



SCUOLA NORMALE SUPERIORE

PH. D. THESIS IN CONDENSED MATTER PHYSICS

OPTIMAL PHASE BIAS IN SUPERCONDUCTING
INTERFEROMETERS

Author

Alberto Ronzani

Advisor

Dott. Francesco Giazotto

ANNO ACCADEMICO 2018/19

Alberto Ronzani: *Optimal phase bias in superconducting interferometers*

This document has been typeset in L^AT_EX with the `classicthesis` template, by André Miede, inspired by Robert Bringhurst's "The Elements of Typographic Style".

CONTENTS

INTRODUCTION	1
LIST OF PUBLICATIONS	5
LIST OF ACRONYMS	7
I METHODS	
1 THEORETIC FUNDAMENTALS	11
1.1 Properties of BCS superconductors	11
1.2 General properties of weak links	15
1.3 Josephson dynamics	17
1.4 Phase bias techniques	21
1.5 Andreev transport	26
1.6 Tunnel junctions	31
1.7 Diffusive weak links	43
2 EXPERIMENTAL PROTOCOLS	65
2.1 Sample fabrication	65
2.2 Low-temperature measurements	71
2.3 Low-frequency characterization	75
II INVESTIGATIONS	
3 VANADIUM/COPPER MICRO-SQUID	81
3.1 Simple model for non-ideal SQUID	83
3.2 Interferometer design and characterization	87
3.3 Magnetometric performance	92
3.4 Discussion	97
4 DOUBLE-LOOP SNS MICRO-SQUID	99
4.1 Two-parameter interferometry	101
4.2 Experimental characterization	104
4.3 Model fitting	106
4.4 Discussion	109

5	ALUMINUM/COPPER SQUIPT	111
5.1	Optimal SQUIPT design	113
5.2	Transport spectroscopy	115
5.3	Magnetometric performance	118
5.4	Discussion	127
6	ALUMINUM-BASED SQUIPTS	129
6.1	Coherent collapse of the order parameter	132
6.2	Transport spectroscopy	134
6.3	Magnetometric performance	141
6.4	Discussion	148
	BIBLIOGRAPHY	149

There's Plenty of Room at the Bottom.

— Richard P. Feynman [10]

INTRODUCTION

A superconducting condensate is characterized by the emergence of macroscopic and collective order, established between its constituent electrons. The degree of correlation at a given spatial position is a complex scalar: it is characterized both by an amplitude (proportional to the minimal energy to generate a fundamental excitation) and a complex phase. Through its gradient, the latter enables the flow of the condensate, demonstrating the quantum fingerprint of superconductivity.

Superconductors exhibit strong coupling to electromagnetic fields, so that phase-dependent dissipationless transport through “weak link” circuitual elements is easily manipulated by applying voltage or magnetic flux bias to superconducting terminals and loops, respectively. For these reasons, superconducting electronics is nowadays a core technology to enable robust access and manipulation of the fundamental degrees of freedom in quantum devices, from ultrasensitive electromagnetic sensors to superconducting qubits.

In this work, we explore different designs of micro-magnetometers based on superconducting interferometers. Differently from conventional designs based on Superconductor, Insulator, Superconductor (SIS) tunnel junctions, here the core elements are nanoscale diffusive metal wires acting as superconducting weak links. These consist in circuitual dishomogeneities that can be fabricated over scales much smaller than typical superconductor coherence lengths, typically yielding unique response properties. On the other hand, their intrinsic transparency is usually associated with strong supercurrent concentration, which can severely limit their practicality due to superconducting depairing and thermal-driven hysteresis upon switching to the dissipative regime.

In this thesis we demonstrate how a judicious use of nanofabricated designs makes it possible to counter these drawbacks and achieve complete phase polarization in interferometers based on diffusive weak links. The resulting micro-magnetometers are characterized by extremely high magnetic responsivity.

STRUCTURE OF THE THESIS

The thesis begins with PART I: METHODS, containing a detailed synopsis of the theoretic and experimental groundwork (chapters 1 and 2, respectively) of the thesis. Of these, chapter 1 is particularly sizeable, and contains my continuing exploration of the foundations of mesoscopic superconductivity, seeded by the guidance of my instructor; interactions with senior scientists and coworkers, my academic track, and the broad amount of literature on this subject, all contributed to its contents.

The main body of the thesis is PART II: INVESTIGATIONS, containing four chapters, each corresponding to a core investigation, whose findings have been published in peer-reviewed journals. Chapter 3 features a study on microscale Superconducting QUantum Interference Devices (SQUIDs) based on V/Cu Superconductor, Normal-metal, Superconductor (SNS) weak links [1]. In chapter 4, the V/Cu SQUID design is extended to include an additional magnetic flux-coupling loop, yielding improved interferometric response [2].

The most favorable magnetic flux sensitivity is achieved with Superconducting QUantum Interference Proximity Transistor (SQUIPT) devices. Chapter 5 presents the design and characterization of the first SQUIPT capable of complete phase modulation of the minigap in a short Al/Cu SNS weak link, leading to excellent performance [3, 5] at 240 mK. The thesis is concluded with chapter 6, where these optimal design principles are applied to the phase-bias of a nanoscale Al Superconductor, Superconductor, Superconductor (SSS) weak link up to the point of complete collapse of the order parameter in its center. As a consequence of the sudden character of this collapse, the resulting device demonstrates record magnetometric figures [4, 6] at 1 K.

ACKNOWLEDGEMENTS

It is often said that a PhD is the crowning demonstration of scientific independence. Looking back at the full extent of the path explored, it is clear to me how much of this independence is really built on the support of peers and mentors alike.

I am deeply grateful to my supervisor, Francesco Giazotto, for his scientific guidance, his unwavering enthusiasm, and most of all for being a source of stability against the hail of little day-to-day failures that pepper the work life of a researcher. On the academic side, I would like to thank my former supervisor, Prof. Fabio Beltram, who taught me never to settle for anything less than excellence, both in form and substance. Furthermore, I would like to acknowledge Prof. Vittorio Giovannetti for kindly accepting the role of internal supervisor.

I feel grateful to Prof. Alessandro Tredicucci for introducing me to the NEST laboratories, leading me in my first steps as a researcher, and being a constant source of support, education and inspiration. Likewise, I thank deeply Miriam Vitiello for (quite literally) holding my hand in my first practical encounters with III-V semiconductor devices. The NEST research environment is amazingly rich with outstanding scientists, that end up influencing by example anyone who works there. In this sense, I feel particularly grateful to Lucia Sorba and Pasqualantonio Pingue for their guidance.

Life in research is not really possible without great co-workers and friends. A special, grateful acknowledgement goes to Carles Altimiras, with whom I shared many important moments, both professionally and personally. Mario Amado Montero and Pepa Martínez Pérez were probably the first who amazed me with their whirlpool of positivity and talent. A fundamental acknowledgement goes to Pauli Virtanen, who went above and beyond to push me through the perilous lands of the theory of mesoscopic superconductivity.

I'll always remember fondly my time with Matthieu Baillergeau, Antonio Fornieri, Jonna Tiira, and Maria Camarasa Gomez. Last but not least Simone Zanotto, good friend and best roommate ever.

FUNDING

My doctoral studies, core [1–4] and supplementary [5–7] publications have been supported by:

- Fondazione Tronchetti Provera,
- Marie Curie Initial Training Action (ITN) Q-NET 264034,
- Italian Ministry of Defense through the PNRM project TERASUPER,
- Italian Ministry of Education, University and Research (MIUR) through the programme FIRB-RBFR1379UX “Coherent Caloritronics (CoCa)”,
- European Research Council under the European Union’s Seventh Framework Programme (FP7/2007-2013)/ERC grant agreement No. 615187-COMANCHE.

The additional works [8, 9], published within the doctoral program in topics not covered in this thesis, have received funding by:

- Italian Ministry of Education, University, and Research (MIUR) through the programme FIRB—RBFR10LULP “Fundamental research on Terahertz photonic devices”,
- European Research Council under the European Union’s Seventh Framework Programme (FP7/2007-2013)/ERC advanced grant agreement No. 321122-SOULMAN.

LIST OF PUBLICATIONS

- [1] A. Ronzani, M. Baillergeau, C. Altimiras, and F. Giazotto. "Micro-superconducting quantum interference devices based on V/Cu/V Josephson nanojunctions." In: *Applied Physics Letters* 103.5 (2013), p. 052603.
- [2] A. Ronzani, C. Altimiras, and F. Giazotto. "Balanced double-loop mesoscopic interferometer based on Josephson proximity nanojunctions." In: *Applied Physics Letters* 104.3 (2014), p. 032601.
- [3] A. Ronzani, C. Altimiras, and F. Giazotto. "Highly sensitive Superconducting Quantum-Interference Proximity Transistor." In: *Physical Review Applied* 2.2 (2014), p. 024005.
- [4] A. Ronzani, S. D'Ambrosio, P. Virtanen, F. Giazotto, and C. Altimiras. "Phase-driven collapse of the Cooper condensate in a nano-sized superconductor." In: *Physical Review B* 96 (2017), p. 214517.
- [5] S. D'Ambrosio, M. Meissner, C. Blanc, A. Ronzani, and F. Giazotto. "Normal metal tunnel junction-based Superconducting Quantum Interference Proximity Transistor." In: *Applied Physics Letters* 107.11 (2015), p. 113110.
- [6] P. Virtanen, A. Ronzani, and F. Giazotto. "Spectral Characteristics of a Fully Superconducting SQUIPT." In: *Physical Review Applied* 6.5 (2016), p. 054002.
- [7] P. Virtanen, A. Ronzani, and F. Giazotto. "Josephson Photodetectors via Temperature-to-Phase Conversion." In: *Physical Review Applied* 9 (2018), p. 054027.
- [8] M. S. Vitiello, M. Nobile, A. Ronzani, A. Tredicucci, F. Castellano, V. Talora, L. Li, E. H. Linfield, and A. G. Davies. "Photonic quasi-crystal terahertz lasers." In: *Nature Communications* 5 (2014), p. 5884.

- [9] R. Degli Innocenti, Y. D. Shah, L. Masini, A. Ronzani, A. Pitanti, Y. Ren, D. S. Jessop, A. Tredicucci, H. E. Beere, and D. A. Ritchie. "Hyperuniform disordered terahertz quantum cascade laser." In: *Scientific Reports* 6 (2016), p. 19325.

LIST OF ACRONYMS

SQUIPT	Superconducting QUantum Interference Proximity Transistor
SQUID	Superconducting QUantum Interference Device
RCSJ	Resistively and Capacitively Shunted Junction
RSJ	Resistively Shunted Junction
SNS	Superconductor, Normal-metal, Superconductor
SSS	Superconductor, Superconductor, Superconductor
SN	Superconductor, Normal-metal
SIS	Superconductor, Insulator, Superconductor
NIS	Normal-metal, Insulator, Superconductor
NIN	Normal-metal, Insulator, Normal-metal
ABS	Andreev Bound State
BCS	Bardeen, Cooper and Schrieffer
LNA	Low-Noise Amplifier
LIA	Lock-In Amplifier
CPR	Current-Phase Relation
DOS	Density Of States
LDOS	Local Density Of States
DC	Direct Current

RF	Radio Frequency
ADC	Analog to Digital Converter
PSD	Power Spectral Density
CSD	Cross-correlated Spectral Density
SNR	Signal to Noise Ratio
EBL	Electron-Beam Lithography
RPM	Revolutions Per Minute
PMMA	Poly-(Methyl MethAcrylate)
MMA	Methyl MethAcrylate
MAA	MethAcrylic Acid
SEM	Scanning Electron Microscope
IPA	IsoPropylic Alcohol
MIBK	Methyl IsoButyl Ketone
BNC	Bayonet Neill–Concelman
DIL	Dual In Line
PID	Proportional, Integral and Derivative
PCB	Printed Circuit Board

Part I

METHODS

THEORETIC FUNDAMENTALS

The goal of this chapter is to present a synopsis on key concepts in the theory of mesoscopic superconductivity. This compendium sets the context for the topics encountered in the following chapters and provides a focused description for the constituent elements of the fabricated devices.

The chapter begins with a brief overview of selected physical properties of a Bardeen, Cooper and Schrieffer (BCS) superconductor. The focus then shifts towards the general definition and dynamics of superconducting weak links. A discussion on phase-bias limitations completes the overview on the general properties of superconducting interferometry. The second part of the chapter is dedicated to a more fine-grained description of individual circuit elements. The Andreev Bound State (ABS), fundamental building block for Cooper-pair transport between coupled superconductors, is introduced and discussed. Then, transport phenomena between metals separated by a thin oxide layer are discussed in terms of both quasiparticle and Cooper-pair transfer. Finally, weak links characterized by transparent interfaces between the superconducting electrodes and a diffusive conduction channel are reviewed. The semiclassical modelization provided by the Usadel framework is illustrated, including physical observables and analytical limits for the long and short junction. The chapter is concluded by the discussion of weak links based on nanostructured diffusive superconducting channels.

1.1 PROPERTIES OF BCS SUPERCONDUCTORS

The advance in cryogenics that allowed the first liquefaction of helium at the beginning of the twentieth century quickly led to the observation

of zero electrical resistance in a mercury sample cooled below 4.2 K [11]. This event marks the discovery of one of the most spectacular manifestations of the quantum nature of matter.

Although a considerable wealth of phenomenological data and theoretical models [12, 13] had been accumulated on the subject since then, a full explanation from first principles of superconductivity was not developed until 1957, with the BCS theory [14]. This theory shows that, in the presence of so much as a non-zero attractive interaction between the electrons¹, the Fermi sphere is expected to be energetically unstable as the temperature is lowered below a material-dependent threshold: the *critical temperature* (T_c). In this condition, pairs of electrons having opposite spin couple to form a bound state of zero spin: the Cooper pair. Due to the bosonic nature of the pairs, they can collectively occupy the ground state of an highly-correlated macroscopic condensate.

The signature of the non-zero binding energy of pairs appears as an energy gap in the Density Of States (DOS) of single-particle excitations (shown in fig. 1.2), amounting to Δ per electron. This quantity vanishes above the critical temperature, and approaches the finite value Δ_0 in the zero-temperature limit. The full BCS $\Delta(T)$ dependence is determined by the characteristics of the phonon-mediated interaction via the self-consistency equation for the gap:

$$\frac{1}{\lambda} = \int_{\Delta(T)}^{\hbar\omega_D} \frac{dE}{\sqrt{E^2 - \Delta(T)^2}} \tanh\left(\frac{E}{2k_B T}\right), \quad (1.1)$$

where \hbar and k_B are respectively the reduced Planck's and Boltzmann's constants. Material-dependent parameters include the high-frequency cutoff for phonon interaction ω_D and the adimensional parameter λ describing the strength of the effective interaction between the paired electrons. In the limit of weak coupling² $\lambda \ll 1$, eq. (1.1) yields $T_c \approx 1.13 \hbar\omega_D/k_B \exp(-1/\lambda)$ as well as $\Delta_0 = \Delta(0) = \hbar\omega_D/\sinh(1/\lambda)$; in

¹ In conventional superconductors this interaction is mediated by phonons, meaning that electrons are reciprocally coupled by the vibrations of the crystalline lattice.

² This can be assumed to be the case for all elemental superconductors.

particular, $\Delta_0 \approx 1.76 k_B T_c$. In the weak coupling limit, the normalized $\Delta(T/T_c)/\Delta_0$ assumes the dependence shown in fig. 1.1.

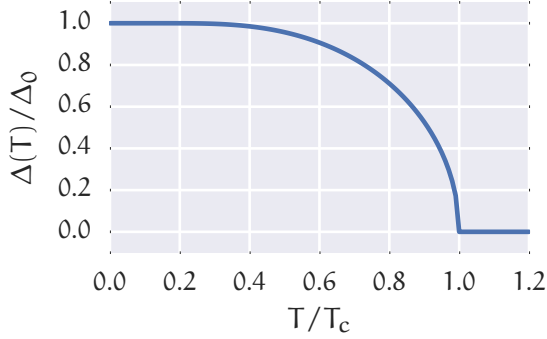


Figure 1.1: Temperature dependence of the gap for a superconductor in the weak coupling limit of BCS.

The BCS theory also provides the functional form of the DOS of the single-particle excitations of the Cooper condensate

$$\rho_S(E) = N_0 \frac{|E|}{\sqrt{E^2 - \Delta^2}} \Theta(|E| - \Delta), \quad (1.2)$$

where the energy variable E is relative to the Fermi energy, Θ is the Heaviside step function and N_0 is the value of the DOS at the Fermi energy for the normal state. From the functional in eq. (1.2) it can be seen that the energy gap developed with the superconducting transition displaces the single-electron states at the Fermi energy from the constant³ normal metal DOS but overall conserving the number of states.

The appearance of a Cooper condensate is a manifestation of a second-order phase transition, in which the order parameter is proportional

³ The DOS in the normal state is *approximately* constant over the energy range relevant to superconducting phenomena, the typical values of Δ being negligible when compared to the Fermi energy.

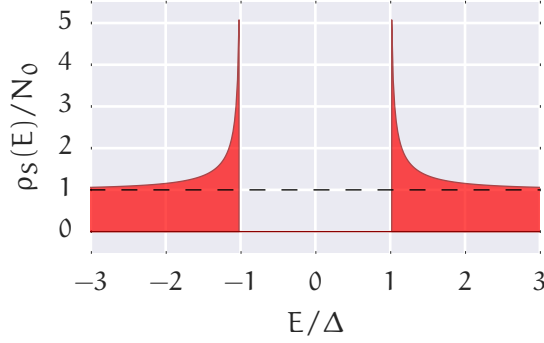


Figure 1.2: Normalized quasiparticle DOS in the BCS theory (red). The normal-state DOS is superimposed as a dashed black line. The energy scale is relative to the Fermi energy and normalized to Δ .

to electronic correlation. To describe the latter, a position-dependent complex pair amplitude is generally adopted. Its magnitude is set to $\Delta(\mathbf{r})$; the phase degree of freedom $\phi(\mathbf{r})$ is introduced to account for supercurrent-carrying states of the condensate⁴. In fact, this picture corresponds to a Schrödinger-like description of the Cooper condensate in terms of the wavefunction

$$\psi(\mathbf{r}) \propto \Delta(\mathbf{r}) \exp(i\phi(\mathbf{r})). \quad (1.3)$$

With an opportune normalization of the wavefunction, $|\psi|^2 = n_S$, the spatial density of Cooper pairs. Then, the current density can be derived as

$$\mathbf{j}_S = \frac{q_p}{2m_p} \left[(\psi^* \hat{\mathbf{p}} \psi - \psi \hat{\mathbf{p}} \psi^*) - 2q_p \mathbf{A}(\mathbf{r}) |\psi|^2 \right], \quad (1.4)$$

where $q_p = 2e$ and m_p are respectively the charge and mass of a Cooper pair; the term containing the vector potential $\mathbf{A}(\mathbf{r})$ accounts

⁴ I. e., when the net collective momentum of the ground state of the condensate is different from zero.

for the magnetic interaction under minimal coupling. Substituting the functional form of eq. (1.3) in eq. (1.4) yields

$$\mathbf{j}_S = n_S \frac{q_p}{m_p} \left[\hbar \vec{\nabla} \phi - q_p \mathbf{A} \right], \quad (1.5)$$

where the term in square parentheses is the kinetic momentum.

1.2 GENERAL PROPERTIES OF WEAK LINKS

In the broadest sense, a weak link is a portion of a superconducting path featuring a spatially localized suppression of the critical current value⁵ with respect to its neighboring parts. Actual implementations are numerous [15]: they include thin insulating barriers, geometric constrictions and point contacts, as well as hybrid structures based on normal metals, ferromagnets, topological insulators, graphene, high-mobility semiconducting elements, carbon nanotubes, semiconducting nanowires and quantum dots.

Regardless of their specific nature, weak links are important in superconducting circuits, where they provide preferential pinning points for the establishment of phase gradients. As a result, the supercurrent flowing across a weak link is a function of the well-defined phase difference across its boundaries [16]. This functional dependence is called Current-Phase Relation (CPR); in symbols $I_S(\theta)$, where θ is the gauge-invariant phase difference across the weak link. The latter is derived from the kinetic momentum in eq. (1.5) so that the value of the integral

$$\theta \equiv \int_{e_1}^{e_2} \frac{m_p \mathbf{v} \cdot d\mathbf{r}}{\hbar} = \Delta\phi - \frac{q_p}{\hbar} \int_{e_1}^{e_2} \mathbf{A} \cdot d\mathbf{r} \quad (1.6)$$

is independent from the particular choice for the electromagnetic gauge; in eq. (1.6) e_1, e_2 label the electrodes and $\Delta\phi$ is the difference in phase of the order parameter between the electrodes. In absence of magnetic

⁵ I.e., the maximal current that can be supported without collapsing the superconducting phase.

field $\theta \equiv \Delta\phi$. To complement the general definition of a weak link, eq. (1.6) can be reworked as

$$\vec{\nabla}\theta = \frac{m_p \mathbf{v}}{\hbar} = \frac{m_p}{\hbar q_p} \frac{\mathbf{j}_S}{n_S}, \quad (1.7)$$

to show that considerable phase gradients are expected either with the suppression of the spatial density of the Cooper pair condensate (this is the case in tunnel junctions) or whenever a geometric constriction increases the current density. Both effects are typically present in most weak link implementations.

Independently from the specific composition of a weak link, the following fundamental properties apply to its CPR.

PERIODICITY: The physical state of a Cooper condensate is the same when the phase is rotated by 2π ; hence the CPR is a 2π -periodic function of its argument.

$$I_S(\theta) = I_S(\theta + 2\pi)$$

PARITY: Due to time-reversal symmetry, a change in the direction of the supercurrent has to be matched by a change in the sign of the phase gradient; hence the CPR is an *odd* function of its argument.

$$I_S(-\theta) = -I_S(\theta)$$

NODES: Zero current is expected when θ equals to zero, due to the odd parity. Additionally, the combination of parity and periodicity also requires the current to be zero when θ equals to π or its integer multiples.

$$I_S(\pi n) = 0 \quad \forall n \in \mathbb{Z}$$

The properties listed above can be embodied in the following Fourier series expansion:

$$I_S(\theta) = \sum_{k=1}^{\infty} I_k \sin(k\theta). \quad (1.8)$$

The free energy of a weak link can be obtained by integration of the CPR, in analogy with the energy stored in an inductor:

$$E_{\text{wl}}(\theta) = \int_0^\theta \mathcal{L}_{\text{wl}}(\vartheta) I_S(\vartheta) dI_S = \frac{\hbar}{2e} \int_0^\theta I_S(\vartheta) d\vartheta. \quad (1.9)$$

Here, the non-linear inductance of the weak link is defined as

$$\mathcal{L}_{\text{wl}}(\theta) = \frac{\hbar}{2e} \left(\frac{dI_S}{d\theta} \right)^{-1}. \quad (1.10)$$

1.3 JOSEPHSON DYNAMICS

In 1962 Josephson published the key prediction that two superconductors separated by a tunnel junction could support a dissipationless current due to the coherent tunneling of Cooper pairs [17]. The equations describing this phenomenon (called Josephson effect) are remarkably simple.

$$I_S(\theta) = I_c \sin \theta \quad (1.11)$$

$$\frac{d\theta}{dt} = \frac{2eV_j}{\hbar} \quad (1.12)$$

Here θ is the gauge-invariant phase difference, I_S and V_j are respectively the supercurrent and the voltage at the junction, and I_c is the maximal supercurrent that can be sustained by the weak link in the non-dissipative state.

Although the derivation of eqs. (1.11) and (1.12) was targeted to quantum tunneling in SIS junctions, it has since been recognized that its range of applicability extends to most superconducting weak links. In particular, the harmonic CPR in eq. (1.11) has been found to be the limiting form of the more general eq. (1.8) when the superconducting electrodes are suitably weakly-coupled⁶. Equation (1.12) is even more

⁶ Exceptions to this case include high-transparency tunnel barriers, short diffusive contacts at low temperature and systems characterized by depairing induced by strong supercurrent concentration, as well as superconducting atomic contacts.

general, being derivable from the unitarity of the temporal evolution of the phase difference between two Cooper condensates having different values of the chemical potential.

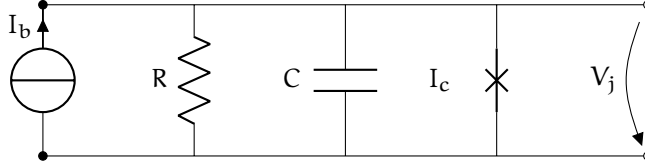


Figure 1.3: Equivalent circuit for the **RCSJ** model.

Equations (1.11) and (1.12) provide the foundation to model the dissipative state of a current-biased Josephson junction in actual superconducting devices. In the Resistively and Capacitively Shunted Junction (**RCSJ**) model, the physical junction is schematized as the parallel of an ideal Josephson weak link, a resistor and a capacitor. This arrangement, shown in fig. 1.3, is described by the following equation:

$$I_b = I_c \sin \theta + \frac{V_j}{R} + C \frac{dV_j}{dt}, \quad (1.13)$$

where I_b is the bias current and C , R are respectively the interelectrode capacitance and the effective resistance⁷ of the physical junction.

Substitution of eqs. (1.11) and (1.12) in eq. (1.13) yields the second order nonlinear differential equation:

$$\frac{\hbar C}{2e} \ddot{\theta} + \frac{\hbar}{2eR} \dot{\theta} = I_b - I_c \sin \theta, \quad (1.14)$$

⁷ Here the approximation corresponds to a linearized current-voltage response, wherein the linear coefficient depends on the characteristic of the junction. In **SIS** junctions the relevant figure is the subgap resistance, which can be significantly larger than the tunnel resistance at low temperature.

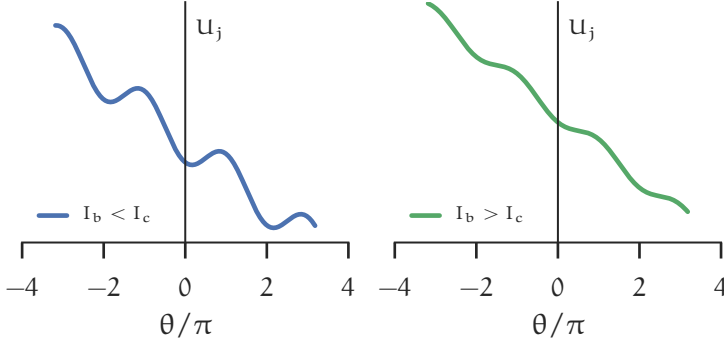


Figure 1.4: Washboard potential in the [RCSJ](#) model.

where the dots indicate the time derivatives. The latter equation describes a dynamic analogous to a massive particle subjected to drag moving in the potential

$$U_j(\theta) = -\frac{\hbar}{2e} \int [I_b - I_c \sin \vartheta] d\vartheta = -E_j (\cos \theta + i_b \theta), \quad (1.15)$$

where $i_b = I_b/I_c$ is the normalized bias current and $E_j = \hbar I_c/2e$ is the Josephson energy. The cosine term in eq. (1.15) is actually the free energy of the junction, obtained by integration of the sinusoidal [CPR](#) of eq. (1.11).

Figure 1.4 shows $U_j(\theta)$ in two limiting cases. When the external bias current is less than the critical current of the junction (leftmost plot) the potential landscape admits several equivalent local minima, located at $\theta^* = \arcsin(i_b)$ in the steady state. The voltage developed by the junction is null. Conversely, when the external bias current is larger than the critical current (rightmost plot) no equilibrium points are present, and the θ variable is forced to evolve with a non-zero time-averaged $\dot{\theta}$, corresponding to a finite V_j by virtue of eq. (1.12).

To explicitate the role of junction capacitance (i. e., the mass parameter), eq. (1.14) is reworked in a more compact form:

$$\beta_c \theta'' + \theta' + \sin \theta = i_b, \quad (1.16)$$

where $\beta_c = 2eCR^2I_c/\hbar$ is the *Stewart-McCumber* parameter and the prime (') symbols denote differentiation with respect to the normalized time $\tau = t/\tau_{RL} = 2etRI_c/\hbar$. In the low-capacitance regime (or overdamped limit, corresponding to $\beta_c \ll 1$), the dynamics reduce to the so-called Resistively Shunted Junction (*RSJ*) model. There is no kinetic energy associated to the evolution of θ , so that the “particle” is immediately released from or trapped to a local minimum of U_j when the bias current crosses the critical current. In the opposite high-capacitance case (underdamped limit, $\beta_c \gg 1$), the kinetic term is sizeable and a retrapping event⁸ may only be possible with the voltage (proportional to the velocity in the moving particle picture) falling under a certain threshold.

Physical *SIS* junctions often natively belong to the underdamped regime; their current-voltage characteristics show significant amount of switching-retrapping hysteresis⁹. On the contrary, low-impedance Josephson weak links such as *SNS* junctions are intrinsically overdamped, being characterized by both negligible normal-state resistance and interelectrode capacitance.

Although rather idealized, the *RCSJ* model captures the essence of the time-dependent processes occurring in several physical implementations of superconducting circuits. It has been extended to include fluctuation effects to accurately design devices of great practical importance such as *SQUIDS* and junction arrays in use as metrological standards. Last but not least, the quantum mechanical treatment of the tilted-washboard potential is a fundamental building block for the design of frontier technology such as quantum computation in circuit QED.

⁸ I. e., the return to the zero-voltage state.

⁹ A practical solution to suppress this type of hysteresis is to add an external shunting resistor to the junction. Its purpose is to enhance the relative effect of the “drag” term in eq. (1.14), bringing β_c to the overdamped limit.

1.4 PHASE BIAS TECHNIQUES

External control of the phase difference of individual Josephson junctions arranged in a non simply-connected topology enables supercurrent interferometry. In the previous section it has been implied that a partial degree of phase control can be achieved by imposing a fixed current bias to a weak link in the zero-voltage state. With this technique, the junction can only be phase-biased in a subset of the full $0-2\pi$ range; for example, in the common case of a sinusoidal CPR, $\theta^* = \arcsin(I_b/I_c)$, with $\theta^* \in (-\pi/2, \pi/2)$.

Access to the full $0-2\pi$ range is feasible by exploiting a fundamental property of the superconducting condensate, namely the fact that its order parameter is a single-valued scalar function of the spatial coordinate. The single-valuedness requirement constrains the value of any closed-loop line integral of the gradient of the phase to multiples of 2π :

$$\oint \vec{\nabla} \phi \cdot d\mathbf{r} = 2\pi n, \quad \text{with } n \in \mathbb{Z}. \quad (1.17)$$

Recalling that the canonical momentum of the condensate is $\mathbf{p} = m_p \mathbf{v} + q_p \mathbf{A} = \hbar \vec{\nabla} \phi$, eq. (1.17) yields the quantization [18, 19] of the *fluxoid* \mathcal{F} in terms of the flux quantum $\Phi_0 = h/2e$:

$$\mathcal{F} = \frac{1}{q_p} \oint (m_p \mathbf{v} + q_p \mathbf{A}) \cdot d\mathbf{r} = \frac{\hbar}{q_p} \oint \vec{\nabla} \phi \cdot d\mathbf{r} = n \Phi_0. \quad (1.18)$$

For a Cooper condensate spanning a simply-connected domain $\mathcal{F} = 0$. In particular, in the limit of a vanishing path this constraint reduces eq. (1.18) to:

$$\vec{\nabla} \times \mathbf{j} = q_p n_s \vec{\nabla} \times \mathbf{v} = -\frac{n_s q_p^2}{m_p} \mathbf{B}, \quad (1.19)$$

which corresponds to the second London equation. Conversely, in a non simply-connected topology, such as a superconducting ring, the fluxoid can assume non-zero (integer) values, leading to the well-known

quantization of the magnetic flux for rings which are thick compared to the magnetic penetration length.

Interrupting a superconducting ring with a weak link, as shown in fig. 1.5, allows the latter to be phase-biased by the application of a magnetic field threading the ring. In fact, the gauge-invariant phase dif-

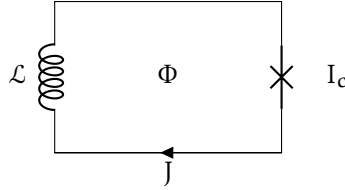


Figure 1.5: Equivalent circuit for magnetic flux biasing.

ference across the weak link can be derived by performing the following integration over the loop:

$$\begin{aligned} \theta &= \oint \vec{\nabla} \phi \cdot d\mathbf{r} = \frac{2\pi}{\Phi_0} \left[\Phi + \frac{m_p}{q_p} \oint \frac{\mathbf{j}\mathbf{s}}{q_p m_p} \cdot d\mathbf{r} \right] \\ &= \frac{2\pi}{\Phi_0} \left[\Phi + \mu_0 \lambda_L^2 \oint \mathbf{j}\mathbf{s} \cdot d\mathbf{r} \right], \end{aligned} \quad (1.20)$$

where Φ is the applied magnetic flux, μ_0 is the magnetic permeability of free space and $\lambda_L = \sqrt{m_p / \mu_0 n_p q_p^2}$ is the London magnetic penetration depth.

The path integral term in eq. (1.20) originates from the kinetic momentum, scales as the normal state resistance of the superconducting ring and it is proportional to the circulating supercurrent. For these reasons, it is considered equivalent to an inductive screening to the externally applied magnetic flux, to be added to the geometric self-inductance term. The kinetic inductance term can become sizeable especially in the case of nanostructured superconducting loops, where the cross-section of

the constituents is often comparable to the scale of London penetration depth. In this formalism, eq. (1.20) is equivalent to

$$\theta = \frac{2\pi}{\Phi_0} [\Phi - \mathcal{L}J(\theta)] , \quad (1.21)$$

where \mathcal{L} is an effective inductance whose value is the sum of both kinetic and geometric components. The circulating current J is a function of θ via the CPR of the weak link; its sign is negative due to the fact that the current density in eq. (1.20) opposes the applied magnetic field consistently with eq. (1.19).

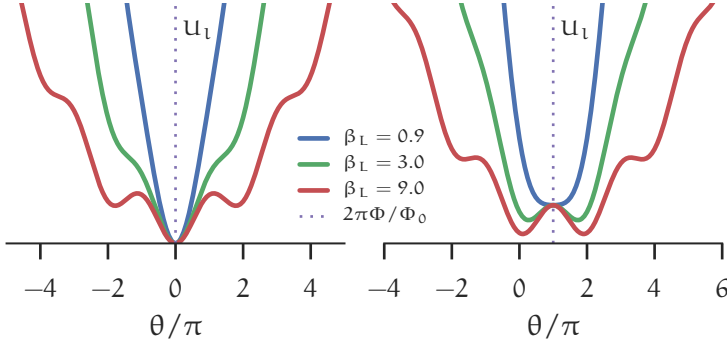


Figure 1.6: Effective potential of a Josephson weak link embedded in a superconducting loop.

In the case of a sinusoidal Josephson relation, eq. (1.21) can be reworked in:

$$2\pi \frac{\Phi}{\Phi_0} = \theta + \beta_L \sin \theta , \quad (1.22)$$

where $\beta_L = 2\pi\mathcal{L}I_c/\Phi_0$ is the adimensional inductive screening parameter. Equation (1.22) describes the position of the local maxima and minima of an effective potential U_l , in analogy with eq. (1.15):

$$U_l(\theta) = E_j \left[\frac{\left(\theta - 2\pi\frac{\Phi}{\Phi_0}\right)^2}{2\beta_L} + (1 - \cos\theta) \right], \quad (1.23)$$

where the parabolic term is the free energy of the inductor, whose CPR is linear. In the limit of vanishing β_L this term constrains the value of θ to be identically equal to $2\pi\Phi/\Phi_0$. Figure 1.6 shows the effect of an increasing β_L parameter. With no external magnetic flux (left panel), the global minimum of U_l is located at $\theta = 0$ independently of the value of β_L . On the other hand, for $\Phi = \Phi_0/2$ (right panel) potential curves having $\beta_L > 1$ show multiple local minima.

Graphical representations of eq. (1.22) for different β_L values are presented in fig. 1.7. Coherently with the previous discussion, it can be noted that a bijective θ - Φ relation is only possible when $\beta_L < 1$, where $\theta = \pi$ is still a local minimum for U_l with $\Phi = \Phi_0/2$. Hysteretic phenomena and phase-tunneling between different local minima are expected with $\beta_L > 1$. The critical value $\beta_L = 1$ corresponds to a divergent $d\theta/d\Phi$ value at $\Phi = \Phi_0/2$.

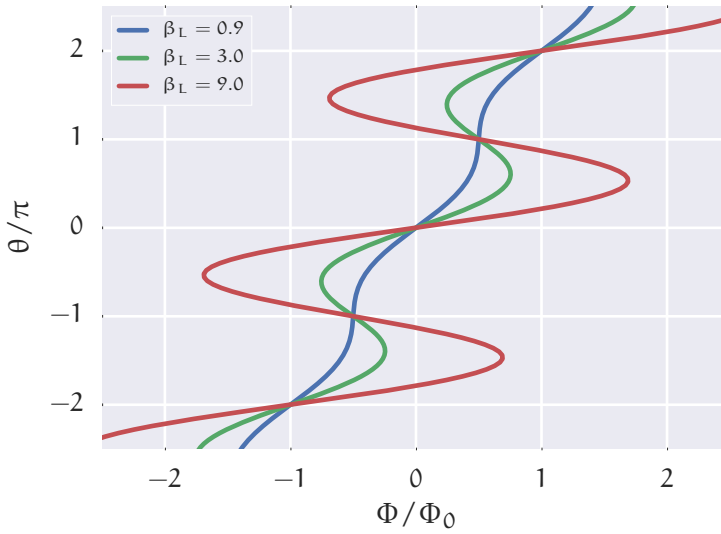


Figure 1.7: Inductance-based hysteresis in magnetic phase bias. Solutions to eq. (1.22) for different values of the inductive screening parameter β_L are plotted in the θ, Φ space. Non-hysteretic $\theta(\Phi)$ is only possible with $\beta_L < 1$.

1.5 ANDREEV TRANSPORT

Although the functional description of superconducting weak links in sections 1.2 to 1.4 provides a vast amount of predictions regarding their transport dynamics, a more insightful picture can be obtained by considering the microscopic foundation of interface-bound supercurrent transport. In particular, the latter can be understood in terms of a peculiar charge transport mechanism occurring at a transparent Superconductor, Normal-metal (SN) interface: the *Andreev reflection* [12, 13, 20].

An electron having energy close to the chemical potential of the normal domain of an unbiased clean SN interface is not expected to propagate as a quasiparticle in the superconductor due to the presence of the energy gap in the excitation spectrum of the latter. On the other hand, an elastic reflection would require a momentum change of the order of twice the Fermi momentum in order to reverse the motion of the electron. However, the relative change in momentum that may be provided by the “barrier” represented by the gap is proportional to the ratio $\Delta/E_F \ll 1$, where E_F is the Fermi energy. As such, momentum conservation prevents the electron from being elastically back-reflected into the normal metal.

In an Andreev reflection the electron can instead be back-reflected as a hole. This event is accompanied by the generation of a Cooper pair in the superconducting electrode. The whole process satisfies energy and momentum conservation and results in a net transfer of twice the elementary charge, leading to a significant enhancement of the subgap conductance¹⁰. As a result of the interaction with the Cooper condensate, the relative phases of the impinging electron and the back-reflected hole are correlated. In a SNS structure in which the effective electron path length is less than the coherence length, the Andreev

¹⁰ The subgap conductance of an ideally transparent SN junction is twice the conductance of the corresponding NN system obtained, e. g., by quenching the superconductivity with the application of a strong magnetic field.

reflection events at the two SN interfaces interfere constructively leading to the appearance of Andreev Bound States (ABSs) [21].

ABSs are supercurrent-carrying electronic quantum states localized at the weak link; their energy is a function of the phase difference across the superconducting electrodes. The total supercurrent in a generic weak link can be thought of as resulting from the integration of a phase-dependent energy distribution of supercurrent called *spectral current*. The total supercurrent carried by ABSs in stationary conditions can be expressed in the general form:

$$I_S(\theta) = \int_{-\infty}^{+\infty} \mathcal{J}_{sp}(\varepsilon, \theta) \tan\left(\frac{\varepsilon}{2k_B T}\right) d\varepsilon, \quad (1.24)$$

where \mathcal{J}_{sp} is an appropriate spectral current, incorporating the CPR dependence of each ABS as well as their distribution in energy. Depending on the nature of the weak link, the spectral current may assume a structure peaked at specific energy values corresponding to well-defined electron trajectories; this is typical for ballistic conduction channels. On the other hand, the presence of disorder such as the grain-to-grain scattering in diffusive weak links causes an effective wash-out of the spectral current peak structure as a result of the statistical averaging over a continuous distribution of path lengths.

The elementary form of an individual ABS can be appreciated considering a weak link constituted by a single short and semi-transparent conduction channel¹¹. Here, the excitation spectrum obtained by the solution of the Bogoliubov-de Gennes equation in a scattering-matrix formalism shows the functional form:

$$E_\tau(\theta) = \pm\Delta\sqrt{1 - \tau\sin^2(\theta/2)}, \quad (1.25)$$

where Δ , θ are respectively the BCS superconducting gap and the gauge-invariant phase difference at the electrodes and $0 < \tau \leq 1$ models

¹¹ I. e., where the longitudinal and transverse dimensions are small with respect to both the electron mean free path and the superconducting coherence length and the traversal time is negligible with respect to \hbar/Δ .

the transmissivity of the channel. Since the CPR is proportional to the derivative of the free energy F of the weak link with respect to the phase difference, the supercurrent is

$$\begin{aligned} I_S(\theta) &= \frac{2\pi}{\Phi_0} \frac{dF}{d\theta} \quad (1.26) \\ &= \frac{\pi \tau \Delta}{2 \Phi_0} \frac{\sin \theta}{\sqrt{1 - \tau \sin^2(\theta/2)}} \tanh \left(\frac{\Delta \sqrt{1 - \tau \sin^2(\theta/2)}}{2k_B T} \right). \quad (1.27) \end{aligned}$$

Figure 1.8 shows the energy dispersion (top panel) and corresponding zero-temperature CPRs (bottom left panel) for ABSs characterized by selected values of the transparency parameter τ . The magnitude scale of the supercurrent at zero temperature is $I_0 \equiv \pi\tau\Delta_0/2\Phi_0$. The extremal values of the transparency range demonstrate two opposite paradigms at low temperature. In the low-transparency limit ($\tau \ll 1$, typical of tunnel junctions) the energy dispersion of the ABS is basically flat; the critical current amplitude is correspondingly suppressed with I_0 . The CPR reduces to $I_S(\theta) = I_0 \sin(\theta)$, consistently with the behaviour expected for weakly-coupled superconducting electrodes.

A gradual increase in transparency corresponds to wider amplitude in the phase-dependent energy modulation as well as to the progressive development of non-harmonicity in the CPR. Ultimately, in a perfectly transparent conduction channel ($\tau = 1$) the ground and excited ABS branches become degenerate for $\theta = \pi$, where the corresponding CPR is discontinuous¹² in the zero-temperature limit:

$$I_S(\theta) = \begin{cases} +2I_0 \sin(\theta/2) & 0 \leq \theta < \pi \\ 0 & \theta = \pi \\ -2I_0 \sin(\theta/2) & \pi < \theta \leq 2\pi \end{cases}. \quad (1.28)$$

¹² This singular behaviour, shown as a dashed line in the bottom left panel of fig. 1.8, is resolved with either non-zero temperature or $\tau < 1$, so it is never truly observed in practical devices.

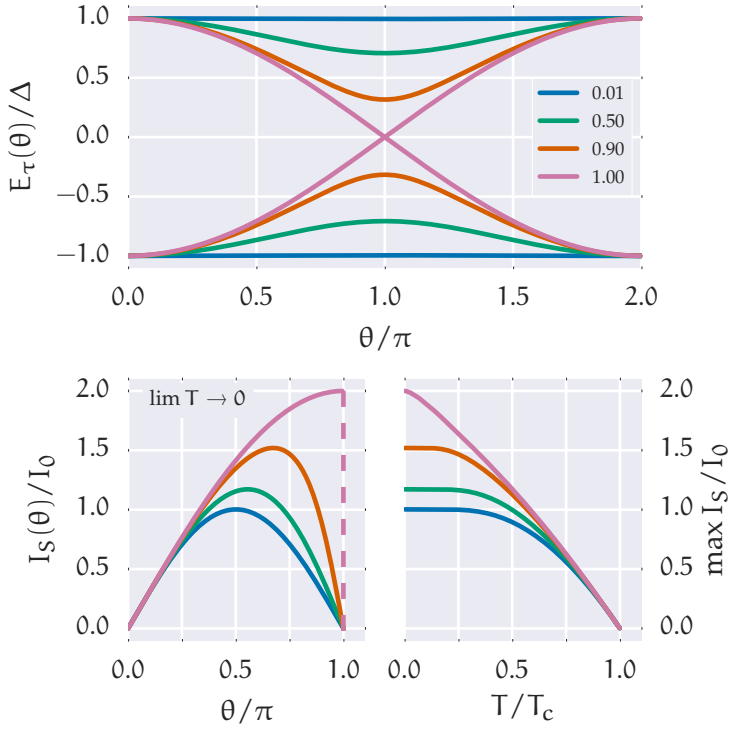


Figure 1.8: Phase response of a single-channel ABS. The top panel shows the phase-dependent energy spectrum; different traces are color-coded to different values of channel transparency τ . The bottom left panel shows the corresponding CPRs in the low-temperature limit. The bottom right panel shows the thermal dependence of the critical current values.

The bottom right panel in fig. 1.8 shows the temperature dependence of the critical current of the weak link, normalized with respect to I_0 . Finite temperature affects both the value of the superconducting gap at the electrodes and the relative population of the ground and excited ABS branches. From the graphs it can be seen that, for sufficiently transparent channels, the latter mechanism affects appreciably the critical current even at low temperature values ($T < T_c/3$), where the $\Delta(T)$ dependence is basically flat. On the other hand, independently of transparency, the normalized CPRs tend to the harmonic Aslamazov-Larkin model [16, 22] in the vicinity of the critical temperature:

$$\frac{I_S(\theta)}{I_0} = \frac{\Delta^2(T)}{2\Delta_0 k_B T} \sin \theta \approx 2.66 \left(1 - \frac{T}{T_c}\right) \sin \theta, \quad T \rightarrow T_c. \quad (1.29)$$

The single channel picture can be readily generalized for weak links composed of several conduction channels, each characterized by a specific transparency value τ_k . Equation (1.26) becomes:

$$I_S(\theta) = \frac{2\pi}{\Phi_0} \sum_k \frac{dE_k(\theta)}{d\theta} \tanh\left(\frac{E_k(\theta)}{2k_B T}\right), \quad (1.30)$$

where $E_k(\theta)$ is the energy dispersion of the k -th ABS. Equation (1.30) is the limiting form of eq. (1.24) for a spectral current derived from a discrete set of ABSs.

The last sections concluding this chapter focus on two types of weak link, oxide-barrier junctions and hybrid SN structures characterized by clean intermetallic contacts. The theoretical results listed therein set a specific reference for the understanding of individual circuit elements employed in the devices presented in the following chapters.

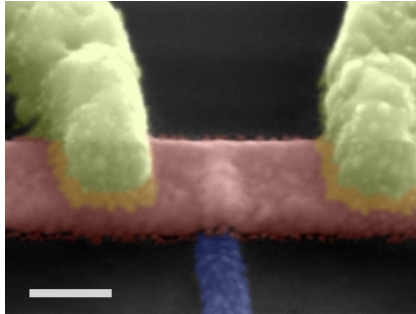


Figure 1.9: Tilted (60 deg.) pseudocolor scanning electron micrograph of a detail in a fabricated device. A 25 nm-thick Cu wire (red) is contacted to a buried superconducting tunnel probe (blue) realized by a 15 nm-thick oxidized Al film. The normal metal wire is proximized by the clean contact with 150 nm-thick Al electrodes (yellow) forming a SNS junction. The scale bar at the bottom left represents a horizontal distance of 100 nm.

1.6 TUNNEL JUNCTIONS

In circuit elements based on tunnel junctions charge transport is due to quantum tunneling of carriers through a suitably thin insulating barrier. The latter separates two metallic domains that can be either in the superconducting or in the normal state, resulting in SIS, Normal-metal, Insulator, Superconductor (NIS) and Normal-metal, Insulator, Normal-metal (NIN) junction types. For applications in superconducting electronics a typical choice is to realize overlap junctions where the insulating barrier is provided by the controlled oxidation of an aluminum layer. The latter may either coincide with a superconducting electrode or, as it is common for devices designed to work at liquid helium temperature, deposited as a nm-thick wetting layer over niobium-based electrodes. The resulting weak links are stable against aging and repeated cooldowns, and their reliability makes them widely used as

Josephson junctions in commercial low-temperature superconducting electronic devices and sensors.

Supercurrent transport in SIS junction can be understood as the direct tunneling of Cooper pairs across the thin insulating barrier. The temperature-dependent CPR for this process has been derived analytically by Ambegaokar and Baratoff [23]:

$$I_S(\theta) = \frac{\pi \Delta G_T}{2e} \tanh\left(\frac{\Delta}{2k_B T}\right) \sin \theta, \quad (1.31)$$

where G_T is the tunnel conductance. The Ambegaokar-Baratoff CPR is evidently equivalent to the limit $\tau \ll 1$ in eq. (1.27). In this analogy, the tunnel junction is composed of \mathcal{N} channels of low average transparency. The tunnel conductance $G_T = \mathcal{N}\tau e/\Phi_0 = \mathcal{N}\tau G_0$, where $G_0 = 2e^2/h \approx 77.5 \mu\text{S}$ is the quantum of conductance. It follows that the critical current is suppressed with increasing temperature in accordance with the $\tau \ll 1$ case in the bottom right panel of fig. 1.8 (blue trace), where its value is approximately constant up to $T \simeq T_c/3$. Close to T_c the suppression of the critical current is linear with temperature in accordance with the Aslamazov-Larkin model¹³.

It is worth mentioning that the Ambegaokar-Baratoff model can be generalized to include the case of a SIS junction composed of superconductors having different critical temperature values [16]. In this case, adopting the Matsubara formalism,

$$I_S(\theta) = \frac{2\pi G_T k_B T}{e} \sum_{\omega_n > 0} \frac{\Delta_1 \Delta_2}{\sqrt{(\omega_n^2 + \Delta_1^2)(\omega_n^2 + \Delta_2^2)}} \sin \theta, \quad (1.32)$$

where Δ_1, Δ_2 are the superconducting gap values for each electrode and $\omega_n = \pi k_B T(2n + 1)$ represents the discrete set of Matsubara energies. In general, the sum in eq. (1.32) has to be carried out numerically. However, close to the lower critical temperature, the CPR converges to the asymmetric Aslamazov-Larkin model:

$$I_S(\theta) = \frac{\pi \Delta_1 \Delta_2 G_T}{4ek_B T} \sin \theta, \quad T \rightarrow \min [T_{c1}, T_{c2}]. \quad (1.33)$$

¹³ See eq. (1.29).

Another important charge transport mechanism is given by the tunneling of quasiparticles at finite voltage bias. Under thermal equilibrium, the quasiparticle current can be expressed by the transport integral

$$I_{\text{qp}}(V) = \frac{G_T}{e} \int_{-\infty}^{+\infty} \rho_1(E) \rho_2(E + eV) [g(E) - g(E + eV)] dE, \quad (1.34)$$

where $\rho_{1,2}(E)$ are the normalized quasiparticle DOSs in the left and right electrodes and $g(E) = 1/[1 + \exp(E/k_B T)]$ is the Fermi-Dirac distribution function [24]. The left panel of fig. 1.10 shows an example of the current-voltage characteristics resulting from eq. (1.34) in the case of a NIS junction at zero and finite temperature. For the DOS of the superconducting electrode a modified form of eq. (1.2) is often assumed:

$$\rho_S(E) = \left| \Re \left[\frac{E/\Delta + i\gamma}{\sqrt{(E/\Delta + i\gamma)^2 - 1}} \right] \right|, \quad (1.35)$$

where the parameter $\gamma \ll 1$ semiempirically models a finite quasiparticle lifetime introducing a small imaginary part in their energy [25]. As a result, the singularities at $E = \pm\Delta$ are lifted and a small subgap DOS appears, in consistence with the experimental observation of non-zero subgap conductance in SIS and NIS junctions [26]. The right panel of fig. 1.10 shows the energy alignment diagram of the DOSs in the NIS junction where the chemical potentials are offset by an applied voltage $V = \Delta/e$, corresponding to the onset of conduction at zero temperature. Finite temperature values influence the population of electron-like and hole-like quasiparticles, represented as blue and white areas in the diagram, respectively.

Tunnel junctions provide a useful tool to directly sample the Local Density Of States (LDOS) of a target metallic domain, provided the DOS of the probing electrode is known. In particular, for a normal-metal

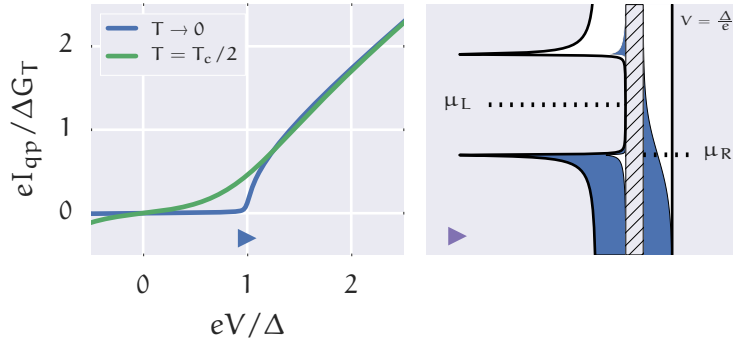


Figure 1.10: Quasiparticle tunnel transport in a NIS junction. The left panel shows the normalized current-voltage characteristic curves calculated from eq. (1.34) for temperature values $T = 0$, $T_c/2$ (blue and green traces, respectively). The bias condition corresponding to the onset of quasiparticle conduction at zero temperature ($V = \Delta/e$) is marked with a rightward facing triangle. The corresponding energy alignment diagram is shown in the right panel, where electron-like and hole-like quasiparticle populations are shown in the DOSs as blue and white areas, respectively. Here the magnitude of thermal excitations has been exaggerated for illustrative purposes.

probe in the zero temperature limit, the conductance is found to be proportional to the [LDOS](#) of the target electrode:

$$G_N(V) = -\frac{G_T}{e} \int_{-\infty}^{+\infty} \rho(E) \left[\frac{\partial g(E + eV)}{\partial V} \right] dE \quad (1.36)$$

$$\approx G_T \rho(eV), \quad T \rightarrow 0. \quad (1.37)$$

With increasing temperature the convolution kernel originating from the electron distribution function¹⁴ broadens, progressively washing out the fine details of $\rho(E)$ from the measurable $G_N(V)$, as shown in the green trace in the left panel of [fig. 1.10](#).

Quasiparticle tunneling is the main conduction pathway for [SIS](#) junctions biased so that the difference in chemical potentials of the electrodes is greater than the sum of the superconducting gaps. The bottom left panel in [fig. 1.11](#) shows the calculated quasiparticle current for an asymmetric [SIS](#) junction both at zero and non-zero temperature. The surrounding panels show the aligned [DOS](#) diagrams at selected voltage bias values. The top left panel corresponds to zero applied voltage, leading to zero net tunneling current regardless of temperature. Moving clockwise, the top right panel shows a condition in which the chemical potential difference is equal to the difference in the superconducting gaps of the electrodes. This regime, where the voltage bias is still in the subgap range, results in a pronounced quasiparticle current peak at finite temperature. This peak originates from a density imbalance between the thermally-excited quasiparticle states in the left and right electrodes, which is maximally evident when the singular features of the [BCS DOSs](#) are aligned. This *singularity-matching peak* is associated with a negative differential resistance region, and disappears at zero temperature. Finally, the onset of the out-of-gap conduction regime is shown in the bottom right panel of [fig. 1.11](#) and corresponds to the alignment of the electron-like states of the left electrode to the hole-like states of the right electrode. The resulting conductance peak is sharper than the corresponding feature found in the [NIS](#) case.

¹⁴ I. e., the term between square parentheses in [eq. \(1.36\)](#).

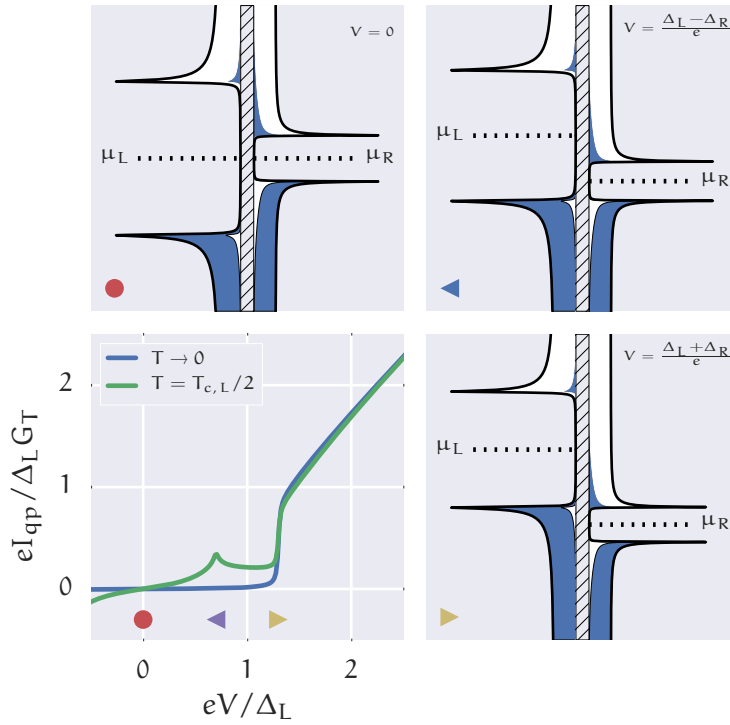


Figure 1.11: Quasiparticle tunnel transport in an asymmetric SIS junction. The bottom left panel shows the normalized current-voltage characteristic curves calculated from eq. (1.34) for temperature values $T = 0$, $T_{c,L}/2$ (blue and green traces, respectively). The surrounding panels show energy alignment diagrams corresponding to relevant biasing conditions marked by matching symbols in the horizontal axis of the bottom left panel. In particular, a non-zero difference in the values of the superconducting gap values between the electrodes results in the appearance of a non-trivial conduction feature (leftward-facing triangle) at finite temperature for $eV = |\Delta_L - \Delta_R|$.

In summary, both superconducting and normal-metal tunnel probes can be exploited to infer the LDOS of a mesoscopic conductor from their quasiparticle current-voltage characteristic curves. Both in normal-metal and superconducting probes, limiting the power dissipation induced by quasiparticle tunneling¹⁵ can be enforced by choosing an optimal barrier opacity during fabrication, hence moderating the magnitude of the current in typical biasing conditions.

Normal-metal probes offer the convenience of direct proportionality between the conductance and the target LDOS, but suffer from a gradual loss of energy selectivity with increasing temperature, due to the broadening of the electron energy distribution in the normal domain. Conversely, the full reconstruction of a target LDOS from the quasiparticle current data of a superconducting probe is in general a complicated task, due to the singular shape of the probing BCS DOS. Nevertheless, the presence of the superconducting gap is helpful in preserving the energy selectivity when performing transport spectroscopy at temperature values approaching the critical temperature, and is particularly suitable for measuring the precise width of an energy gap in the target LDOS.

Interaction with the photonic environment

We conclude this section by mentioning important effects related to the interaction between tunneling events and the electromagnetic degrees of freedom of the surrounding environment. As a consequence of the nanoscopic design size¹⁶ of metallic tunnel probes, the resulting oxide junctions are characterized by a capacitance C with typical values in the fF range. This, coupled with the discrete nature of the tunneling process, leads to the appearance of a junction *charging energy* $E_c = e^2/2C$, which may very well not be negligible with respect to the thermal energy scale

¹⁵ A requirement of interest, e. g., for ensuring no undesired local heating of the quasiparticles during the operation of the probe.

¹⁶ This feature is often sought after to obtain a good degree of spatial selectivity in mesoscopic transport experiments.

in cryogenic environments¹⁷. The basic manifestation of the charging energy is associated with the well known Coulomb blockade effect in double barrier, quantum dot and single electron transistor systems, where tunnel transport is suppressed at low temperatures for bias voltages within the Coulomb gap $V_g = e/C$.

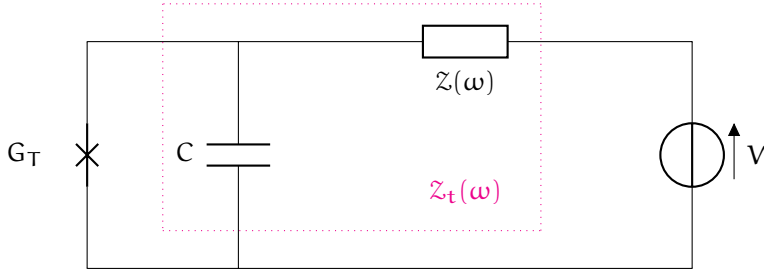


Figure 1.12: Lumped element diagram describing the equivalent circuit for the interaction between a tunnel junction characterized by non-negligible charging energy and a generic environmental impedance $Z(\omega)$. The physical junction is characterized by tunnel conductance G_T and capacitance C . The whole circuit is biased at voltage V by an external ideal source. A dotted magenta box indicates the total impedance $Z_t(\omega) = 1/[i\omega C + Z^{-1}(\omega)]$, whose real part determines the photon emission probability via eqs. (1.38) and (1.39).

In the case of a single low-capacitance tunnel junction the static Coulomb blockade theory can be extended considering the junction in series with a frequency dependent impedance describing a generic dissipative environment [27]. This arrangement is shown in fig. 1.12 as a lumped-element electrical circuit, where the physical junction is represented as the parallel of a capacitor and an ideal tunnel element. Physically, the interaction between the degrees of freedom of the junction and the environment affects both quasiparticle and Cooper pair

¹⁷ For a junction characterized by a 1 fF capacitance the charging energy is $E_c \approx 80 \mu\text{eV}$; this indicates that effects related to this energy scale are not washed out by thermal fluctuations for temperature values below 1 K.

tunnel transport characteristics. These phenomena fall under the broad denomination of *dynamical Coulomb blockade* effects.

A Hamiltonian representation of the coupling between the junction and the dissipative environment can be performed by considering the environment as a collection of LC oscillators, whose eigenfrequency and inductance values are chosen so to reproduce a given environmental impedance. The tunneling rates are then derived by perturbative expansion with respect to the matrix elements coupling the two leads. From a physical point of view, the interaction between the tunneling charge carriers and the environment can be fully described in terms of the photon emission probability energy distribution, which can be obtained as the Fourier transform:

$$P(\varepsilon) = \frac{1}{2\pi\hbar} \int_{-\infty}^{+\infty} \exp \left[J(t) + \frac{i}{\hbar} \varepsilon t \right] dt, \quad (1.38)$$

where $J(t)$ is the charge carrier phase-phase correlation function, and ε is the energy of the interacting photon (positive in case of emission and negative for absorption).

In the zero-temperature limit no photons are present in the LC bath and $P(\varepsilon)$ is non-zero only for positive values of its argument. The interaction between the charge on the tunnel junction and the environment is dependent on the value of the total inductance $\mathcal{Z}_t(\omega)$, shown in fig. 1.12 as the parallel of the junction capacitor and the environmental impedance $\mathcal{Z}(\omega)$. The phase-phase correlation function can be obtained from the dissipative part of the total inductance as

$$J(t) \approx 2 \int_0^{+\infty} \frac{d\omega}{\omega} \frac{\Re[\mathcal{Z}_t(\omega)]}{R_0} [\exp(-i\omega t) - 1], \quad T \rightarrow 0, \quad (1.39)$$

where the value of the reference resistance R_0 depends on the nature of the charge carriers: when considering electron tunneling the scaling resistance is equal to the von Klitzing constant $R_0 = R_K = h/e^2$, whereas for Cooper pairs $R_0 = R_K/4$.

In case of electron carriers, the forward tunneling rate under Direct Current (DC) voltage bias can be computed, for a given $P(\varepsilon)$ in the Fermi golden rule approximation:

$$\Gamma(V)^+ = \frac{G_T}{e^2} \iint dE_1 dE_2 \rho_1(E_1) \rho_2(E_2 + eV) \times \quad (1.40)$$

$$\times g(E_1) [1 - g(E_2 + eV)] P(E_1 - E_2).$$

The total quasiparticle current is obtained by summing backwards and forward rates, yielding:

$$I_{qp}(V) = \frac{G_T}{e} \iint dE_1 dE_2 \rho_1(E_1) \rho_2(E_1 + E_2) \frac{1 - \exp(-\frac{eV}{k_B T})}{1 - \exp(-\frac{E_2}{k_B T})} \times \quad (1.41)$$

$$\times [g(E_1) - g(E_1 + E_2)] P(eV - E_2),$$

which appropriately reduces to eq. (1.34) in the $E_c \rightarrow 0$ limit, where $P(\varepsilon) \rightarrow \delta(\varepsilon)$.

In case of Cooper pair tunneling, the perturbative expansion of the total Hamiltonian is performed with respect to the Josephson energy $E_j = \hbar I_c / 2e$, which describes the amplitude of the coupling of the superconducting condensates across the oxide barrier. In this case the forward tunneling rate under DC voltage bias is directly proportional to the photon emission probability:

$$\Gamma(V)^+ = \frac{\pi}{2\hbar} E_j^2 P(2eV), \quad (1.42)$$

yielding the total supercurrent

$$I_S(V) = \frac{\pi e}{\hbar} E_j^2 [P(2eV) - P(-2eV)]. \quad (1.43)$$

Review [27] provides worked examples to reconstruct the $P(\varepsilon)$ distribution from common environment impedances, including resistive, inductive and transmission lines. For illustrative purposes, we report the main results concerning the coupling between the tunnel junction

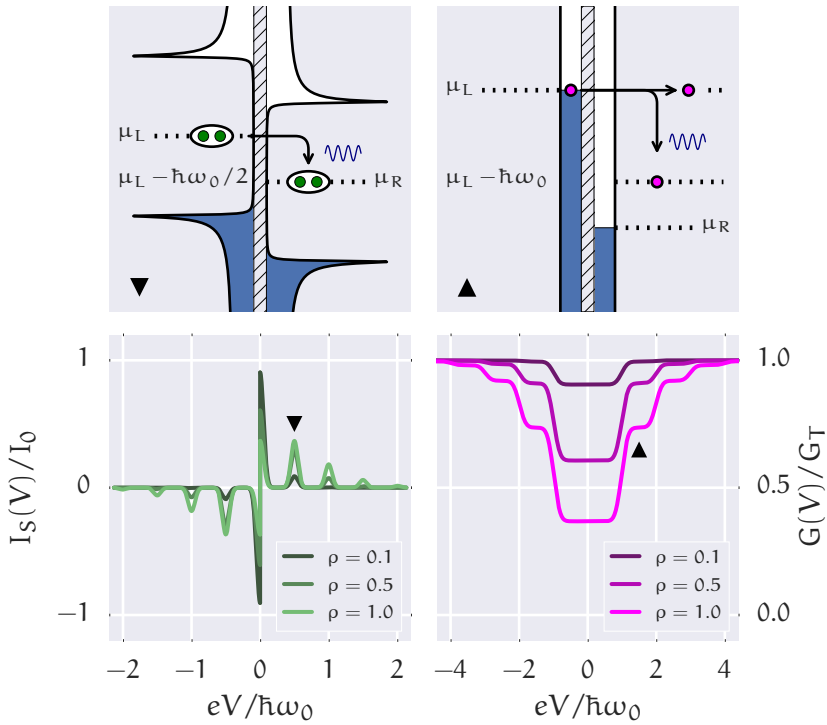


Figure 1.13: Energy alignment diagrams (top panels) and calculated transport characteristics (bottom panels) for Cooper pair and quasiparticle transport in SIS and NIN tunnel junctions (left and right panels, respectively) in inductive environments at zero temperature. The coupling results in a single-mode resonator whose fundamental frequency is ω_0 and the photon emission probability $P(\varepsilon)$ is Poissonian with parameter ρ (see text). The resonating peaks in $P(\varepsilon)$ have been artificially broadened for clarity in the displayed characteristics, where G_T is the tunnel conductance and $I_0 = \pi\Delta G_T/2e$ is the Ambegaokar-Baratoff critical current amplitude. Voltage bias conditions are indicated by matching symbols between the upper and lower panels.

and a single photonic mode, corresponding to an inductive environment. The total impedance $\mathcal{Z}_t(\omega)$ is given by the parallel of the junction capacitance C and the environmental inductance L . The resulting resonator is characterized by a photonic fundamental mode with energy $\hbar\omega_0 = \hbar/\sqrt{LC}$. The zero-temperature photon emission probability is:

$$P(\varepsilon) = \exp(-\rho) \sum_{k=0}^{\infty} \frac{\rho^k}{k!} \delta(\varepsilon - k\hbar\omega_0), \quad (1.44)$$

where the parameter ρ for the Poissonian distribution is:

$$\rho = \frac{E_c}{\hbar\omega_0} \frac{R_K}{R_0} = \frac{\pi}{R_0} \sqrt{\frac{L}{C}}. \quad (1.45)$$

Figure 1.13 shows the effects of a moderate ($\rho \leq 1$) single-mode photonic coupling on Cooper pair tunneling in a **SIS** tunnel junction (left panels) and on quasiparticle tunnel transport in a **NIN** junction (right panels) at zero temperature. In the case of the **SIS** junction, net transport of a Cooper pair at non-zero voltage is only possible when the work done by the voltage source matches the energy transferred to the photonic resonator. As a result, with increasing ρ , supercurrent peaks appear at voltage values $V_k = k\hbar\omega_0/2e$. This situation is depicted in the top left alignment diagram for the case of photon emission in the fundamental mode ($k=1$). This specific voltage bias is marked with a downwards facing triangle in the bottom left panel of fig. 1.13, where the $I_S(V)$ characteristics are shown for different values of the coupling parameter ρ .

An important difference between quasiparticle and Cooper pair tunneling is that in the former the charge carriers can tunnel to high energy states and then relax non-radiatively towards the chemical potential level in the sink electrode; on the contrary, Cooper condensates do

not provide a similar kinetic buffer¹⁸. For a **NIN** tunnel junction in the zero-temperature limit eq. (1.41) simplifies to

$$I_{qp}(V) = \frac{G_T}{e} \int_0^{eV} d\varepsilon (eV - \varepsilon) P(\varepsilon), \quad (1.46)$$

and differentiation with respect to voltage yields the differential conductance

$$G_N(V) = G_T \left(1 - \int_{e|V|}^{+\infty} P(\varepsilon) d\varepsilon \right). \quad (1.47)$$

For quasiparticle transport, the photonic coupling induces a breakdown of the total tunnel conductance in partial transport windows which are cumulatively activated with increasing voltage bias. The full tunnel conductance $G(V) = G_T$ is restored with $V \gg E_c/e$. The top right panel of fig. 1.13 shows the energy alignment diagram in which electrons at the chemical potential in the left electrode tunnel into the right electrode either elastically or with the emission of one photon of energy ε . The non-radiative relaxation to the chemical potential in the right electrode is not explicitly pictured. This specific voltage bias is marked with an upwards facing triangle in the bottom right panel of fig. 1.13, where the differential conductance characteristics are shown for different values of the coupling parameter ρ .

1.7 DIFFUSIVE WEAK LINKS

This section focuses on weak links where the supercurrent is mediated by elements characterized by metallic-like conductance in the normal state. Although this category also includes ballistic conductors, the specific target of the forthcoming discussion is metallic conductors in the *diffusive* limit, i. e., where the electronic elastic mean free path is negligible compared with the spatial extent of the conductor; the latter

¹⁸ This is the fundamental reason for the direct proportionality in eq. (1.42) between Cooper pair transfer rates and photon emission probability.

is also assumed to be shorter than the phase-coherence length of the charge carriers at low enough temperature.

Weak links based on diffusive domains in direct contact with the superconducting electrodes are the high-transparency counterpart to the tunnel barrier junctions analyzed in the previous section. They are typically realized by sequential metallic thin film depositions under high vacuum conditions to ensure the absence of oxide layers at the interfaces between different metals. To reach a given critical current value, due to the difference in the typical surface conductivity of tunnel barriers with respect to clean metallic contacts, short weak links based on the latter would require a smaller cross section, leading to stronger supercurrent concentration compared to a SIS junction.

Due to the non-trivial nature of the weak link medium, supercurrent transport in such structures is parametrically affected by geometrical and intrinsic degrees of freedom beyond the normal-state conductance of the metallic channel¹⁹. In a scattering-matrix picture, a diffusive element is composed of an ensemble of electron propagation paths, each characterized by a specific length and transparency. As anticipated in section 1.5, the spectrum of the supercurrent-carrying standing modes is broadened by propagation-dependent dephasing along each conduction pathway; spectral observables are then expected to be parametrically dependent from both the diffusive channel length and the average traversal timescale.

The spatial character intrinsic in phase-coherent diffusion processes is indeed reflected in the denomination “*proximity effect*”, the term collectively describing phenomena related to the penetration of superconducting correlations in normal metal domains. In the following, the basic phenomenology of *proximized* finite-length diffusive domains is presented with specific focus on the phase response of the electronic states inside the weak link and of the supercurrent transport associated to them. To this end, a quasi one-dimensional picture is assumed,

¹⁹ Moreover, the presence of intrinsic electron states in the channel provides the opportunity for direct manipulation of their distribution function beyond equilibrium; exotic states such as the π -shifted Josephson junction [28] have been demonstrated in this way.

meaning that no physical quantities are expected to vary along the dimensions transverse to the weak link axis. Additionally, the electrodes are considered at the same electric potential and the electron states in the diffusive channel are assumed to be in thermal equilibrium.

As a starting point in the understanding of the phenomenology of diffusive weak links it is helpful to consider their short-length limit: the *diffusive point contact*. In such a structure the effect of the diffusion is simply to scramble the direction of electronic momenta [15, 16], without introducing phase shifts due to negligible traversal time inside the weak link. As a consequence, the diffusive point contact can be described as a collection of zero-length ABSs whose transparency values are picked from the arcsine distribution

$$\zeta(\tau) = \frac{1}{\pi\sqrt{\tau(1-\tau)}}, \quad (1.48)$$

to model the effect of the momentum direction scrambling on transmission probability. The top right and left panels of fig. 1.14, show respectively the statistical distribution of τ values and a qualitative depiction of its effect on the spectrum of ABSs; in the latter, green and red shades indicate ground and excited branches, while the intensity of the color shading is proportional to the local probability of occurrence of the specific $E_\tau(\theta)$.

The collective CPR can be obtained in consistence with eq. (1.30) as the statistically weighted average of eq. (1.27)

$$\frac{I_S(\theta)}{I_0} = \int_0^1 d\tau \zeta(\tau) \frac{\sin \theta}{\sqrt{1 - \tau \sin^2 \frac{\theta}{2}}} \tanh \left(\frac{\Delta \sqrt{1 - \tau \sin^2 \frac{\theta}{2}}}{2k_B T} \right), \quad (1.49)$$

where the current magnitude scale $I_0 = \pi\Delta G_N/2e$ is defined in analogy with the nomenclature adopted for the single ABS and for tunnel junctions; here the proper conductance reference scale is given by G_N , the

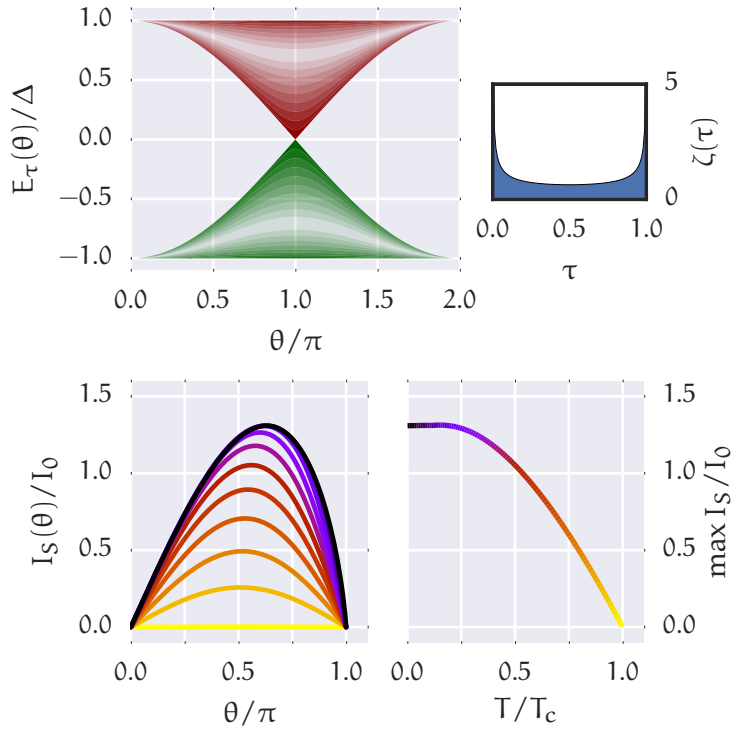


Figure 1.14: Phase and temperature response of the supercurrent in a diffusive point contact. The top left panel shows the energy distribution of the phase-modulated spectrum of an ensemble of ABSs; in the latter the individual transparency values τ are sampled from the arcsine distribution shown in the upper right panel. The lower left panel shows the temperature-dependent CPRs obtained by integrating eq. (1.49); here the temperature values span the $0 \rightarrow T_c$ range in even $T_c/10$ steps. The bottom right panel shows in matching colors the temperature dependence of the maximal supercurrent of the diffusive point contact. All current values are normalized to $I_0 = \pi\Delta_0 G_N/2e$, where Δ_0 is the zero-temperature superconducting gap at the electrodes and G_N is the normal state conductance of the point contact.

normal state conductance in the normal state. Evaluating the integral leads to the following expression for the CPR

$$\frac{I_S(\theta)}{I_0} = \sum_{n=0}^{+\infty} \frac{8k_B T \cos \frac{\theta}{2}}{\sqrt{(\Delta \cos \frac{\theta}{2})^2 + \omega_n^2}} \arctan \left(\frac{\Delta \sin \frac{\theta}{2}}{\sqrt{(\Delta \cos \frac{\theta}{2})^2 + \omega_n^2}} \right), \quad (1.50)$$

where $\omega_n = \pi k_B T (2n + 1)$ are the Matsubara frequencies. This limiting form is usually referred to as the *Kulik-Omelyanchuk dirty model* [29], after the authors who originally derived it. The resulting temperature-dependent CPRs traces are shown in the bottom left panel of fig. 1.14; the corresponding maximal supercurrent values as a function of temperature are shown on the bottom right panel, with matching color coding to indicate the temperature value. The shape of the CPR is markedly non-harmonic except for relatively high temperature values; the normalized critical current at zero temperature is slightly larger than the corresponding value for a SIS junction.

Attempting the theoretical description of hybrid systems beyond the short-length limit requires the adoption of a microscopic framework able to treat spatially inhomogeneous superconductors. The solution of the quantum many-body problem is typically attempted within a Green's function-based description in the Nambu particle-hole space [30]. With these tools it is possible to derive the set of Gor'kov equations [31–33] which incorporates the effects of the pair potential as well as chemical inhomogeneities at the atomic scale.

In order to reach a numerically treatable complexity for the analysis of mesoscopic weak links, the Gor'kov equations can be approximated to a quasiclassical level based on the insight that the characteristic length scales in superconductivity are much larger than the Fermi wavelength. Equations resulting from this quasiclassical approximation are due to Eilenberger [34] and they can be further simplified as a consequence of the isotropy of diffusive processes in metallic weak links. The whole of these approximations is known as the Usadel quasiclassical framework

for the diffusive (or “dirty”) limit [35]. A comprehensive treatment on the matter, also including non-equilibrium effects, can be found in [36].

Under the assumption of thermal equilibrium, the quasiclassical treatment reduces to the following matrix equation for the retarded Green’s function:

$$\hbar D \nabla \left(\hat{\mathcal{G}}_R \nabla \hat{\mathcal{G}}_R \right) = \left[-i \varepsilon \hat{\tau}_3 + \hat{\Delta}, \hat{\mathcal{G}}_R \right], \quad (1.51)$$

where D is a coefficient quantifying the strength of diffusive processes, $\hat{\tau}_3$ is the third Pauli matrix in electron-hole space and

$$\hat{\Delta} = \begin{pmatrix} 0 & \Delta e^{i\phi} \\ \Delta e^{-i\phi} & 0 \end{pmatrix}. \quad (1.52)$$

Here Δ and ϕ are respectively the amplitude and the phase of the superconducting order parameter; they are real scalar functions of the position in the diffusive channel.

A possible choice is to parametrize the $\hat{\mathcal{G}}_R$ matrix as

$$\hat{\mathcal{G}}_R(\varepsilon, \mathbf{x}) = \begin{pmatrix} \cosh \Theta & i \sinh \Theta e^{iX} \\ i \sinh \Theta e^{-iX} & -\cosh \Theta \end{pmatrix}, \quad (1.53)$$

where $\Theta(\varepsilon, \mathbf{x})$ and $X(\varepsilon, \mathbf{x})$ are complex scalar functions of energy and position along the diffusive channel (respectively, ε and \mathbf{x}). The rationale is that hyperbolic trigonometry allows describing a position-dependent “rotation” between a normal and a BCS-like form for the $\hat{\mathcal{G}}_R$ matrix while providing a means of natively incorporating the characteristic hyperbolic energy dependence of a BCS condensate. With this parametrization choice eq. (1.51) yields the following equations:

$$\begin{aligned} \hbar D \partial_{\mathbf{x}}^2 \Theta &= -2i \left[\varepsilon \sinh \Theta - \Delta \cos(\phi - X) \cosh \Theta \right] + \\ &+ \hbar D (\partial_{\mathbf{x}} X)^2 \sinh(\Theta) \cosh(\Theta), \end{aligned} \quad (1.54)$$

and

$$\hbar D \partial_{\mathbf{x}} j_E = -2i \Delta \sin(\phi - X) \sinh \Theta, \quad (1.55)$$

where $j_E = -(\partial_x X) \sinh^2 \Theta$. In analogy with eq. (1.1), inside the diffusive domain with a non-zero effective interaction, the shape of the $[\Delta(x), \phi(x)]$ profile is determined by the integral equation

$$\Delta e^{i\phi} = \frac{\lambda}{4} \int_{-\infty}^{+\infty} \left[\sinh \Theta e^{iX} + \sinh \bar{\Theta} e^{i\bar{X}} \right] \tanh \left(\frac{\varepsilon}{2k_B T} \right) d\varepsilon, \quad (1.56)$$

where the overline symbol indicates complex conjugation. This latter equation is to be solved self-consistently with eqs. (1.54) and (1.55), being dependent on both Θ and X .

Equations (1.54) to (1.56) define a second-order partial derivative equation set, whose solution is in general attempted numerically. For the problem to be well-defined, this set of equations has to be supplemented by appropriate boundary conditions to model the interfaces between the diffusive channel and the surrounding reservoirs. The parametrization of the $\hat{\mathcal{G}}_R$ matrix takes the following form in an ideal reservoir:

$$\begin{cases} \Theta_S = \operatorname{arctanh} \left(\frac{\Delta}{\varepsilon} \right), X_S = \phi & \text{superconducting reservoir,} \\ \Theta_N = 0, X_N = 0 & \text{normal reservoir.} \end{cases} \quad (1.57)$$

First-order boundary conditions, derived by Kupriyanov and Lukichev [37], complement eq. (1.57) in the problem definition [16, 36]:

$$\begin{cases} \mp r \sinh \Theta \partial_x X = \sin(X - X_{\mp}) \sinh \Theta_{\mp} \\ \mp r \partial_x \Theta = \sinh \Theta \cosh \Theta_{\mp} - \cos(X - X_{\mp}) \cosh \Theta \sinh \Theta_{\mp} \end{cases}, \quad (1.58)$$

where quantities marked by the \mp symbol refer to the values taken according to eq. (1.57) at the left (−) and right (+) contacts across the SN interface; here the characteristic length scale of the spatial derivative of Θ and X at the boundaries is $r = R_b/R_0$, the barrier resistance normalized to the channel resistance per unit length. Conditions in eq. (1.58) are actually the low-transparency limiting form of more general boundary conditions [38]. However, they have been found to be reasonably predictive also in the high-transparency limit [39]. The impact of interface resistivity and per-channel transparency in superconducting

weak links based on diffusive elements has been extensively analyzed [40, 41]. In the following, unless otherwise specified, we assume rigid superconducting boundaries with ideal transparent interfaces ($r \simeq 0$).

A successful solution of the Usadel equations yields the physical observables of interest. The local quasiparticle DOS can be directly obtained from the real part of the first diagonal element in \hat{G}_R (the *normal* component):

$$\rho(\varepsilon, x, \theta) = \Re [\cosh \Theta] . \quad (1.59)$$

Notably, for a bulk superconductor $\Theta = \operatorname{arctanh}(\Delta/\varepsilon)$ and eq. (1.59) identically yields eq. (1.2). On the other hand, the off-diagonal elements in eq. (1.53) (the *anomalous* component) determine the energy distribution of supercurrent-carrying states. The spectral current is the imaginary part of j_E , introduced in eq. (1.55) in its specific $[\Theta, X]$ parametrization form. In its general form, the spectral current is defined as:

$$\mathcal{J}_{sp} = \Im [j_E] = \frac{1}{4} \operatorname{Tr} \left[\hat{\tau}_3 \left(\hat{G}_R \nabla \hat{G}_R - \hat{G}_A \nabla \hat{G}_A \right) \right] , \quad (1.60)$$

where $\hat{G}_A = -\hat{\tau}_3 (\hat{G}_R)^\dagger \hat{\tau}_3$ is the matrix representation of the advanced Green's function. Equation (1.60) explicits the balance between forward and backward supercurrent transport. The CPR for a diffusive superconducting weak link can then be calculated as

$$\begin{aligned} I_S(\theta) &= -\frac{G_N}{2e} \int \mathcal{J}_{sp}(\varepsilon) \tanh \left(\frac{\varepsilon}{2k_B T} \right) d\varepsilon \\ &= \frac{G_N}{2e} \int \Im \left[(\partial_x X) \sinh^2 \Theta \right] \tanh \left(\frac{\varepsilon}{2k_B T} \right) d\varepsilon . \end{aligned} \quad (1.61)$$

Here, for a diffusive channel of length L , the value of the integral is dependent on the phase difference $\theta = \phi(L) - \phi(0)$ and, although not immediately evident from the form of the integral²⁰, is constant along the x variable as a consequence of current conservation.

²⁰ With the exception of proximized normal metal, in which the $\partial_x j_E = 0$ by virtue of eq. (1.55), being $\Delta = 0$.

In the following and throughout the rest of the thesis, numerical solutions to the Usadel equations, as well as the relative physical observables, have been obtained with the open-source `usadel1` software package [42].

Normal-metal diffusive channel

Applying the Usadel framework to the analysis of SNS systems is important for the understanding of the interplay between the superconducting and diffusive dynamics. To this end, a key observation is that the coefficients in eq. (1.51) fix a natural energy scale for the diffusive process: the *Thouless energy*. This quantity is defined as $E_{\text{Th}} = \hbar D/L^2$, where L is the length of the diffusive channel²¹.

On the other hand, the obviously natural energy scale for superconducting phenomena is the value of the superconducting gap. Since for a normal metal domain one can assume $\lambda = 0$, eq. (1.56) is trivially satisfied with an identically zero $\Delta(x)$ profile inside the diffusive channel. As a consequence, all Δ -proportional terms disappear from eqs. (1.54) and (1.55). The superconducting energy scale only manifests itself at the electrode boundaries, where the Θ , X functions and their first spatial derivatives are constrained to link to their bulk superconducting forms.

Figure 1.15 shows the quasiparticle LDOSs obtained from the numerical solutions of the Usadel equations for three SNS weak links of increasing length in the zero-temperature limit. The LDOS shown in the top left panel corresponds to the case of $E_{\text{Th}} = \Delta_0$, where Δ_0 is the zero-temperature superconducting gap in the electrodes. From the colormap it can be seen that inside the channel the width of the gap in the quasiparticle excitation spectrum is only slightly perturbed with respect to the superconducting electrodes; this corresponds to an effectively *short* diffusive channel. The top right panel corresponds to an

²¹ For typical metallic thin films, D takes values in the range $1 - 100 \text{ cm}^2/\text{s}$; the corresponding $E_{\text{Th}} \in 1 - 1000 \text{ } \mu\text{eV}$ for lengths of practical mesoscopic interest.

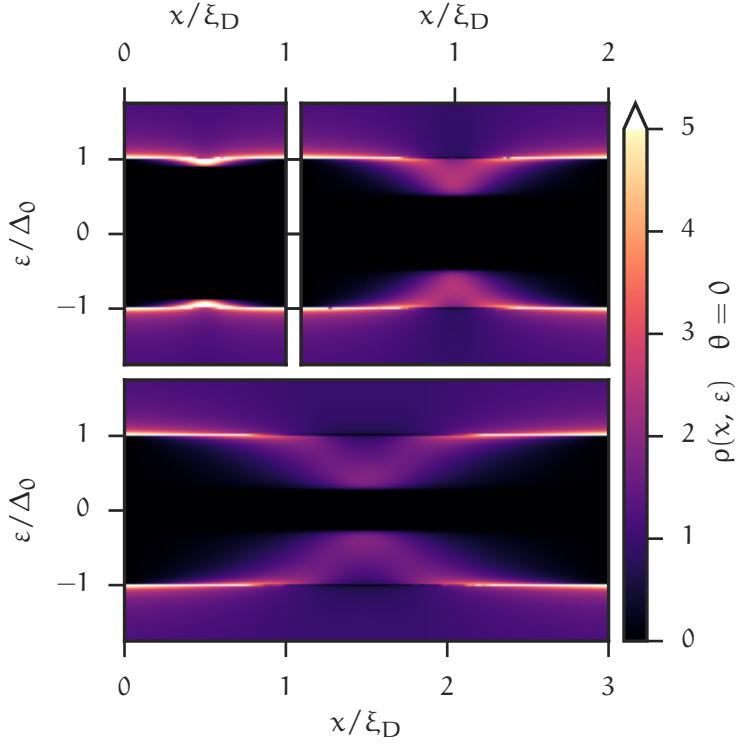


Figure 1.15: The colormap plots represent the normalized zero-temperature LDOS $\rho(x, \varepsilon)$ inside proximized normal weak links with linearly increasing length (top left, top right and bottom colormaps), corresponding to short, intermediate and long regimes. The width of each colormap panel is approximately proportional to the corresponding channel length value. The spatial coordinate x (horizontal colormap axes) is shown as normalized with respect to the coherence length $\xi_D = \sqrt{\hbar D / \Delta_0}$, where Δ_0 is the zero-temperature superconducting gap at the electrodes. The latter quantity also provides the normalization factor for the energy coordinate ε (vertical colormap axes). Zero phase bias is applied at the electrodes ($\theta = 0$).

intermediate-length channel, with $E_{\text{Th}} = \Delta_0/4$; in this case, the spatial character of the diffusive dynamics can be appreciated from the shape of the quasiparticle **LDOS**. In the latter, the extent of the gap is halved with respect to the electrodes. Finally, the *long* regime is illustrated by the bottom panel, where $E_{\text{Th}} = \Delta_0/9$. In this case the shape of the corresponding quasiparticle excitation spectrum is severely affected, and its energy gap is furtherly suppressed.

Overall these results illustrate that the impact of diffusive dynamics on the spectral properties of the proximized system can be quantified by the value of the Δ_0/E_{Th} ratio. A corresponding diffusive coherence length, defined as $\xi_D = \sqrt{\hbar D/\Delta_0}$, describes the spatial extent of the penetration of superconducting correlations inside the normal metal domain. Consequently, diffusive **SNS** weak links are classified in terms of their *normalized length* $l = L/\xi_D = \sqrt{\Delta_0/E_{\text{Th}}}$.

Beside length, the **LDOS** of a proximized weak link is affected by the superconducting phase difference enforced at its boundaries. This phase-driven modulation is shown in fig. 1.16 for the short, intermediate and long regimes described above (respectively, top, middle and bottom panels). Each plot shows the shape of the quasiparticle **LDOS** in the central part of the diffusive normal domain as a function of the applied phase difference. As the latter is increased from $\theta = 0$ to $\theta = \pi$ the corresponding $\rho(\varepsilon)$ is modified resulting in a progressive suppression of its energy gap. Notably, all proximized systems revert to a constant quasiparticle **DOS** in their center for $\theta = \pi$, independently of their length.

A non-zero phase gradient along the diffusive wire is associated with a finite supercurrent. Evaluation of eq. (1.61) in the zero temperature limit yields the normalized **CPRs** shown in the left panel fig. 1.17 for **SNS** weak links of different normalized lengths. All the curves are non-harmonic, and the critical current values I_c are quickly suppressed with increasing length. The latter property is due to the fact that in the long **SNS** regime the Thouless energy replaces Δ_0 as the characteristic scale for the $eI_c R_N$ product.

The right panel of fig. 1.17 shows the temperature dependence of the normalized critical current of the **SNS** weak links. It can be noted

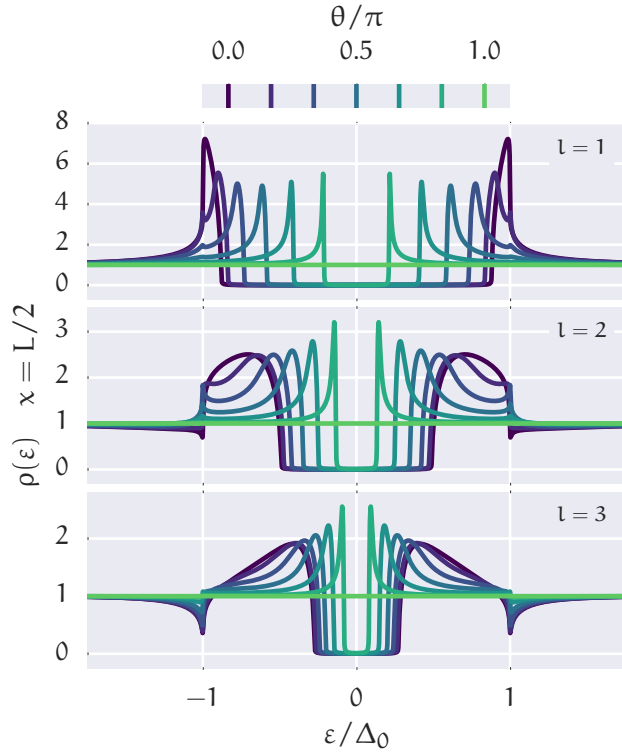


Figure 1.16: Phase-driven modulation of the LDOS $\rho(\varepsilon)$ in the center of a proximized normal weak link ($x = L/2$). The top, middle and bottom panels correspond respectively to normalized length values $l = 1, 2, 3$. Each plotted curve is relative to an applied phase difference θ in the range $0 \rightarrow \pi$, in even $\pi/6$ steps. The corresponding θ values are shown in matching colors in the bar at the top of the figure.

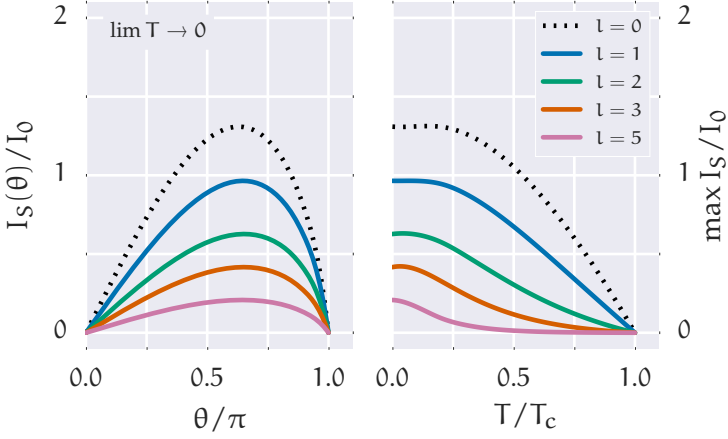


Figure 1.17: The left and right panels show respectively the zero-temperature CPRs and the temperature dependence of the critical current in SNS weak links of normalized length $l = 0, 1, 2, 3, 5$. The zero-length limit, corresponding to the diffusive point contact, is shown as a dotted line. All current values are normalized to $I_0 = \pi\Delta_0 G_N/2e$, in analogy with the nomenclature adopted for tunnel-type junctions.

that while short weak links show an almost linear suppression of their critical current with temperature, the long diffusive regime is instead characterized by an exponential damping. The latter is consistent with the following analytical model [43], valid in the $E_{Th} \ll k_B T < \Delta$ limit.

$$I_c(T) = \frac{32}{3 + 2\sqrt{2}} \frac{E_{Th}}{eR_N} \sqrt{\left(\frac{2\pi k_B T}{E_{Th}}\right)^3} \exp\left(-\sqrt{\frac{2\pi k_B T}{E_{Th}}}\right), \quad (1.62)$$

where T is the electron temperature in the proximized normal domain²². The exponential suppression is parametrized by the ratio L/ξ_T , where $\xi_T = \sqrt{\hbar D/2\pi k_B T}$ is the *thermal* diffusive coherence length. Equation (1.62) is actually the first term of the Matsubara summation

$$I_c(T) = \frac{64\pi k_B T}{eR_N} \sum_{n=0}^{+\infty} \frac{\sqrt{\frac{2\omega_n}{E_{Th}} \Delta^2} \exp\left(-\sqrt{\frac{2\omega_n}{E_{Th}}}\right)}{\left[\omega_n + \Omega_n + \sqrt{2(\Omega_n^2 + \Omega_n \omega_n)}\right]^2}, \quad (1.63)$$

where $\omega_n = \pi k_B T(2n + 1)$ and $\Omega_n = \sqrt{\Delta^2 + \omega_n^2}$. This extended form provides an appropriate model for the temperature dependence of the critical current for SNS weak links when $E_{Th} \simeq \Delta \ll k_B T$, which is the case, e. g., when approaching the critical temperature of the superconducting electrodes [43]. In this case the full evaluation of the Matsubara summation is required to reproduce the linear collapse of the critical current in the vicinity of the superconducting-to-normal transition.

Superconducting diffusive channel

We conclude both this section and this chapter by extending the analysis of diffusive weak links to superconducting channels. This entails using the open-source `usadel1` software package to solve the Usadel equations assuming $\lambda > 0$ inside the diffusive channel. As a consequence of the self-consistency eq. (1.56), a non-zero superconducting order parameter is present all along the channel, while its boundary values are enforced by the superconducting electrodes. In the following we present results corresponding to an identical λ (i. e., identical BCS critical temperature) between the electrodes and the diffusive channel. The boundary interfaces are assumed to be ideally rigid and transparent.

²² Note that at sub-Kelvin temperature the latter quantity need not coincide with the bath temperature or with the quasiparticle temperature in the superconducting electrodes, due respectively to the low-temperature suppression of the electron-phonon coupling and to the negligible thermal conductance of superconducting contacts.

In analogy with the SNS case, diffusive SSS weak links can be classified according to their normalized length [15, 16]. In the *short* regime, physical observables are dominated by the electrodes. This case is illustrated in fig. 1.18 for a SSS weak link of unit length in the zero temperature limit.

In the figure, the top left panel shows the spatial dependence of the absolute value of the order parameter; here different curves correspond to the bias points marked in the CPR presented in the top right panel. The bottom panel shows the quasiparticle LDOS in the center of the superconducting wire for the same biasing conditions. Dark blue colors correspond to the linear phase-response regime, close to the $\theta = 0$ CPR node; in this case the absolute value of the order parameter is approximately constant and the supercurrent is directly proportional to the gradient of the phase. On the other hand, close to the $\theta = \pi$ node (green curves), the collapse of both the order parameter and the supercurrent is accompanied by the quasiparticle LDOS reverting to the normal-state form. Overall, the shape of the CPR is barely different from the zero-length limit represented by eq. (1.50); in the present case, however, the weak link itself hosts an actual superconducting condensate whose quasiparticle LDOS is BCS-like, with an energy gap which is fully modulated by the phase difference applied at the electrodes.

In the *long* limit the intrinsic superconducting properties of the diffusive wire are expected to take over with respect to the electrodes. When this is the case, multiple solutions of the Usadel equations may be compatible with the applied boundary constraints, namely the phase difference at the electrodes. Still, a one-to-one mapping between physical observables and the curvilinear coordinate spanning the locus of the CPR can be found.

The transition between the short and the long regime is illustrated by fig. 1.19. Here, the left and right panels show, respectively, the zero-temperature CPRs and the temperature dependence of the normalized critical current for SSS weak links of different normalized lengths. It can be noted that the transition to the long regime is characterized

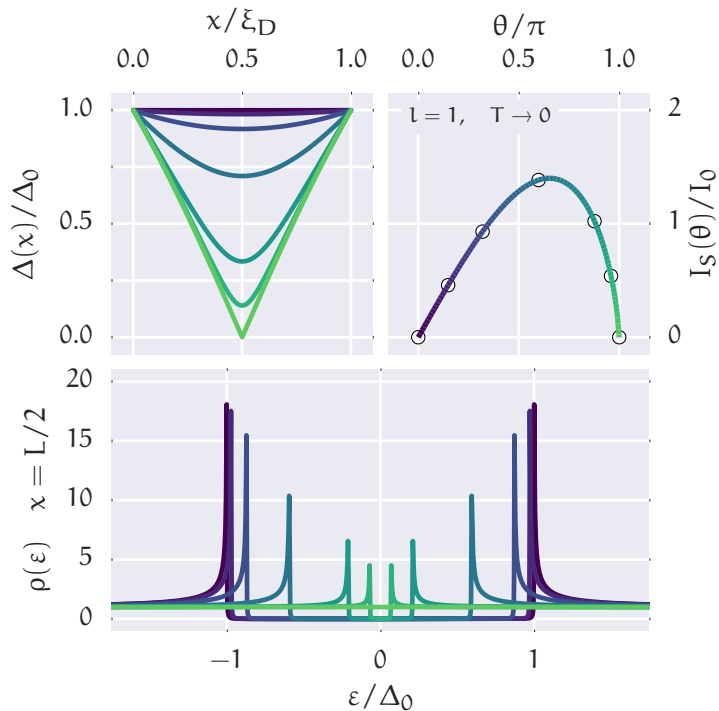


Figure 1.18: The top left, top right and bottom panels show the phase-driven modulation of, respectively, the self-consistent $\Delta(x)$ profile, the CPR and the LDOS in the center of a short ($l = 1$) SSS weak link in the zero-temperature limit. In both top left and bottom panels, different curves refer in matching colors to the points marked on the CPR curve shown in the top right panel.

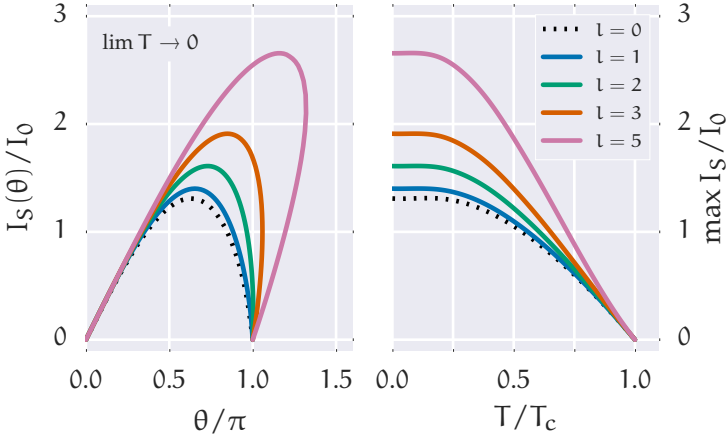


Figure 1.19: The left and right panels show respectively the zero-temperature CPRs and the temperature dependence of the critical current in SSS weak links of normalized length $l = 0, 1, 2, 3, 5$. The zero-length limit, corresponding to the diffusive point contact, is shown as a dotted line. All current values are normalized to $I_0 = \pi\Delta_0 G_N/2e$, in analogy with the nomenclature adopted for tunnel-type junctions.

by increasing values of the normalized critical current²³, while the normalized Josephson inductance²⁴ in the linear phase-response regime ($\theta \approx 0$) is independent of the wire length, being equivalent to the intrinsic kinetic inductance per unit length.

The results for a long (normalized length $l = 5$) superconducting wire are shown for the zero-temperature limit in fig. 1.20. The anomalous CPR locus shown in the top right panel displays the skewing distur-

²³ This is due to the fact that for long wires the critical current for the wire will converge to its intrinsic value, while the normalization constant I_0 , proportional to the normal state conductance, will decrease with increasing wire length.

²⁴ I.e., the reciprocal of the derivative of the normalized CPR.

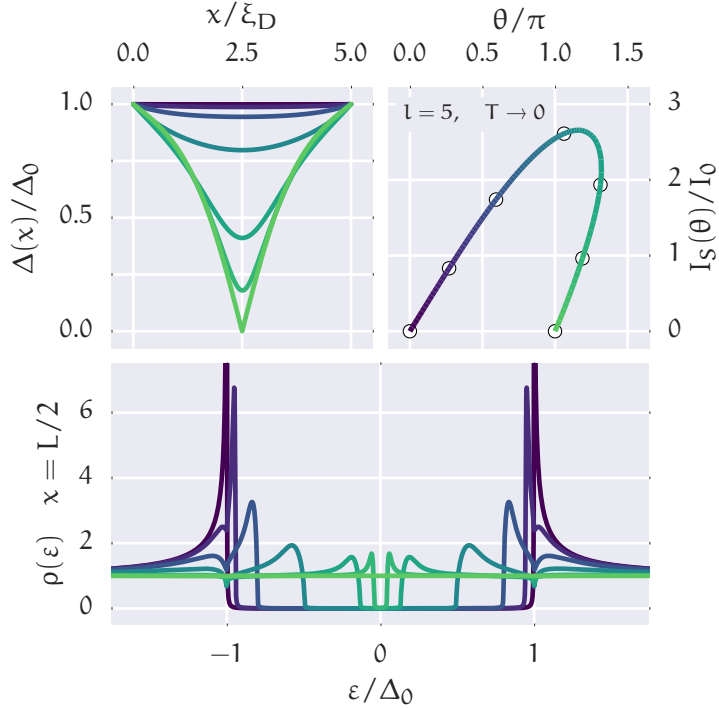


Figure 1.20: The top left, top right and bottom panels show the phase-driven modulation of, respectively, the self-consistent $\Delta(x)$ profile, the CPR and the LDOS in the center of a long ($l = 5$) SSS weak link in the zero-temperature limit. In both top left and bottom panels, different curves refer in matching colors to the points marked on the CPR curve shown in the top right panel.

tion typical of the long regime. The top left and bottom panels show respectively the spatial dependence of the absolute value of the order parameter and the quasiparticle LDOS in the middle of the wire for the bias conditions marked in the CPR locus. It can be appreciated that due to the skewing a phase difference $\theta > \pi$ can be established by *current biasing* the wire close to its critical current. However, the locus branch between this point and the $\theta = \pi$ node is inaccessible both by current and phase biasing techniques. The LDOS curves shown in the bottom panel are markedly different from their almost-BCS counterparts of fig. 1.18. They have been experimentally characterized by means of transport spectroscopy in [44], where the distortion of the singularity peaks at the edge of the gap as well as its suppression is proven to be a consequence of the increasing value of the spatial gradient of the superconducting phase.

For all weak link types considered in this chapter (ballistic ABSs, tunnel junctions, diffusive systems) non-zero temperature values affect the thermal balance of forward and backwards supercurrent transport channels²⁵ that determine the CPR. However, in SSS weak links thermal excitation also plays a direct role in the spectral equations, namely in the self-consistency eq. (1.56).

For a superconducting wire in the long regime a sufficient increase in temperature can revert the anomalous CPR locus to a single-valued functional $I_S(\theta)$ dependence. This can be appreciated in the left panel of fig. 1.21, which shows the evolution of CPR loci with increasing temperature for a SSS weak link of normalized length $l = 5$. The actual temperature marking the transition between anomalous and single-valued CPR can be discovered by monitoring the evolution of the normalized inductance at the $\theta = \pi$ node. The latter quantity is defined as $\mathcal{M}_\pi = I_0(dI_S/d\theta)^{-1}$, and its thermal evolution is shown in the right panel of fig. 1.21, where a star-shaped marker at $\mathcal{M}_\pi = 0$ indicates the transition. The latter occurs for $T \approx 0.7 T_c$ for the $l = 5$ SSS weak link.

²⁵ In fact, eqs. (1.27), (1.30), (1.31), (1.49) and (1.61) implement the specific form of eq. (1.24) for each weak link type.

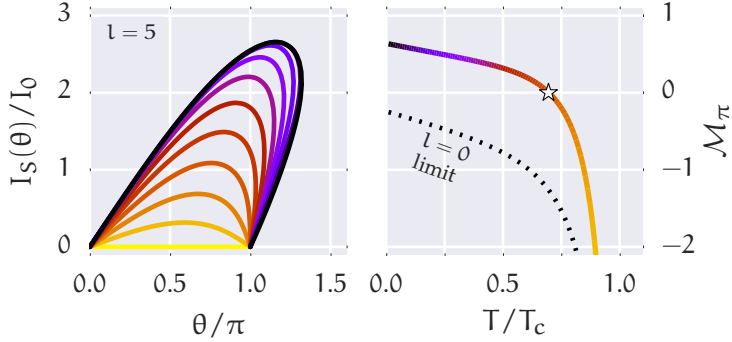


Figure 1.21: The left panel shows the temperature-driven transition from multi-valued to single-valued CPR for a long ($l = 5$) SSS weak link. The plotted CPR curves are relative to temperature values spanning the $0 \rightarrow T_c$ range in even $T_c/10$ steps. The right panel shows the corresponding temperature dependence of the normalized inductance $\mathcal{M}_\pi = I_0(dI_S/d\theta)^{-1}$, evaluated at the π -node of the CPR. A star-shaped marker at $\mathcal{M}_\pi = 0$ indicates the transition between the multi-valued and the single-valued regime. For the zero-length limit, shown as a dotted line, the value of \mathcal{M}_π is negative in the whole temperature range, consistently with the single-valuedness of the corresponding CPR.

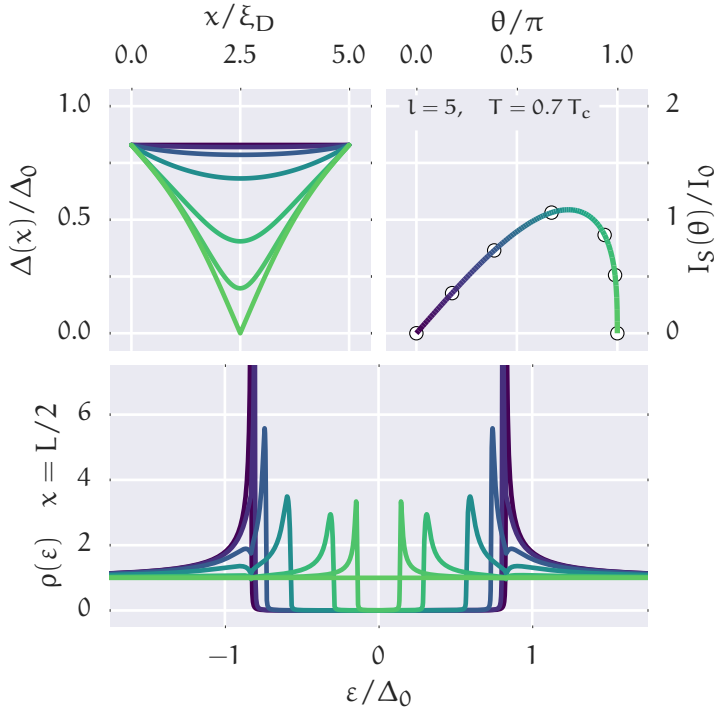


Figure 1.22: The top left, top right and bottom panels show the phase-driven modulation of, respectively, the self-consistent $\Delta(x)$ profile, the CPR and the LDOS in the center of a long ($l = 5$) SSS weak link at $T = 0.7T_c$. In both top left and bottom panels, different curves refer in matching colors to the points marked on the CPR curve shown in the top right panel.

Figure 1.22 shows results for the $l = 5$ SSS weak link at the quoted reversal temperature for its CPR, shown in the top right panel. Direct comparison with the corresponding zero-temperature results in fig. 1.20 indicates that the absolute value of the order parameter at the electrodes is only slightly suppressed with respect to its zero-temperature value. Similarly to the case of a short SSS weak link, spanning the applied phase bias to $\theta = \pi$ induces the progressive and full closing of the energy gap in the LDOS, accompanied by the collapse of the supercurrent towards the π node of the CPR. On the other hand, traces of the *long* diffusive nature of the weak link can be appreciated in the broadened peaks at the gap edges as well as the appearance of additional DOS features for $\varepsilon \approx \pm\Delta$.

EXPERIMENTAL PROTOCOLS

2.1 SAMPLE FABRICATION

The devices presented in this thesis consist in micro-structured networks of metallic domains, whose interfaces can be either clean galvanic contacts or metal-oxide barriers. They have been realized by directional thin-film deposition through an Electron-Beam Lithography (EBL)-defined mask (or stencil) suspended at a fixed distance above the substrate, a nanofabrication technique known as suspended mask lithography [45], whose basic steps are illustrated in fig. 2.1.

The target for the lithography is prepared by spin-coating a silicon substrate¹ with a positive-tone EBL resist bi-layer. The latter consists in a Methyl MethAcrylate (MMA)-MethAcrylic Acid (MAA) copolymer *spacer* layer topped by a conventional Poly-(Methyl MethAcrylate) (PMMA) *stencil* layer. The following recipe has been found to reliably yield a 100 nm-thick PMMA stencil and a 700 nm-thick copolymer spacing layer.

1. Clean the wafer in acetone, rinse with IsoPropyl Alcohol (IPA), blow-dry with nitrogen.
2. Pre-baking: 5 min on the hotplate @ 120 °C, 2 min cool-off
3. Spacer resist² spin-coating: 1500 RPM for 90 s
4. Spacer curing: 15 min on the hotplate @ 170 °C, 2 min cool-off
5. Stencil resist³ spin-coating: 3500 RPM for 45 s
6. Stencil curing: 15 min on the hotplate @ 170 °C, 2 min cool-off

¹ A 80 mm Si-[100] wafer capped by a 250 nm-thick thermally-grown SiO₂ layer.

² Microchem MMA(8.5)MAA Copolymer (13% in ethyl lactate)

³ Microchem 950-kD PMMA EBL resist (4% in anisole)

The wafer is then cleaved in individual chips suitable for the subsequent fabrication steps.

The electron exposure is performed by EBL-adapted field emission Scanning Electron Microscope (SEM) columns⁴, where the electron beam is accelerated to 30 keV and reaches typical beam waist values as low as ≈ 5 nm. Pattern generator software⁵ drives the deflection coils in the SEM columns to expose the bi-layer according to the required dose pattern. The copolymer layer is fully exposed by a dose of $150 \mu\text{C}/\text{cm}^2$; the stencil layer requires $400 \mu\text{C}/\text{cm}^2$ to $700 \mu\text{C}/\text{cm}^2$, depending on the size of the patterned feature.

The resist development is performed in a 1:3 by weight solution of Methyl IsoButyl Ketone (MIBK):IPA at 20 °C for 30 s, stopped in pure IPA. The difference in exposure sensitivity for the two layers results in a developed resist structure similar to the one shown in fig. 2.1a, where the spacer layer is broadly cleared out under the sharp patterning of the top stencil layer. The achievable linewidth resolution in patterning the latter actually benefits from the distance of the substrate, in that the low-energy secondary electrons backscattering from silicon diffuse through the spacer resist layer.

After development the sample is blow-dried by a gentle nitrogen flow and loaded in a custom ultra-high vacuum⁶ electron-beam evaporator for thin film deposition. The evaporator is equipped with multiple crucibles; the materials used for the devices presented in this thesis are listed in table 2.1. For each film layer, a 8 kV electron gun heats the contents of the appropriate crucible until evaporation. As a consequence of the ultra-low pressure, the evaporated beam propagates ballistically towards the patterned substrate, which is mounted on a tiltable sample holder. The latter enables directional deposition: the EBL pattern is cast onto the substrate with an angle-dependent offset, allowing for the realization of the complete device without the need of multiple

⁴ Zeiss Merlin and Ultraplus models.

⁵ Nanometer Pattern Generation System (JC Naby Lithography Systems); Elphy Quantum (Raith GmbH).

⁶ Typical chamber pressure: 1 nTorr, achieved with a continuous cryopumping ($T \approx 13$ K).

MATERIAL	GROWTH RATE ($\text{\AA}/\text{s}$)	PURITY	NOTES
V	10	2N	$T_c \approx 4 \text{ K}$
Al	2	5N	$T_c \approx 1.2 \text{ K to } 1.6 \text{ K}$
$\text{Al}_{0.98}\text{Mn}_{0.02}$	2	n/a	normal metal [46]
Cu	2	5N	normal metal
Ti	2	4N	adhesivant

Table 2.1: Catalogue of the metallic thin film depositions used in this thesis.

lithographic steps. The typical layer thickness is in the 15 nm to 200 nm range.

Superconducting-electrode tunnel junctions are obtained by exposing the surface of an Al layer⁷ to a pure oxygen atmosphere in the oxidation chamber for 300 s right after the evaporation; the thickness of the barrier, and consequently the value of the tunnel resistance can be tuned by controlling the oxygen pressure in the chamber⁸. The tunnel junction is completed by evaporating an overlapped metallic layer to form the second electrode.

A scanning electron micrograph of a detail in a fabricated device right after the evaporation process is shown in fig. 2.2. The three-dimensional structure of the bi-layer, including the undercut of the spacer layer and the patterning in the metal-covered suspended mask are particularly evident.

Beside the benefits related to its intrinsic self-alignment, the suspended mask nanofabrication protocol results in high quality metal-to-metal or metal-to-oxide contacts. This is granted by the sequential metal-

⁷ If a normal-metal electrode is required a Mn-doped Al layer is instead used (cfr. table 2.1).

⁸ Oxygen pressure values from 0.05 Torr to 1 Torr result in tunnel resistance-surface product in the 0.1 $\text{k}\Omega \mu\text{m}^2$ to 10 $\text{k}\Omega \mu\text{m}^2$ range.

lic depositions and oxidations being performed in controlled vacuum, without the need of exposing the sample to the ambient atmosphere.

These advantages come at the expense of a more challenging mask design process; in fact, care has to be taken in order to ensure the mechanical stability of tightly-packed suspended parts and to prevent unwanted short contacts between otherwise irrelevant deposition replicas. The latter is typically avoided by sensible spacing of the designed elements and by appropriately sculpting the undercut profile of the spacer resist layer to intercept problematic replicas⁹.

Finally, the finite thickness of the stencil layer (typically 100 nm) can be exploited to trim the width of deposited metallic wires beyond the linewidth resolution of the lithographic process. This can be achieved by evaporating at a finite angle with the tilting axis parallel to the desired wire; the resulting cast feature will be trimmed by the partial occlusion of the slit patterned on the stencil, as seen by the impinging beam of evaporated material.

After the deposition of all required layers, the fabrication is concluded by removing the resist and the excess metal in a warm acetone bath, followed by rinsing in IPA and blow-drying the substrate. The latter is then glued with GE varnish to a ceramic Dual In Line (DIL) chip carrier and wire bonded¹⁰ for the subsequent characterization.

⁹ This solution is pictured in fig. 2.1b, where the leftmost deposited feature does not come into contact with the substrate, and will be washed away during the lift-off step.

¹⁰ Ultrasonic wedge bonding with 25 μm -thick Al wire.

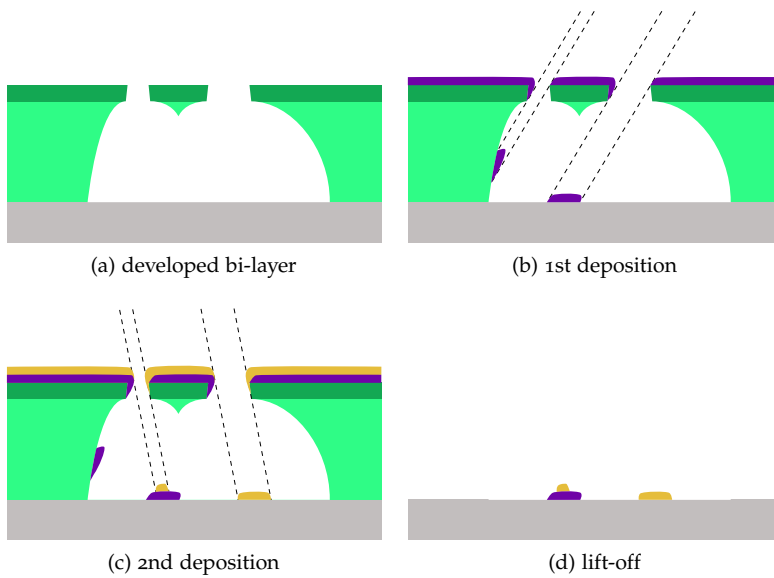


Figure 2.1: Summary of suspended mask nanofabrication. The sequence (a-d) represents, in section, the multi-stage deposition of metallic thin films (purple, orange) on a substrate (gray) through a suspended stencil mask (dark green). Different substrate offsets allow the realization of devices of hybrid composition within a single lithographic step.

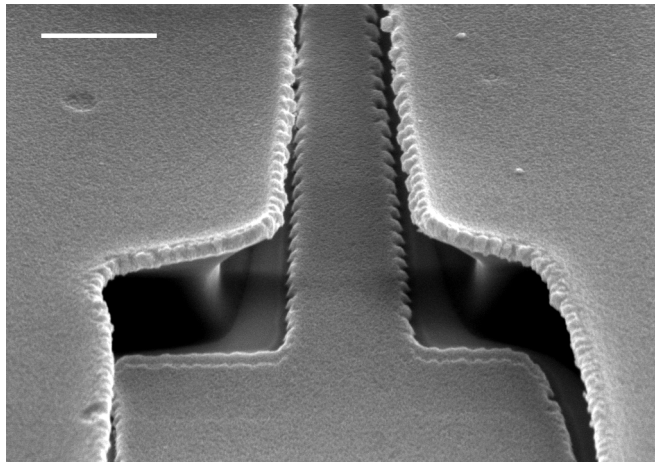


Figure 2.2: Tilted scanning electron micrograph of the suspended mask after the evaporation process. The horizontal scale bar corresponds to $1\ \mu\text{m}$.

2.2 LOW-TEMPERATURE MEASUREMENTS

The magneto-electric characterization of the devices presented in this thesis has been performed in two cryogenic Oxford Instrument setups: a pumped ^3He dewar insert (model *Heliox*) and a cryofree dilution refrigerator (model *Triton 200*).

Heliox setup

This refrigerator is designed to operate as a brass vacuum can insert for 75 L liquid helium dewars. During operation, the primary cooling mechanism consists in the forced evaporation of liquid helium from the 1 K pot, a small vessel located inside the vacuum can of the insert. This element is continuously replenished by a capillary feed line dipped in the dewar and is able to reach temperature values as low as 1.2 K.

The insert is equipped with a sealed ^3He -filled circuit, composed of a tank, a charcoal sorption pump, a condensing neck and a ^3He pot vessel in thermal contact with the sample space. After the initial cool-down of the insert, the sorption pump is electrically heated to 30 K, releasing ^3He gas; at the same time the primary cooling power of the 1 K pot is exploited in the condensing neck to liquefy the ^3He which then collects by gravity in the ^3He pot.

After all the ^3He has been condensed (fig. 2.3), the heating of the sorption pump is deactivated. This initiates the forced evaporation of the contents of the ^3He pot, lowering the sample space temperature to 240 mK. For typical heat loads, up to 60 h of uninterrupted measurements at base temperature are possible before the ^3He pot is completely depleted by the sorption pump. The overall liquid helium consumption from the dewar averages at approximately 6 L/d.

A resistance bridge monitoring the resistance variation of a calibrated ruthenium oxide sensor allows to measure the temperature of the sample. The latter can be stabilized in the 0.25 K to 2 K range by a closed-loop Proportional, Integral and Derivative (PID) controller operating on a resistive heater on the ^3He pot. A magnetic field up to 20 mT can be

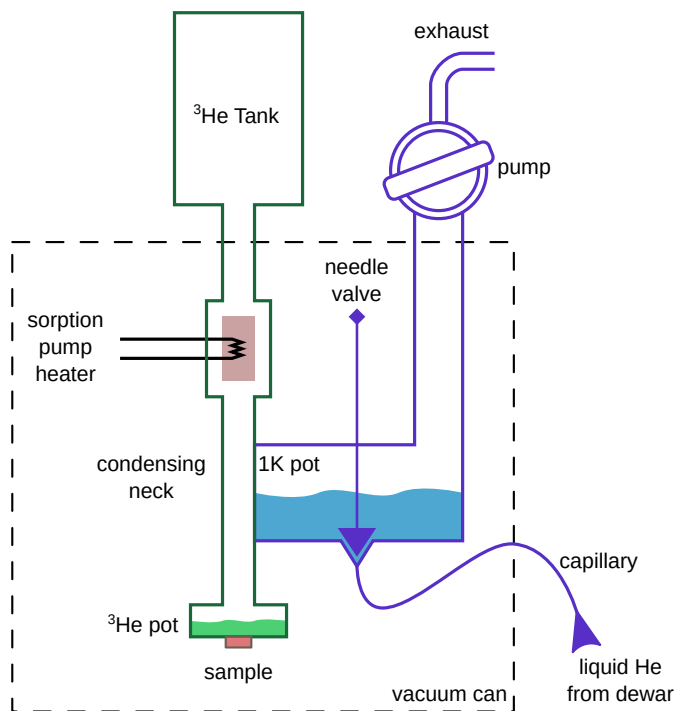


Figure 2.3: Functional schematic of the Heliox refrigerator. The latter is represented after a successful condensation of ^3He in the ^3He pot.

applied to the sample space by a custom-built superconducting magnet threaded to the brass vacuum can of the insert.

The *Heliox* setup is equipped with 16 audio-band measurement lines connecting a Bayonet Neill–Concelman (BNC) breakout box to a 16-pin DIL chip socket with conventional cryogenic loom wiring. The latter is thermalized by mechanical clamping at the 1 K pot level; the lines are filtered by a two-pole RC stage¹¹ on copper-lined Printed Circuit

¹¹ $C = 47 \text{ nF}$, $R = 510 \Omega$

Board (PCB) thermalized at the ^3He pot. Shielding from external Radio Frequency (RF) sources is provided by π -filters in the breakout box. Sample-level RF shielding is ensured by a copper Faraday cage with pass-through LC π -filters¹² enclosing the DIL socket.

Triton 200 setup

This continuous-cycle refrigerator, proposed [11, 47] by H. London in 1962, bases its operation on the endothermic character of the forced diffusion of ^3He atoms across the physical interface between a ^3He -rich phase and a ^3He -poor phase in a $^3\text{He}/^4\text{He}$ mixture. The interface occurs as a consequence of the spontaneous phase segregation of sufficiently rich $^3\text{He}/^4\text{He}$ mixtures at temperature values lower than the tricritical point¹³.

Throughout the circuit (fig. 2.4) the injected gas is progressively thermalized to its cold counterflowing path by appropriate heat exchangers. This cooling mechanism is somewhat equivalent to the forced evaporation of a cryogenic fluid; however, the minimum temperature of operation that can be reached in practice is limited only by the total ^3He circulating rate and by the thermalization efficiency of the counterflow exchangers. The sample space is thermalized to the mixing chamber.

The *Triton 200* setup is able to reach a base temperature of approximately 15 mK, with a cooling power of 200 μW at 125 mK. The primary cooling mechanism (exploited for the liquefaction of the incoming ^3He flux) for this refrigerator is provided by a pulse tube cooler¹⁴. The latter is a dual-stage cryocooler able to provide up to 1 W of cooling power at its 4 K stage. The pulse-tube cryocooler is responsible for the cooling of the 50 K and 3 K plates and relative radiation shields, and provides the analogue to the pumped 1 K-pot of the conventional “wet” dilution systems. Heat removal from the pulse-tube head to the heat exchangers of a water-cooled compressor is mediated by a self-contained amount of he-

¹² Oxley FLT/P/5000, 5 nF

¹³ Approximately 0.87 K.

¹⁴ Cryomech model PT410

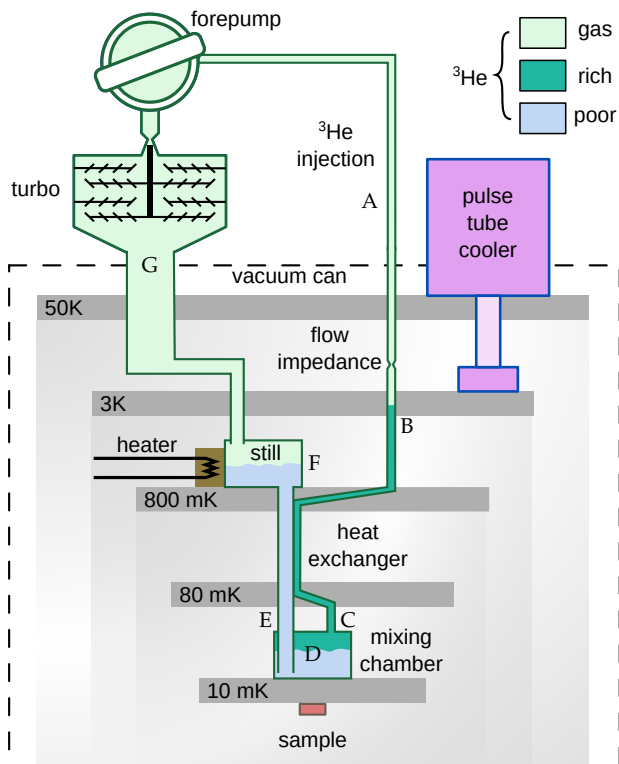


Figure 2.4: Functional schematic of a dry dilution refrigerator. The main circuit path for ^3He consists in the sequence: (A) *injection* into the impedance-limited lines; (B) *liquefaction* at the primary condensation point; (C) entering the mixing chamber (*rich phase*); (D) endothermic *dilution* inside the mixing chamber (*poor phase*); (E) leaving the mixing chamber (*poor phase*); (F) forced *evaporation* from the still; (G) pumping back into injection.

lium gas, so that its continued operation does not require replenishment of cryoliquids, hence its “dry” or “cryofree” denomination.

A resistance bridge monitoring the resistance variation of a ruthenium oxide sensor calibrated against a Johnson noise thermometer allows to measure the temperature of the mixing chamber. The latter can be stabilized up to 10 K by a closed-loop PID controller operating on a resistive heater on the mixing chamber. A magnetic field up to 400 mT can be applied to the sample space by a custom-built superconducting magnet thermally anchored to the still stage shield. The latter is energized by a precision current source (Keithley 2600 SMU) for noise-sensitive magnetic characterization.

The *Triton 200* setup is equipped (see fig. 2.5) with 24 audio-band measurement lines connecting a BNC breakout box to a 24-pin DIL chip socket with conventional cryogenic loom wiring. The latter is thermalized by mechanical clamping at each plate of the refrigerator; the lines are then filtered by a two-pole RC lowpass¹⁵ on copper-lined PCB thermalized at the mixing chamber. Shielding from external RF sources is provided by π -filters in the breakout box. Sample-level RF shielding is ensured by a copper Faraday cage with pass-through LC π -filters¹⁶ in series with high-rejection wideband lowpass filters¹⁷ enclosing the DIL socket.

2.3 LOW-FREQUENCY CHARACTERIZATION

In the present work, physical observables of interests have been probed by means of electrical characterization of the mesoscopic circuits obtained by the nanofabrication process detailed at the beginning of the present chapter. In particular, depending on the typical impedance of the devices under test, transport characteristics have been determined in either two-wire or four-wire probing setups. In both *Triton* and *Heliox* setups, the signal lines connecting the sample space to room-temperature

¹⁵ C = 47 nF, R = 1 k Ω

¹⁶ Oxley SLT/P/5000, 5 nF

¹⁷ Minicircuits VLFX-80.

electronics are designed to attenuate the high-frequency thermal radiation emitted by the latter, limiting the available signal bandwidth to approximately 1 kHz for low-impedance samples.

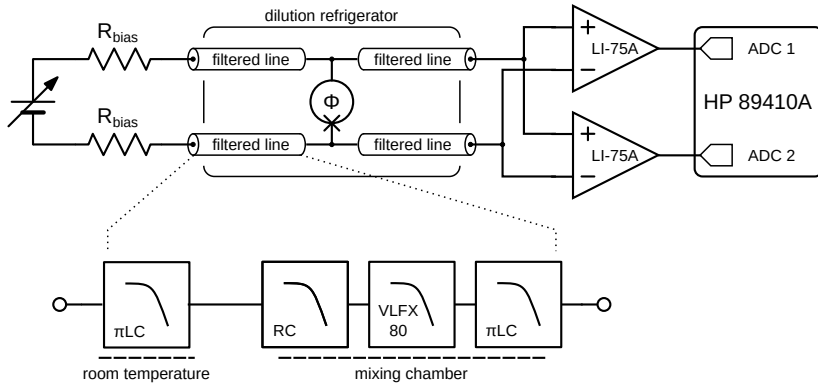


Figure 2.5: Functional schematic of a 4-wire measurement in the *Triton 200* setup. Each signal line is filtered by a combination of lowpass filters: feed-through LC, two-pole RC and high RF-rejecting multistage. In the particular case represented, the output of two low-noise differential preamplifiers (LI-75A) is digitized independently as the inputs of a vector signal analyzer (HP 89410A) for subsequent characterization of the spectral content of the signal.

Oxide-barrier junctions are typically characterized by tunnel resistance in the $10\text{ k}\Omega$ to $10\text{ M}\Omega$ range, and are thus suited to a two-wire voltage-biased characterization. Commonly used programmable voltage sources include Agilent HP 3245A, Stanford Research Systems SIM928, Yokogawa GS200. Room-temperature transimpedance preamplification (DL Instruments model 1211) provides the means for high-gain current to voltage transduction. Lock-in amplifiers (Stanford Research Systems SR830, NF Corporation LI-5640) have been used to record the differential conductance as a function of the applied voltage bias.

The characterization of low-impedance loads such as SNS weak links has been generally performed with a four-wire setup. The transport

characteristics are obtained by recording the voltage drop across the element as a function of the applied current bias. Low-noise room temperature differential preamplification (NF Corporation LI-75A) is used to boost the signal before digitization (Agilent 34470A). While low-noise differential preamplifiers are characterized by high values of common-mode noise rejection, their output is often affected by slow drift, i. e., significant low-frequency $1/f$ noise. To counteract this noise source, the current vs voltage curves were recorded via lock-in technique by measuring the first harmonic of the voltage response to a DC current bias chopped at a reference frequency significantly faster than the corresponding $1/f$ “drift” timescale¹⁸.

Some of the devices considered in the present thesis can be operated as magnetometers. For such applications, the noise-equivalent magnetic flux resolution has been deduced from the spectral characterization of the readout signal. One typical setup is represented in fig. 2.5, where the voltage response of a SQUIPT magnetometer under fixed current bias is amplified by two Low-Noise Amplifiers (LNAs) connected in parallel. The output of each LNA is digitized independently at each input Analog to Digital Converter (ADC) of a spectrum analyzer (HP 89410A), which computes both the Power Spectral Density (PSD) of each channel as well as the Cross-correlated Spectral Density (CSD) between the two. This characterization allows to distinguish the noise added by the amplification (which is assumed uncorrelated between two different battery-powered LNA units) from the spectral features (including the background noise floor) which are present before the amplification stage and are completely correlated between the two signal pathways.

¹⁸ The low impedance under test allows for undistorted square-wave bias and detection with reference frequency $f \approx 17$ Hz.

Part II

INVESTIGATIONS

The Superconducting QUantum Interference Device (**SQUID**) is a widely studied superconducting interferometer. Its typical structure (shown in fig. 3.1) consists in a superconducting ring interrupted by two Josephson junctions [12]. The combination of the Josephson effect [17] and magnetic flux quantization [18, 19] in a closed superconducting loop enforces the Φ_0 -periodic dependence of the phase difference values at the weak links with respect to the magnetic flux Φ coupled to the ring. The consequent modification of the *circulating* supercurrent can then be inferred by the periodic suppression of the maximal value of the *crosswise* supercurrent of the circuit constituted by the parallel of the two Josephson junctions [48].

The physical picture described above is at the core of **SQUID** magnetometry. State-of-the-art **SQUID** systems are typically able to resolve noise-equivalent magnetic flux levels lower than $1 \mu\Phi_0$ per unit bandwidth [49]. The vast majority of **SQUID** systems is based on **SIS** Josephson junctions, typically realized with Nb-AlOx multilayer thin film deposition techniques. These junctions are technologically attractive due to the comparatively high critical temperature and field of the Nb components, coupled with the long-term stability of AlOx tunnel barriers. Whole-wafer multilayer fabrication protocols directly result in high-throughput production of nearly identical devices where the main **SQUID** loops are integrated with inductively-coupled large-area input and feedback coils [49].

On the other hand, as discussed in chapter 1, the Josephson effect has been observed in a variety of weak links, well beyond **SIS** tunnel junctions. Structures such as superconducting constrictions, normal metal wires, ferromagnets, and even low-dimensional elements such as graphene, 2D electron gas, semiconducting nanowires, carbon nan-

otubes, atomic point contacts and quantum dots have been successfully engineered to support Josephson-like supercurrent transport between two Cooper condensates.

Here we consider the case of a SNS-based SQUID. The fundamental difference, compared to its SIS counterpart, is that in diffusive SNS weak links the transport of supercurrent depends non-trivially on the state of the internal degrees of freedom of the normal-metal element, which determine both the phase-dependent energy spectrum of ABSs and its occupation function (see sections 1.5 and 1.7). As a significant example, an exotic phenomenon such as the π -shifted junction¹ has been demonstrated by driving out of equilibrium the occupation of the Andreev states of a normal metal weak link [28].

From a more practical standpoint, SNS Josephson elements are of interest due to their intrinsic transparency, allowing the design of low-impedance devices, well suited for wide-bandwidth, low-noise readout. Furthermore, the negligible capacitance of typical SNS weak link geometries renders them immune to capacitive hysteresis phenomena that afflict SIS junctions. Finally, the high maximal current density supported in SNS weak links makes them interesting candidates for realizing compact Josephson junctions in interferometer geometries designed for nanoscale magnetometry [50, 51].

In this chapter we present the realization of micrometer-sized SQUIDs based on V/Cu/V SNS Josephson junctions. The rationale behind the choice of vanadium as superconductor includes its sizeable values in both critical field and critical temperature² and the possibility of performing the directional thin film deposition required for suspended mask evaporation. A previous publication [52] showed that Josephson coupling in V/Cu/V SNS junctions persists to temperature higher than 2 K thanks to the combination of a wide superconducting gap in the electrodes, a highly diffusive normal channel and favourably transparent galvanic contact between the two. The goal of this investigation is to

¹ I. e., a Josephson junction whose free energy minimum occurs for a phase difference equal to π .

² Up to approximately 4 K in thin films.

build upon this foundation to realize compact **SQUID** devices dedicated to magnetometry on the micrometer scale for subKelvin operation.

The chapter begins with the description of the supercurrent interferometry model for a **SQUID** based on Josephson junctions having sinusoidal **CPR**. The model adopted accounts for non-ideal effects such as asymmetry in the critical current values of the junctions and non-negligible ring inductance [49]. Next, the interferometric performance of the realized devices is evaluated in terms of the model. Finally the magnetometric performance of the best device is characterized and commented. The chapter is concluded by a summary of the main results.

3.1 SIMPLE MODEL FOR NON-IDEAL SQUID

The basic **SQUID** interferometer (see fig. 3.1) can be schematized as two Josephson junctions connected in parallel. The **CPR** of the junctions is assumed to be harmonic:

$$I_1(\theta_1) = I_o(1 - \alpha_1) \sin \theta_1, \quad (3.1)$$

$$I_2(\theta_2) = I_o(1 + \alpha_1) \sin \theta_2, \quad (3.2)$$

where I_k and θ_k respectively represent the supercurrent and the phase difference for the k -th junction. Potential asymmetry between the critical current values of the junctions is taken into account by the adimensional α_1 parameter, whereas I_o is the critical current per junction in the symmetric limit.

In order to quantitatively describe the zero-voltage state, it is useful to introduce the normalized crosswise and circulating supercurrent (respectively i and j). Current conservation dictates:

$$i \equiv \frac{I_1 + I_2}{I_o} = (1 - \alpha_1) \sin \theta_1 + (1 + \alpha_1) \sin \theta_2, \quad (3.3)$$

$$2j \equiv \frac{I_1 - I_2}{I_o} = (1 - \alpha_1) \sin \theta_1 - (1 + \alpha_1) \sin \theta_2. \quad (3.4)$$

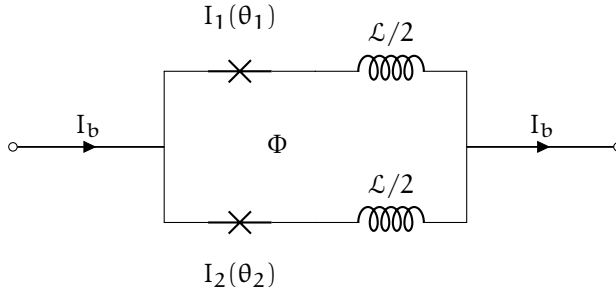


Figure 3.1: Functional diagram of a **SQUID** element. In the non-dissipative state, the **DC** current bias I_b applied *crosswise* to the element is carried by the two Josephson junctions according to eq. (3.3). The possible values of the pair of phase differences θ_1, θ_2 satisfy eqs. (3.4) and (3.5), and are parametrically dependent on the magnetic flux Φ applied to the **SQUID** ring of inductance \mathcal{L} .

The phase differences θ_1 and θ_2 are not mutually independent, due to the constraint of flux quantization. With an applied magnetic flux Φ coupled to the loop of the **SQUID**:

$$\theta_1 - \theta_2 = \frac{2\pi}{\Phi_0} (\Phi - \mathcal{L}I_o j) \equiv 2\pi \frac{\Phi}{\Phi_0} - \beta_{\mathcal{L}} j. \quad (3.5)$$

As elaborated in section 1.4, the presence of a finite loop inductance \mathcal{L} , results in a nonzero $\beta_{\mathcal{L}} = 2\pi\mathcal{L}I_o/\Phi_0$, which here causes the coupling between the equations describing circulating and crosswise supercurrent terms.

Generally, for a given value of Φ , there exists a range of values for θ_1, θ_2 (and consequently i, j) that satisfy eqs. (3.3) to (3.5). We define the positive and negative critical currents (I_c^\pm) as the extremal values of the crosswise supercurrent over all such constrained θ_1 and θ_2 pairs:

$$I_c^+(\Phi) = I_o \max_{\theta_1, \theta_2} i, \quad (3.6)$$

$$I_c^-(\Phi) = I_o \min_{\theta_1, \theta_2} i. \quad (3.7)$$

When subjected to a fixed current bias whose value exceeds the critical current, eqs. (3.3) to (3.5) cannot be simultaneously satisfied, and the device switches to the dissipative state, developing a finite voltage across its terminals. As a consequence, the phase difference of each junction evolves with time according to the second Josephson relation³.

In the ideal symmetric SQUID ($\alpha_I = 0$, $\beta_L = 0$) the value of the critical current can be found with simple trigonometric manipulations, yielding:

$$I_c^\pm(\Phi) = \pm 2I_o \left| \cos\left(\pi \frac{\Phi}{\Phi_0}\right) \right|. \quad (3.8)$$

For generic values of the α_I and β_L parameters the functional $I_c^\pm(\Phi)$ dependence must be numerically solved for. Figure 3.2 shows some illustrative cases. Ideal behaviour is characterized by full suppression of the critical current for $\Phi = (n + 1/2)\Phi_0$. As expected, the effect of an asymmetry in the supercurrent amplitudes of the single junctions (non-zero α_I) results in the impossibility of achieving a complete suppression of i when $\theta_1 - \theta_2 = \pi$. A finite inductance in the ring causes a screening effect on the applied flux: as a consequence even identical junctions cannot be fully biased to a phase difference equal to π . The corresponding $I_c^\pm(\Phi)$ trace shows non-zero critical current with a characteristic cusp for $\Phi = (n + 1/2)\Phi_0$. Finally, in devices characterized by both finite inductance and junction asymmetry, the combined non-idealities cause a skewing of the $I_c^\pm(\Phi)$ curve. In this case, the critical current minima are no longer located at $\Phi = (n + 1/2)\Phi_0$, and both $I_c^\pm(-\Phi) = I_c^\pm(\Phi)$ and $I_c^+(\Phi) = -I_c^-(\Phi)$ symmetries are characteristically broken.

³ Semiclassical approaches such as the simple time-dependent modelization introduced in section 1.3 may grant insight on the dynamics of Josephson junction networks, and have been used extensively to aid the design of practical superconducting electronic devices. It should be noted that a rigorous treatment of the time-dependent behaviour of such circuits requires an appropriate characterization of the electromagnetic environment of the junctions (up to sub-THz frequency range) in order to treat from first principles the charge-carrier/photon interaction.

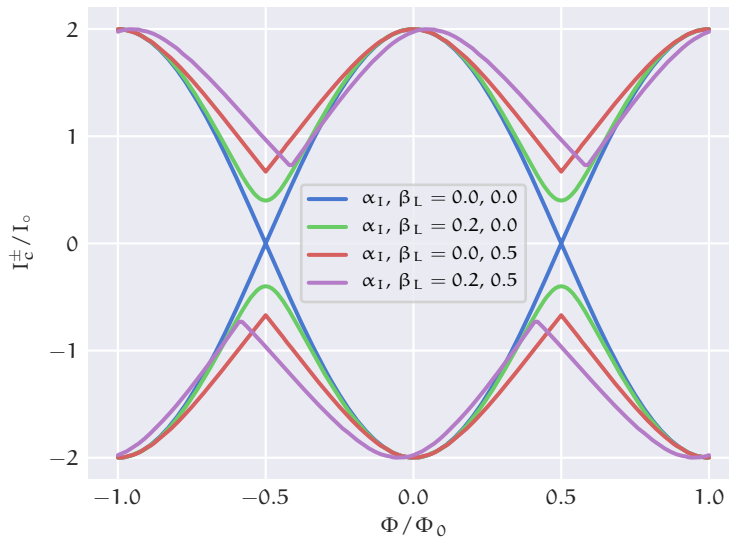


Figure 3.2: Critical current dependence with respect to applied magnetic flux for a two-junction SQUID in presence of junction asymmetry and non-zero loop inductance. The ideal behaviour is shown as a blue trace. Deviations from the ideal case are plotted as green and red trace, respectively for non-zero asymmetry and non-zero inductance. The magenta trace shows the combined effect of non-zero junction asymmetry and loop inductance.

3.2 INTERFEROMETER DESIGN AND CHARACTERIZATION

Although immune to *capacitive* hysteresis in their transport characteristics, current-biased SNS junctions may nevertheless suffer from hysteresis when switching from the supercurrent branch to a dissipative voltage state. This phenomenon is known to originate from the overheating of the quasiparticles in the proximized metal [53]. The latter can be observed at low temperature, when the suppressed efficiency of the quasiparticle cooling mechanisms⁴ makes them unable to compensate the heating induced by the Joule effect, present upon switching to a non-zero voltage state. Limiting the negative impact of the *thermal* hysteresis is the central challenge to address when designing magnetic detectors based on diffusive weak links [54, 55].

In our approach to this problem, we fabricated SQUID devices in which the SNS junctions are short yet resistive. In doing so, the typical Joule power in the dissipative state is kept as low as possible, without sacrificing a sizeable Thouless energy scale⁵ which is a prerequisite for a pronounced voltage modulation of the SQUID. In practice, we find that the latter requirement is satisfied by adopting copper weak links with interelectrode spacing in the 250 nm to 400 nm range, corresponding to Thouless energy values of several tens of μeV . At the same time, the typical dissipated power upon switching can be limited to few pW by reducing the cross-section of the SNS weak link to approximately $1000 (\text{nm})^2$, a value well within the limits of EBL-based nanofabrication techniques.

Figure 3.3 shows a scanning electron micrograph of a typical interferometer, fabricated by standard suspended mask technique⁶. A 5 nm-thick aluminium layer was first evaporated at 40° to ensure the adhesion of subsequent layers, followed by a copper layer of 20 nm at normal incidence and a final vanadium layer of 150 nm at 14° . The loop of the SQUID spans a surface of approximately $1.5 (\mu\text{m})^2$. In the

⁴ Namely, outdiffusion of hot quasiparticles and electron-phonon coupling.

⁵ See section 1.7, page 51.

⁶ Section 2.1.

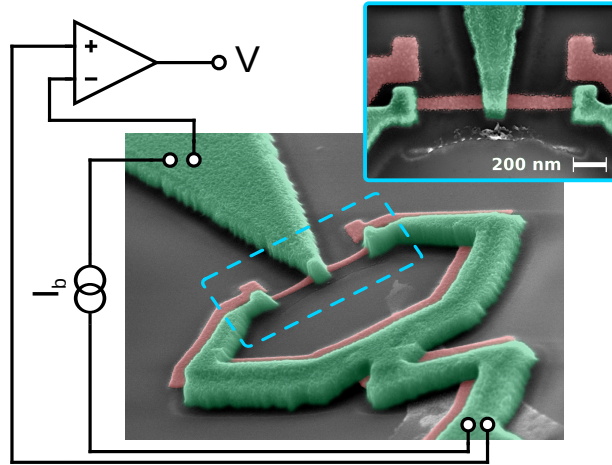


Figure 3.3: Tilted scanning electron micrograph showing a typical SQUID device in pseudocolors. Vanadium (green) and copper (red) films are 150 nm and 20 nm-thick, respectively. The standard setup for a 4-wire measurement is also displayed in the superimposed scheme. The inset in the top right corner shows a perpendicular zoomed view of the SNS junctions.

following, we compare results obtained for devices characterized by different normal-state resistance R_n , as summarized in table 3.1. The copper nanojunctions of device A (shown in the inset in fig. 3.3) are 60 nm and 370 nm in width and length, respectively; on the other hand, the junctions in devices B and C have been designed to be both shorter and wider, resulting in lower values of normal-state resistance.

Figure 3.4 shows the 4-wire current-voltage characteristics from device A measured at the base temperature of the *Heliox* setup⁷. The supercurrent branches are clearly modulated by the magnetic field applied to the loop. A small residual hysteresis of thermal origin is

⁷ Base temperature 240 mK; preamplifier offset drift eliminated via square-wave current biasing (see sections 2.2 and 2.3).

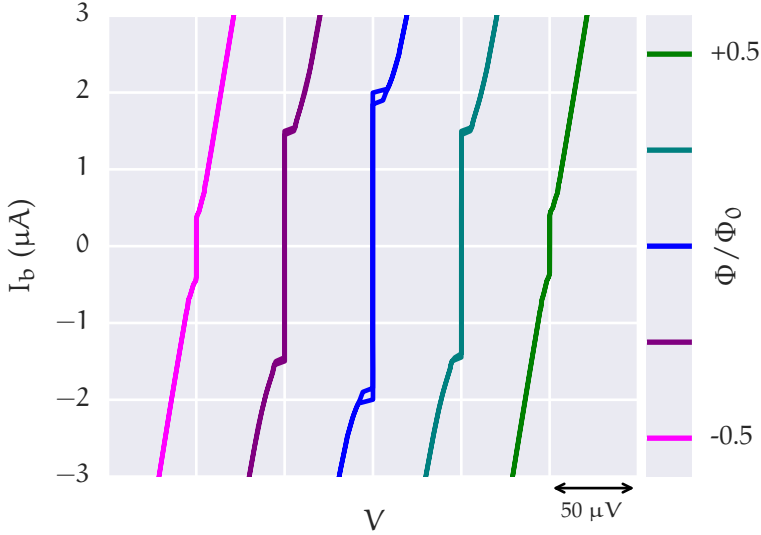


Figure 3.4: Magnetic flux-driven modulation of current-voltage characteristic curves for device A. The electric potential difference was measured in a 4-wire setup under fixed current bias I_b at cryostat bath temperature of 240 mK. The traces recorded for different values of the applied magnetic flux Φ are horizontally offset for clarity.

present in the characteristics for which the critical current $|I_c| > 1.5 \mu\text{A}$. As the bias current I_b exceeds I_c , the system switches to a resistive state developing a potential difference across the superconducting loop. For large bias currents ($I_b \gg I_c$), the characteristic curve can be approximated by $V \approx I_b R_n / 2$, allowing the estimation of the average junction's normal-state resistance and Thouless energy values, reported in table 3.1. Notably, we notice that the Thouless energy values are at least one order of magnitude smaller than the expected superconducting gap in the vanadium electrodes, all the SNS junctions considered here belong to the *long* diffusive limit.

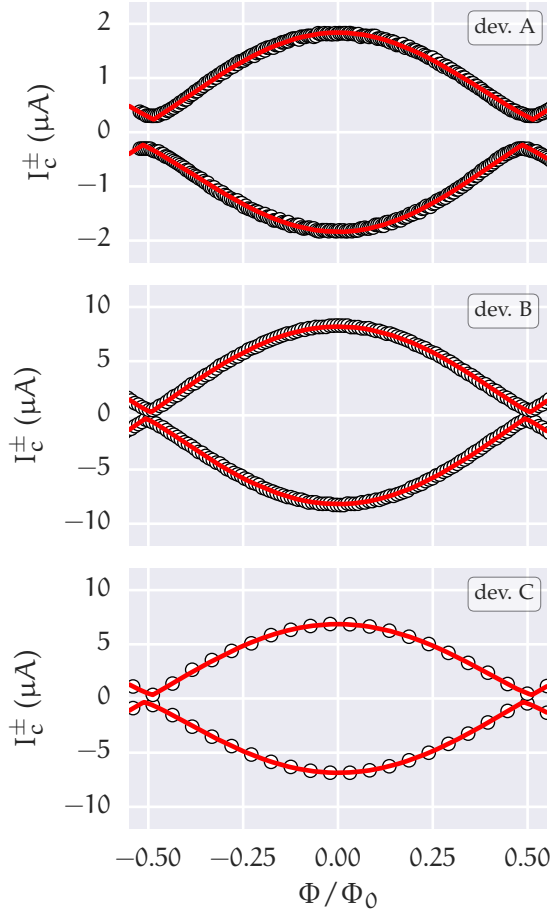


Figure 3.5: Magnetic flux dependence of the switching current (I_c^\pm) for three different V/Cu/V SQUIDs. Data point values (circles) have been extracted from the switching events in the current-voltage characteristics recorded at 240 mK. The red line is the best fit of eqs. (3.3) to (3.5) to experimental data. Values for the parameter estimates are reported in table 3.1.

DEVICE	L/W/t (nm)	R_n (Ω)	E_{Th} (μeV)	I_o (μA)	α_I	$\beta_{\mathcal{L}}$
A	370/060/20	14.0	27	0.97	0.04	0.44
B	300/150/20	3.6	51	4.10	0.03	0.13
C	280/150/20	3.0	65	3.43	0.06	0.09

Table 3.1: Summary of key parameters for the fabricated **SQUID** devices. Length, width and thickness of each copper wire in the **SNS** junctions are reported as L , W and t , respectively. The Thouless energy $E_{Th} = \hbar D/L^2$ has been deduced from the measured normal-state resistance R_n according to the Einstein relation $D = 1/(\rho_n \nu_F e^2)$, where ρ_n is the normal-state resistivity of the junction and $\nu_F = 1.56 \times 10^{47} \text{ J}^{-1} \text{ m}^{-3}$ is the density of states at the Fermi level for copper. Optimal estimates for I_o , α_I and $\beta_{\mathcal{L}}$ parameters have been obtained by fitting eqs. (3.3) to (3.5) to the experimental $I_c^{\pm}(\Phi)$ data (fig. 3.5).

The supercurrent modulation capability of each **SQUID** interferometer has been assessed by extracting the magnetic flux dependence of the critical current from the switching events in the 4-wire current-voltage characteristics. The resulting data, shown as circles in fig. 3.5, features an almost complete modulation of the switching current for all three devices. Nevertheless, minor asymmetries visible in the patterns indicate the presence of non-idealities in the interferometric response. The latter have been quantified by a least-square fit of the model represented by eqs. (3.3) to (3.5) to the experimental data. The best fit for the model is shown in fig. 3.5 as a red trace, while the corresponding parameter estimates are listed in the last three columns of table 3.1.

At a glance, all three devices appear to be characterized by similar values of the $I_o R_n$ product, with values ranging from $10 \mu V$ to $15 \mu V$. Similarly, the typical value of the relative critical current asymmetry is 5%, which corresponds to the expected nanofabrication precision in the definition of diffusive channels of given aspect ratio. Low-resistance

devices B and C are associated with higher values of normal-state conductivity, E_{TH} , and I_0 , but also with pronounced switching-retrapping hysteresis at 240 mK. The latter is only barely noticeable in the high-resistance device A, thanks to the reduction in the dissipated power in the voltage state. On the other hand, the supercurrent modulation of device A is incomplete and appreciably skewed, with an anomalously high value of the β_L parameter.

3.3 MAGNETOMETRIC PERFORMANCE

SQUIDS can be used as magnetometers in the dissipative regime: by biasing the superconducting ring with a constant current exceeding the critical current of the interferometer, changes in magnetic flux can be derived from the corresponding variations in the voltage difference developed across the Josephson junctions.

The $V(\Phi)$ characteristics of device A (the best candidate) measured at 240 mK are shown in fig. 3.6 for different values of the bias current I_b . They are periodic in flux with period Φ_0 , and have an approximate sinusoidal functional form when $I_b \gg 2I_0$. In the opposite limit, the characteristic curves show zero voltage difference for magnetic flux values such that $I_b < I_c(\Phi)$, and finite V values after switching to the dissipative regime⁸. In the switching points themselves the $V(\Phi)$ characteristics display a strongly non-linear behaviour with high values of the flux-to-voltage transfer function $|\partial V/\partial \Phi|$ which, in principle, could allow for highly sensitive magnetometry. However, the switching condition cannot be used as a stable working point since the associated dynamic range becomes null as a consequence of the stochastic nature of the switching.

The transfer function has been obtained by numerical differentiation of the $V(\Phi, I_b)$ characteristics measured in high resolution scans of the two-dimensional (Φ, I_b) space. In the resulting map, shown in fig. 3.7, several ridges are evident from the color plot, the most pronounced

⁸ Typically, for flux ranges centered around $\Phi \approx \Phi_0(n + 1/2)$, where n is an integer number.

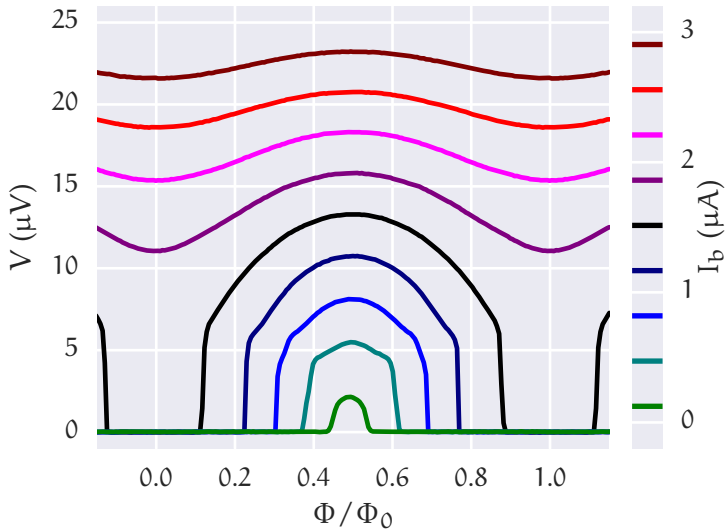


Figure 3.6: Magnetic flux dependence of the voltage across the SQUID (device A) recorded at 240 mK in a 4-wire setup. The traces are color-coded to different values of the current bias I_b .

of which corresponds to the aforementioned switching locus. As one moves down to lower values of the bias current I_b , the profile of the switching ridge broadens and eventually forks into two different ridges in which the transfer function reaches values approximately equal to $0.3 \text{ mV}/\Phi_0$. The optimal working point for maximizing sensitivity corresponds to a bias current just above the splitting point for the two ridges. In this point, indicated near the center of fig. 3.7 by a white arrow, the transfer function obtains values as high as $0.45 \text{ mV}/\Phi_0$ and is constant over an effective dynamic range of several $m\Phi_0$.

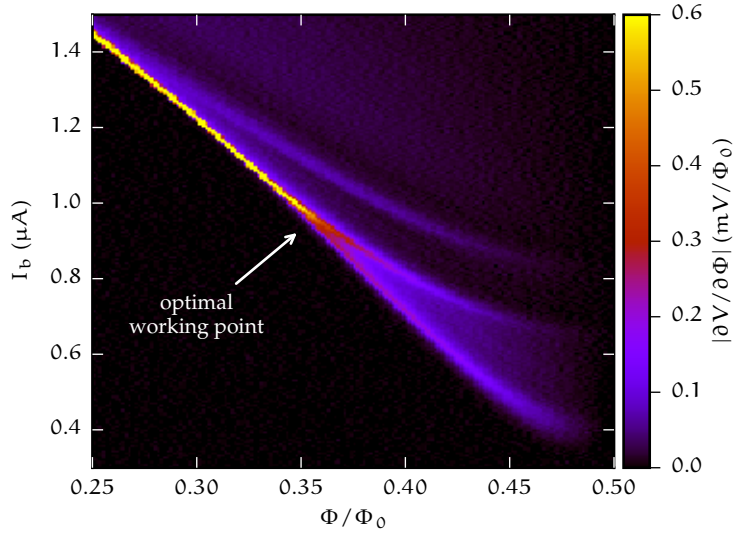


Figure 3.7: Map of the flux-to-voltage transfer function of device A obtained by numerical differentiation of $V(\Phi, I_b)$ data. The optimal working point for sensitive operation (i. e., with the transfer function showing high values approximately constant over a suitable flux interval) is indicated by a white arrow. Non-linearizable switching events (diverging $\partial V/\partial\Phi$) are represented in yellow.

The noise performance of the magnetometers has been characterized by measuring the PSD of the signal at the output of the preamplifier stage⁹. The magnetic flux resolution of the SQUID is defined as:

$$\Phi_{NS} = \frac{\sqrt{S_v}}{|\partial V/\partial\Phi|_{WP}}, \quad (3.9)$$

where S_v is the PSD of the noise (in V^2/Hz units) and $|\partial V/\partial\Phi|_{WP}$ is the absolute value of the flux-to-voltage transfer function at the selected

⁹ Battery-powered LI-75A (NF Corporation).

working point. Upon setting the SQUID to its optimal working point, the white noise level was detected to be $\sqrt{S_v} = 1.25 \text{ nV}/\sqrt{\text{Hz}}$ at 1 kHz, which is consistent with the manufacturer specifications of the input-referred noise of the preamplifier; this value corresponds to a magnetic flux resolution $\Phi_{NS} \approx 2.8 \mu\Phi_0/\sqrt{\text{Hz}}$ at 1 kHz.

To test whether the noise limit originates from the preamplification stage itself, two independent preamplifiers were connected in parallel to the SQUID output¹⁰. The autocorrelated PSD from one preamplifier and the crosscorrelated spectral density between the two preamplifiers have been extracted and compared. The corresponding magnetic flux resolution spectra are presented in fig. 3.8. The autocorrelated spectrum shows the aforementioned $2.8 \mu\Phi_0/\sqrt{\text{Hz}}$ resolution level, whereas the cross-correlated spectrum (the blue line in fig. 3.8) reaches a baseline value of $1.4 \mu\Phi_0/\sqrt{\text{Hz}}$ at 1 kHz, thus demonstrating that the magnetic flux resolution for the SQUIDs is here mostly limited by the room-temperature preamplification stage. We stress that the reported magnetic flux sensitivity levels have been measured without the aid of sophisticated electronics or advanced readout schemes, and directly follow from the intrinsic voltage response properties of SNS weak links.

On the other hand, the comparatively low level of the Thouless energy in the fabricated Josephson junctions entails a noticeable decline of their critical current values for increasing bath temperature. The temperature dependence of the maximum value of the critical current (i.e., that at $\Phi = 0$) for device A is presented in the right panel of fig. 3.9. Temperature has also been found to affect the maximum (stable) value for the transfer function. This dependence is reported in the left panel of fig. 3.9, demonstrating the possibility of operation at temperatures up to 2 K, albeit with exponentially reduced performance (suppression of approximately one decade per K).

¹⁰ See also section 2.3, page 75.

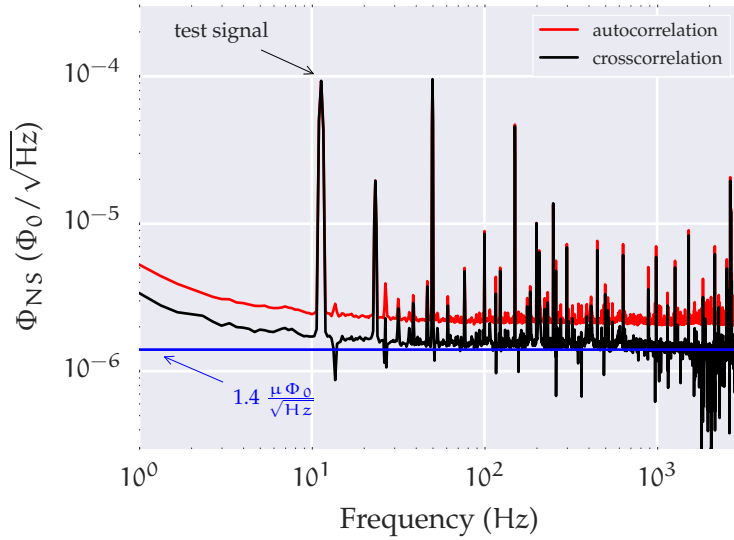


Figure 3.8: Magnetic flux resolution characterization for device A measured at 240 mK and tuned to the optimal working point for maximum sensitivity. The red and black lines represent (in magnetic flux units) the spectrum obtained, respectively, from the autocorrelation of the output of a single voltage preamplifier and from the crosscorrelation of two parallel amplification channels. A small ($100 \mu\Phi_0$ r.m.s.) applied magnetic test signal appears as a peak in both spectra at 11.7 Hz. The estimate of the white-noise equivalent background is indicated by a blue line.

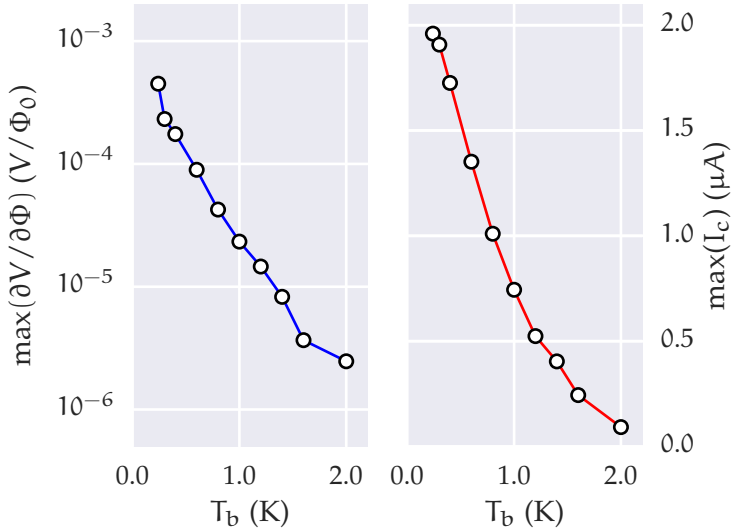


Figure 3.9: Temperature dependence of, respectively, the maximal flux-to-voltage transfer function value (left panel) and the maximum switching current (right panel) for device A. The lines are a guide to the eye.

3.4 DISCUSSION

In summary, in the present chapter we demonstrated the feasibility of using V/Cu/V SNS Josephson junctions to realize SQUID interferometers. Magnetic flux modulation of supercurrent has been observed up to 2 K. The fabricated interferometers proved unable to fully modulate the supercurrent. While not directly affecting their performance as magnetometers, this imperfection stems from both expected limitations (i. e., a minimum α_I dependent on fabrication symmetry) as well as

flux screening effects that, for device A, are rather inconsistent with the expected inductance of the interferometer ring¹¹.

A judicious design of the SNS geometry allows to limit the negative impact of switching-retrapping hysteresis of thermal origin. Our best V/Cu interferometer, equipped with standard room-temperature DC voltage preamplifiers, achieved favourable voltage responsivity figures, ultimately leading to an intrinsic magnetic flux resolution limit of $1.4 \mu\Phi_0/\sqrt{\text{Hz}}$ at 240 mK. This performance level is comparable with commercial SIS-based SQUID systems designed for 4 K operation.

For the sake of fairness, it should be remarked that the steep suppression of the transfer function figures with increasing temperature suggests that our design of V/Cu/V SQUIDs is an attractive solution mostly for bath temperature values lower than 500 mK. Still, with their non-negligible length, the investigated SNS weak links display relatively low $I_0 R_n \simeq E_{\text{Th}}$ product values. This directly reflects in the typical power dissipated during operation: for example, at the optimal working point for device A, the product $I_b V \approx 5 \text{ pW}$. In comparison, for SQUIDs devices based on SIS or Dayem bridge weak links $I_0 R_n \simeq \Delta/e$, so that the magnitude of the dissipated power tends to be significantly higher.

¹¹ The parameter estimates imply $\mathcal{L} \approx 150 \text{ pH}$ for device A, while $\mathcal{L} \approx 10 \text{ pH}$ for devices B and C.

DOUBLE-LOOP SNS MICRO-SQUID

In the previous chapter, we demonstrated the feasibility of using V/Cu/V SNS weak links as the basis for the realization of microfabricated SQUIDs. Quantitative analysis of magnetic response characteristics showed that the relative difference of critical current in two nominally-identical V/Cu/V weak links reaches values $\approx 5\%$. We attribute the origin of this effect to limitations in the reproducibility of their fabrication, both in the geometry of the normal-metal diffusive resistors and to their contact resistance with the superconducting electrodes. In retrospect, considering the nanoscale transverse dimensions of the weak links in our SQUID design, not much larger than the metallic grain size, a 5% supercurrent asymmetry level is not unexpected.

While it is the specific application that ultimately dictates the maximum tolerable critical current asymmetry, it is still generally desirable to develop and test methods to bring its effects to negligible levels. In this respect, one proven strategy is to expand the geometry of the interferometer to include an additional magnetic flux coupling loop. In such a setup, the additional control parameter allows to compensate for asymmetry in the critical current of the weak links composing the interferometer. This strategy has been proven successful in balancing SIS devices intended for metrology, quantum computation and low-temperature sensing [56].

In this chapter, we present the design and characterization of a micrometer-sized double-loop SQUID based on V/Cu/V SNS Josephson junctions. The chapter begins with a compact model introducing the details of the asymmetry compensation effect. The magnetic modulation of the critical current of the double-loop interferometer is derived from the switching events recorded by scanning the current bias of the device. This data, recorded for 22 temperature values in the 0.24 K

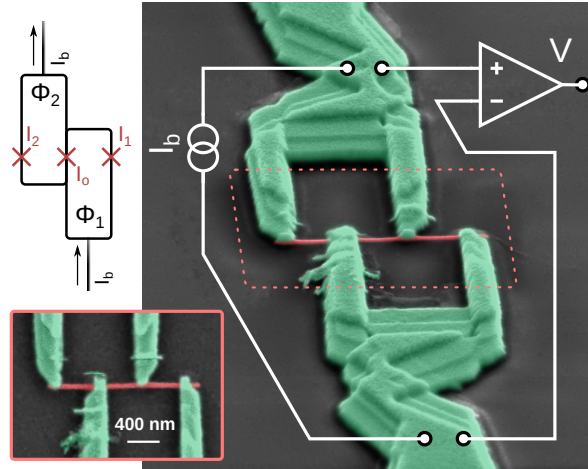


Figure 4.1: The top left panel shows a simplified supercurrent flow model in the balanced double-loop **SNS SQUID**: the bias current is labeled I_b and $\Phi_{1,2}$ represent magnetic fluxes linked to each loop; the critical current values for the three Josephson junctions are labeled $I_{0,1,2}$. The top right panel shows a tilted scanning electron micrograph of a realized device in pseudocolors. The copper layer (red) is 25 nm-thick; the vanadium (green) electrodes contacting the copper nanowire are 80 nm-thick near the nanowire and 160 nm-thick farther away on the loops as well as on the two terminals of the device. Each loop spans a surface approximately equal to $1.18 (\mu\text{m})^2$. The standard setup for a 4-wire measurement is also displayed in the superimposed scheme. The inset in the bottom left shows a perpendicular zoomed view of the **SNS** junctions. In the latter, the average interelectrode spacing is approximately 450 nm, while the nanowire is 45 nm-wide.

to 1.5 K range is fitted to the model, allowing for the extraction of the temperature-dependent critical current values of the *individual* junctions. Although in presence of relatively high junction asymmetry, we obtain supercurrent relative suppression $> 99\%$ for optimal magnetic bias at 240 mK.

4.1 TWO-PARAMETER INTERFEROMETRY

In order to describe a double-loop SQUID interferometer, we adapt the model presented in section 3.1 to the geometry summarized in the top panel of fig. 4.1. The CPR of the three junctions is assumed sinusoidal; I_k and θ_k represent the critical current and phase difference values for the three Josephson junctions, $k = 0, 1, 2$ referring to the central, left and right weak link, respectively. Without loss of generality, we normalize with respect to the central junction, so that the normalized crosswise supercurrent is:

$$i = \sin \theta_0 + r_1 \sin \theta_1 + r_2 \sin \theta_2, \quad (4.1)$$

where $r_1 = I_1/I_0$ and $r_2 = I_2/I_0$ are the normalized critical currents of the lateral junctions.

For the sake of simplicity we neglect the effect of the circulating currents on the applied magnetic field so that the flux quantization equations read:

$$\begin{cases} \theta_1 = \theta_0 + 2\pi \frac{\Phi_1}{\Phi_0} \\ \theta_2 = \theta_0 - 2\pi \frac{\Phi_2}{\Phi_0} \end{cases}, \quad (4.2)$$

where Φ_1 and Φ_2 are the magnetic fluxes linked to each loop. In analogy with eq. (3.6), combining eq. (4.1) with eq. (4.2) yields the maximum bias current that can be sustained without dissipation by the interferometer:

$$I_c(\Phi_1, \Phi_2) = I_0 \max_{\theta_0} [\sin \theta_0 + r_1 \sin (\theta_0 + 2\pi\Phi_1/\Phi_0) + r_2 \sin (\theta_0 - 2\pi\Phi_2/\Phi_0)] \quad (4.3)$$

A key point is that the critical current of the interferometer is given by the magnitude of the *vector sum* of the critical currents of the three Josephson junctions, with $2\pi\Phi_1/\Phi_0$ and $2\pi\Phi_2/\Phi_0$ playing the role of angular displacements between the current vectors representing the lateral junctions with respect to the central one. As such, one can in principle achieve perfect critical current suppression at appropriate Φ_1, Φ_2 values as long as I_0, I_1, I_2 satisfy the triangle inequality:

$$r_1 + r_2 \geq 1 \geq |r_1 - r_2|. \quad (4.4)$$

Examples of interferometers having variable degrees of asymmetry can be appreciated in the $r_1 - r_2$ representation shown in the top panel of fig. 4.2. The most symmetric case, labeled with the letter A, corresponds to an interferometer in which the three junctions have identical critical current values ($r_1 = r_2 = 1$); the corresponding $I_c(\Phi_1, \Phi_2)$ map, shown as a color plot in the bottom panel of fig. 4.2 reaches maximum values $\max(I_c) = 3 I_0$. A reduced symmetry is represented by the case in which the lateral junctions have identical critical current values, but differ from the central junction (*e.g.*, $r_1 = r_2 = 0.5$, labeled as C). Finally, the generic asymmetric case is represented by $r_1 = 0.6, r_2 = 0.9$, values which have been found to approximate the behaviour of the presented device at temperature $T = 0.24\text{K}$; this case is labeled with the letter B in fig. 4.2. All three cases fulfill eq. (4.4), thus they show complete supercurrent suppression for appropriate Φ_1, Φ_2 coordinates; the latter can be located with the aid of white lines in the bottom panel of fig. 4.2.

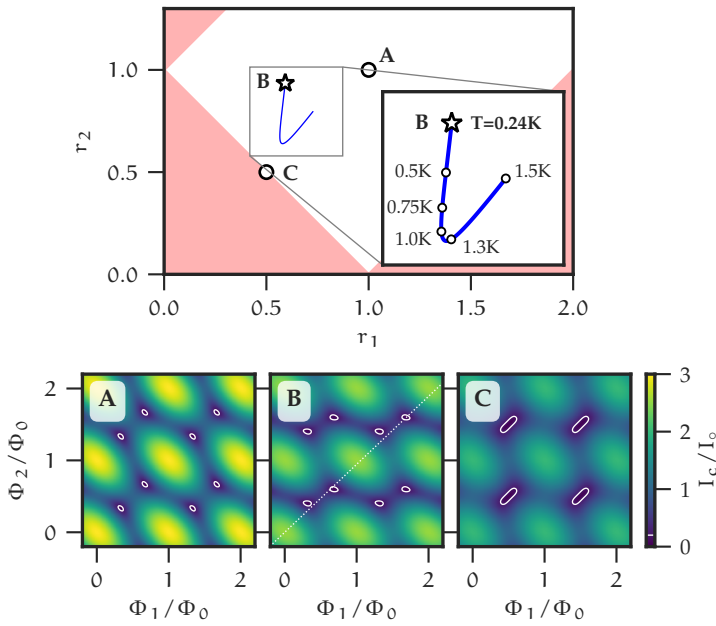


Figure 4.2: The top panel shows the configuration diagram for possible realizations of the double-loop interferometer; parameters $r_1 = I_1/I_0$ and $r_2 = I_2/I_0$ define the amount of asymmetry in critical current between the lateral and the central junctions; a fully symmetric interferometer is obtained with $r_1 = r_2 = 1$ (A), a partially symmetric interferometer is obtained with $r_1 = r_2 \neq 1$ (C). The device presented (B) shows an asymmetric configuration at 0.24 K, where $r_1 \neq r_2 \neq 1$. The area shaded in red represents interferometers which are un-balanceable due to excessive asymmetry; the inset shows the temperature-dependent behaviour of the fabricated device. The bottom panel displays colormap plots of the critical current for the three points labeled in the top panel as a function of magnetic fluxes linked to each loop (Φ_1, Φ_2); local minima are encircled by the white $I_c/I_0 = 0.2$ isoline as a visualization aid; the dotted white line in the colormap to B highlights the flux pair values that can be set by applying an external homogeneous magnetic field to the slightly asymmetric loops of the presented device.

4.2 EXPERIMENTAL CHARACTERIZATION

The main panel in fig. 4.1 shows a scanning electron micrograph of the realized double-loop interferometer. The latter is fabricated according to the protocols detailed in section 2.1 with the deposition of four metallic layers. Initially, a 5 nm-thick adhesivant aluminium layer followed by a 25 nm-thick copper film were deposited at normal incidence to obtain the normal-metal parts; the superconducting body of the interferometer was then realized by depositing two 80 nm-thick vanadium films at opposing angles ($\pm 17^\circ$).

The fabricated interferometer features three weak links (as shown in the zoomed-in view in the bottom left of fig. 4.1) consisting of a diffusive normal-metal wire having width and thickness of 45 nm and 25 nm, respectively; the inter-electrode spacing between vanadium leads is approximately equal to 450 nm. Since the transverse extent of the copper wire is less than the superconducting coherence length ξ_D at each vanadium electrode, the local electronic density of states in the normal metal is expected to have a minigap close to the superconducting energy gap in the electrode itself¹, so that the system can be pictured as having three independent weak links.

The electron transport properties of the interferometer have been characterized in the *Heliox* setup, for 22 bath temperature values in the 0.24 K to 1.5 K range. Current-vs-voltage curves have been estimated with a lock-in amplifier under square-wave modulation² of the current bias I_b . The voltage response of the interferometer has been characterized as a function of magnetic field applied orthogonally to the substrate of the sample.

Figure 4.3 shows the characterization of the interferometer at base temperature ($T \approx 240$ mK); the typical input-referred voltage noise for this setup has been measured to be < 10 nV_{rms}. In this setup, magnetic flux biasing is provided by magnetic field applied homogeneously over the extent of the device, so that the flux coordinates Φ_1 and Φ_2

¹ This has been shown in detail in section 1.7, page 51 and following.

² See section 2.3.

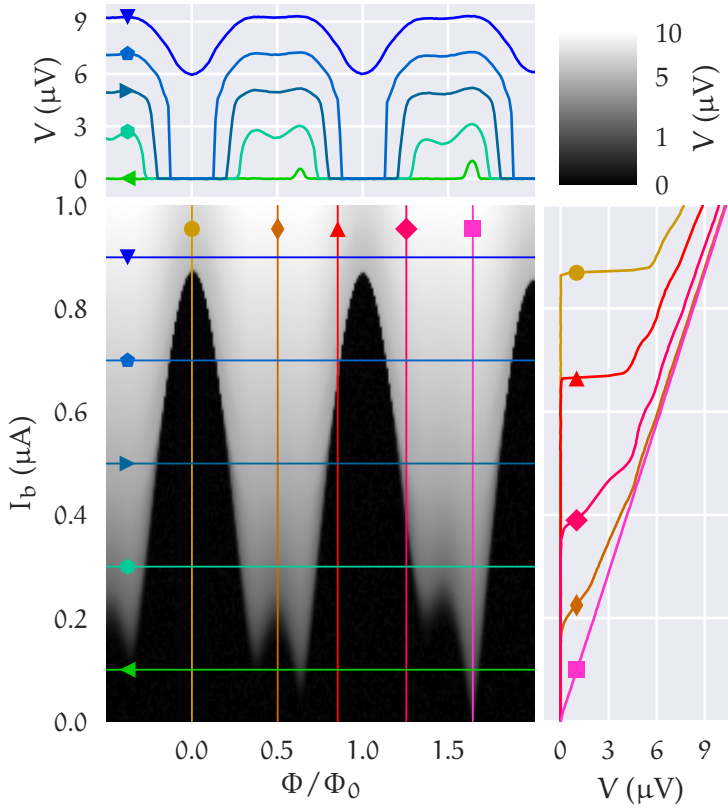


Figure 4.3: The bottom left panel shows a greyscale map of the voltage response V recorded at 240 mK as a function of both the biasing current I_b and the loop-average applied magnetic flux Φ . The grey level is proportional to \sqrt{V} (top right corner) in order to enhance the visual contrast of the switching events. The top panel shows flux-to-voltage characteristic curves extracted from $V(I_b, \Phi)$ data for fixed values of the bias current ($I_b = 0.1, 0.3, 0.5, 0.7, 0.9 \mu\text{A}$, marked as horizontal lines in the map). The right panel shows current-to-voltage characteristic curves extracted from $V(I_b, \Phi)$ data for fixed values of the applied magnetic flux ($\Phi = 0.0, 0.50, 0.86, 1.26, 1.66 \Phi_0$, marked as vertical lines in the map).

are proportional to the applied field and can in principle differ as a consequence of effective loop surface asymmetry:

$$\Phi_{1,2} = (1 \pm \alpha) A_{\text{eff}} B = (1 \pm \alpha) \Phi, \quad (4.5)$$

where A_{eff} is the average effective surface, and α is the effective loop surface asymmetry coefficient.

In fig. 4.3, the magnetic field dependence is shown in terms of the loop-average magnetic flux $\Phi = (\Phi_1 + \Phi_2)/2$. The device shows remarkably ohmic voltage response for applied flux $\Phi = 1.66 \Phi_0$, the characteristic marked with a pink square in the bottom right panel of fig. 4.3, corresponding to a measured resistance $R_n \approx 10.3 \Omega$. Additionally, not exactly periodic modulation can be appreciated from the voltage-vs-flux characteristics shown in the top panel of fig. 4.3, confirming a slight asymmetry in the effective areas of the two superconducting loops.

4.3 MODEL FITTING

A quantitative assessment of the transport properties of the interferometer has been performed by extracting the $I_c(\Phi)$ values by fitting differential resistance data with a sigmoid test function. This *a posteriori* approach provides us with switching current data (shown for selected temperature values in the left panels of fig. 4.4) which are associated with an uncertainty derived from the quadrature propagation of the intrinsic sigmoid width and the current bias discretization error. For lower temperature values, the switching is sharp and the relative uncertainty of the extraction process is limited by the latter term ($\approx 6 \text{ nA}$ over a $1 \mu\text{A}$ scan); with increasing temperature the “intrinsic” sigmoid width gradually takes over, reaching typical values of tens of nA at $T = 1.5 \text{ K}$.

The extracted $I_c(\Phi, T)$ data have been fitted (bottom left panel of fig. 4.4) using eqs. (4.3) and (4.5) as a model, yielding the estimate for the loop surface asymmetry coefficient $\alpha = 0.028 \pm 0.003$. A direct

JUNCTION	ξ	E_{Th} (μeV)	T_c^* (K)
I_o	0.211 ± 0.002	15.1 ± 0.2	1.61 ± 0.01
I_1	0.132 ± 0.003	13.7 ± 0.4	1.66 ± 0.03
I_2	0.256 ± 0.004	10.2 ± 0.2	1.68 ± 0.03

Table 4.1: Parameter estimates for the ideality coefficient ξ , Thouless energy E_{Th} and effective critical temperature at the electrodes T_c^* of the three junctions of the interferometer obtained by fitting eq. (4.6) to $I_k(T)$ data (bottom right panel of fig. 4.4).

comparison between data points and model demonstrates the effectiveness of the latter in describing our mesoscopic SNS interferometer, particularly impressive considering the minimal amount of underlying hypotheses. The fitting procedure provides a means of extracting the temperature dependence of the critical current of *each* of the three constituent Josephson junctions; this derived dataset is shown in the bottom right panel of fig. 4.4.

The three junctions show markedly different $I_k(T)$, both in terms of the characteristic temperature scale of the supercurrent suppression (dependent on the Thouless energy) and of the magnitude of the supercurrent (affected both by the Thouless energy and the normal-state resistance of the SNS weak links). The analytical model of eq. (1.63), whose validity in the high temperature regime has been specifically verified for V/Cu/V junctions, can be slightly adapted to the form:

$$I_c(T) = \xi \frac{64\pi k_B T}{e\mathcal{R}} \sum_{n=0}^{+\infty} \frac{\sqrt{\frac{2\omega_n}{E_{\text{Th}}}} \Delta^2 \exp\left(-\sqrt{\frac{2\omega_n}{E_{\text{Th}}}}\right)}{\left[\omega_n + \Omega_n + \sqrt{2(\Omega_n^2 + \Omega_n \omega_n)}\right]^2}, \quad (4.6)$$

where $\mathcal{R} = 3R_n \approx 30.8 \Omega$ is the average normal-state resistance of a single junction as extracted from current-vs-voltage measurements and ξ accounts for non-ideality of the normal-superconductor interface. We

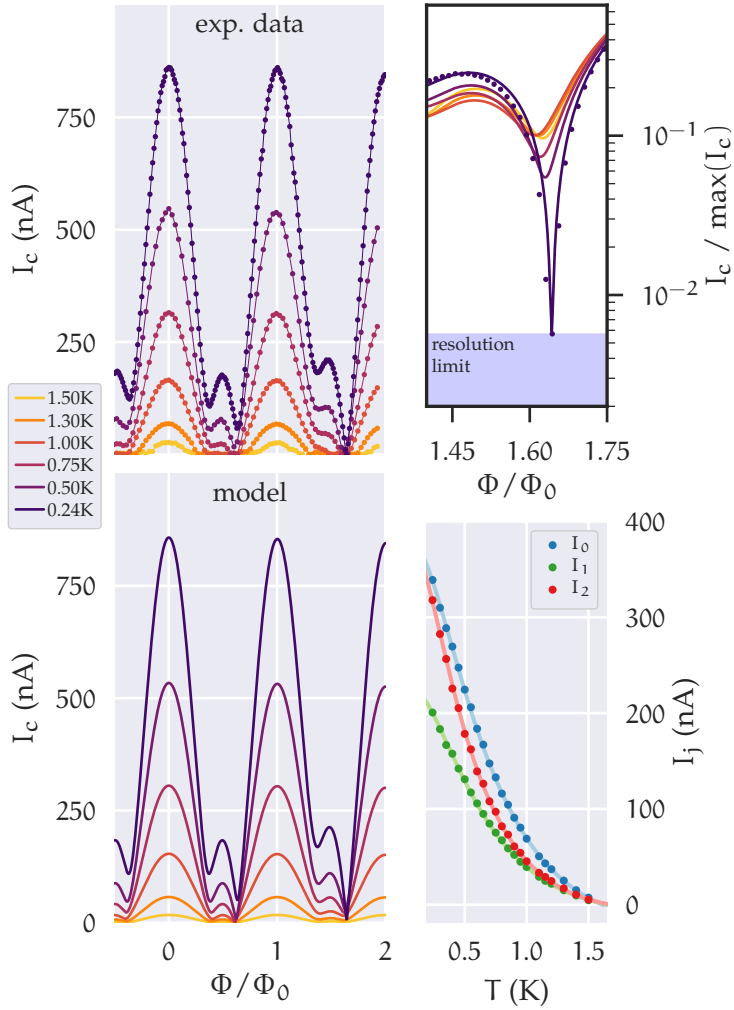


Figure 4.4: See following page for the caption.

Figure 4.4: The top left panel shows experimental critical current values for the interferometer as a function of magnetic flux at different temperatures (color coded). The critical current points have been extracted from $V(I_b, \Phi)$ fixed-temperature datasets, an instance of which has been presented in fig. 4.3; continuous lines joining data points have been added as a visual aid. The bottom left panel shows the proposed model fitted to data presented in the top left panel. The top right panel shows the supercurrent suppression ratio achieved at $\Phi/\Phi_0 = 1.66$ for different values of temperature. Colored continuous lines are derived from the optimal model presented in the bottom left panel; data points calculated for the $T = 0.24$ K dataset are also displayed, along with a shaded area representing the resolution limit due to discretization in current scanning. The bottom right panel shows the temperature dependence of the critical current for each Josephson junction. The continuous lines represent the fitted model for the critical current of long diffusive Josephson junctions in the high-temperature regime.

assume $\Delta(T)$ dependence to be BCS-like (parametrically determined by specifying an effective critical temperature T_c^* for the vanadium electrodes). This model has been used to fit $I_k(T)$ data for each junction, obtaining the parameter estimates reported in table 4.1.

4.4 DISCUSSION

Even though the interferometer has been designed to be fully symmetric, the quantitative modeling procedure shows that deviations from ideality inherent to the fabrication process resulted in junctions with significantly different $I_k(T)$, stemming from different E_{Th} and ξ values. The presence of measurably different Thouless energy scales introduces a temperature dependence in the $r_1 - r_2$ parameters for the presented device, as it can be appreciated in the inset of the top panel of fig. 4.2. Nevertheless, under optimal flux biasing we were able to measure rel-

ative supercurrent suppression $> 99\%$ at base temperature (top right panel in fig. 4.4).

Although such observation was possible in homogeneous magnetic field only thanks to the fortuitous match between loop asymmetry and junction asymmetry, the fitness of the double-loop geometry as a means to circumvent junction asymmetry in mesoscopic SNS-based devices is still confirmed in a general sense. In fact, it is worth noting that the additional degree of freedom granted by the second loop in the geometry entails the possibility of having the interferometer respond both to the homogeneous part and to the first spatial derivative of the magnetic field (proportional to the sum and difference of Φ_1 and Φ_2 , respectively) on a micrometric length scale; moreover, the relative strength of response can be tuned by designing the interferometer with optimal $r_1 - r_2$ parameter values³, easily allowed by the flexibility of the shadow-mask lithographic technique.

³ For example, robust gradiometric response is evident in the asymmetric interferometer labeled as C in fig. 4.2.

ALUMINUM/COPPER SQUIPT

So far we have considered superconducting interferometer designs where the phase bias of multiple SNS weak links induces the modulation of the *crosswise* supercurrent through the interferometer, allowing for a simple DC voltage readout under constant current bias. This configuration is functionally equivalent to devices based on SIS weak links, owing to the universality of the Josephson effect. On the other hand, the SNS fingerprint is expected mostly in terms of a broader signal bandwidth¹ and with respect to the marked temperature dependence of the critical current. The latter is a limiting factor in practical devices², but it is also at the heart of the quantitative characterization of the individual component weak links of the double-loop interferometer presented in the previous chapter.

Both in this and the following chapter, we consider an interferometer where proximity effect plays an even more central role: the Superconducting QUantum Interference Proximity Transistor (SQUIPT) [57]. Its basic design consists in a *single* diffusive nanoscopic metallic weak link embedded in a micrometer-sized superconducting loop. The readout mechanism is provided by a probe electrode in contact with the diffusive weak link through a tunnel junction; the quasiparticle current through the latter is in fact dependent on the LDOS spatially sampled by the tunnel electrode, which in turn is a function of the phase bias acting on the weak link itself. The external magnetic field threading the loop fixes the phase difference across the weak link as a consequence of flux quantization in the closed superconducting ring³; notably, different

- ¹ Consequence of the negligible intrinsic RC cutoff for this type of weak link.
- ² This is evident in the exponential suppression with increasing temperature of the magnetometric responsivity of the V/Cu SQUID, as shown in the left panel of fig. 3.9.
- ³ Chapter 1 presents a thorough review of the fundamental phenomena involved; see in particular sections 1.4, 1.6 and 1.7.

from a [SQUID](#), the phase difference across the weak link can reach values up to π .

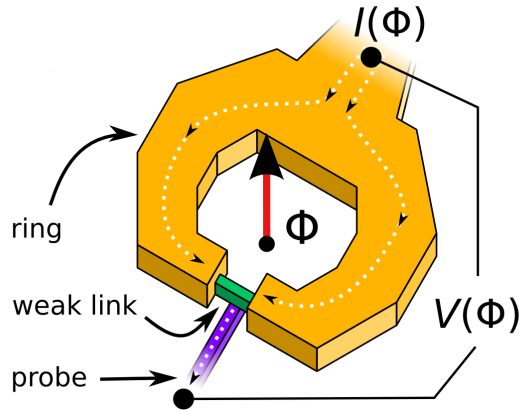


Figure 5.1: Functional schematic of a [SQUIPT](#) device. In the schematic Φ is the magnetic flux linked to the superconducting loop, $I(\Phi)$ and $V(\Phi)$ are respectively the current flowing through and the voltage difference across the device.

At a fundamental level, the current-voltage [DC](#) response of a [SQUIPT](#) device provides spectroscopic information on the correlated phase-biased electronic condensate. As a magnetometer, the [SQUIPT](#) is attractive because of its fundamentally simple interferometer geometry, where, e. g., weak link asymmetry cannot occur. At the same time, the information on the weak link's phase is conveniently carried by [DC](#) signals developed across the probe electrode, with characteristic impedance (given by typical tunnel resistance in the 10 k Ω to 1000 k Ω range) that is perfectly suited to audio-band [LNAs](#).

This chapter details the fabrication and characterization of [SQUIPT](#) devices based on Al/Cu [SNS](#) weak links and intended for robust magnetometric performance. The chapter begins with a historical review of the evolution of the [SQUIPT](#) geometry, along with a discussion of their

characteristic operative issues, followed by a description of our design approach. Next, we present experimental data showing proof of full phase-induced minigap modulation in the proximized copper weak link. The magnetometric performance figures are then assessed comparing the magnetic responsivity with the signal noise recorded from the full amplification chain. The chapter is concluded by a discussion on the significance of the results obtained.

5.1 OPTIMAL SQUIPT DESIGN

The earliest proof-of-concept realization [57] of a SQUIPT describes a device based on a $1.5\ \mu\text{m}$ -long copper weak link, proximized by a thin aluminum loop spanning a surface of approximately $120\ (\mu\text{m})^2$. These figures result in the SNS junction being in the *long* diffusive limit, entailing modest amplitude of the minigap at zero applied field (approximately equal to $10\ \mu\text{eV}$, limited by the small value of the Thouless energy). In subsequent attempts aimed at increasing the response of the device up to its predicted intrinsic limits [58], the length of the normal-metal wire has been reduced to bring the SNS junction in the *short* regime, where the amplitude of the proximized minigap can approach that of the “parent” superconductor. These devices [59] succeed in achieving sizeable induced minigap width ($\approx 130\ \mu\text{eV}$) but suffer from hysteresis stemming from self-induced magnetic screening caused by the high critical current magnitude typical of such low-resistance metallic weak links. In a subsequent work [60], this shortcoming was lifted by reducing the cross section of the copper wire increasing its resistance while keeping it in the short-junction limit. With this approach, a $50\ \mu\text{eV}$ minigap modulation amplitude was observed, a value corresponding to only $\approx 36\%$ of the full induced minigap width measured at zero applied magnetic field.

The typical cause for incomplete minigap modulation lies in non-ideal phase bias of the weak link. In the limit of negligible magnetic screening originating from the geometric self-inductance of the loop, the effective phase difference imposed to the weak link by flux quantization

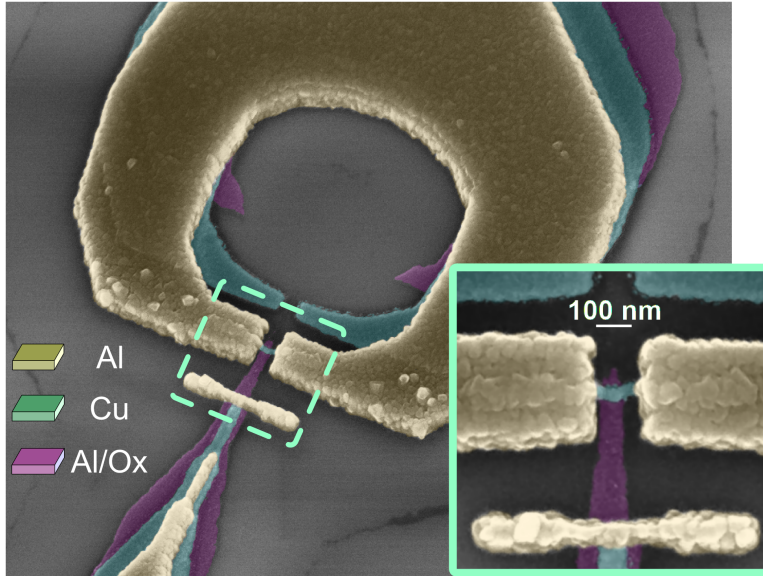


Figure 5.2: Pseudo-colour scanning electron micrographs of a typical SNS SQUIPT device, realized by tilted evaporation of metallic thin films through a suspended resist mask defined by electron-beam lithography. The first evaporation (purple layer) consists in 15 nm of aluminum (Al), subsequently oxidized to form an AlOx tunnel barrier. The second evaporation (green layer) consists in 25 nm of copper (Cu) realizing the normal metal nanowire. Finally, 150 nm of Al (dark yellow) are evaporated to form the superconducting loop (having inner diameter $\simeq 1.7 \mu\text{m}$) as well as the electrodes in clean electric contact with the Cu film. The inset in the bottom right shows a magnified view of the Cu nanowire region. The interelectrode spacing is $\simeq 140 \text{ nm}$; the width of the nanowire is $\simeq 30 \text{ nm}$. The tunnel probe is $\simeq 60 \text{ nm}$ -wide at the interface with the Cu weak link.

is affected by the competition between the kinetic inductance of the superconducting loop and the Josephson inductance of the weak link (respectively \mathcal{L}^S and \mathcal{L}^{WL}). Complete phase bias, corresponding to high phase gradient developed across the Cu nanowire, is only possible in the limit $\mathcal{L}^S/\mathcal{L}^{WL} \ll 1$ [61]. The difficulty in achieving this regime originates from the short-junction nature of the weak links which, apart from the aforementioned high critical current values, also show at low temperature a non-sinusoidal CPR $I^{WL}(\theta)$. Both effects [15, 16] suppress the magnitude of $\mathcal{L}^{WL} = (\Phi_0/2\pi)(\partial I^{WL}/\partial\theta)^{-1}$ as the value of the phase difference θ approaches π , where the sharpest response is expected [58].

Here we show that a complete phase bias can be achieved in a junction approaching the short limit by realizing a copper wire having a nanoscale cross-section (thus maximizing \mathcal{L}^{WL}) while at the same time having a compact superconducting aluminum loop characterized by low normal-state resistance (therefore minimizing both the kinetic and geometric components of \mathcal{L}^S). As a consequence of the full minigap modulation in the proximized weak link, we obtain record magnetic flux responsivity figures, both in current- and voltage-biased setups.

5.2 TRANSPORT SPECTROSCOPY

Figure 5.2 shows a scanning electron micrograph of a typical SQUIPT device, fabricated according to the protocols detailed in section 2.1 with the deposition of three metallic layers. An initial 15 nm-thick Al layer is deposited at 40° and subsequently exposed to a pure O_2 atmosphere (37 mTorr for 300 s) to obtain the tunnel probe electrode. The normal-metal nanowire is realized by evaporating a 25 nm-thick Cu layer at 20° . Finally, a 150 nm-thick Al film in clean contact with the latter layer is deposited at zero angle to implement the superconducting loop, designed to have an internal diameter $\simeq 1.7 \mu\text{m}$.

The device core (visible in the bottom right inset of fig. 5.2) is characterized by an interelectrode spacing $L \simeq 140 \text{ nm}$, while the copper nanowire is 30 nm-wide and overlaps the lateral supercon-

ducting electrodes for $\simeq 400$ nm per side. The width of the tunnel probe electrode is $\simeq 60$ nm. Based on previous measurement on Cu nanowires of similar cross-section in the previous chapter, we estimate the ratio $L/\xi_0 = L\sqrt{\Delta_r/\hbar D_{Cu}} \approx 1.1$ which confirms the frame of the intermediate-short junction regime. Above, $\Delta_r \simeq 185$ μeV is the energy gap in the superconducting ring and $D_{Cu} \simeq 55$ $\text{cm}^2 \text{s}^{-1}$ is the diffusion coefficient for our Cu nanowire. The yield of such simple fabrication scheme is about 20%, being mostly limited by the mechanical stability of the suspended polymethyl-methacrylate mask defining the loop.

The magneto-electric characterization was performed in the *Heliox* setup. Current response under voltage bias was measured in a two-wire configuration as a function of the magnetic flux generated by a magnetic field applied orthogonally to the plane of the substrate. The current response shows periodicity with respect to the applied magnetic field density with period $B_0 = \Phi_0/A_{\text{eff}} \approx 6.2$ G, where $A_{\text{eff}} \approx 3.3$ (μm)² is consistent with the area enclosed by the ring of the SQUIPT.

The left panel of fig. 5.3 shows the current-vs-voltage $I(V_b)$ characteristics recorded at the base temperature ($T = 240$ mK), for selected equally-spaced values of the applied magnetic flux ranging from $\Phi = 0$ to $\Phi = \Phi_0/2$. At zero flux (fully open minigap) the characteristic shows a behaviour resembling that of a tunnel junction between superconductors with different energy gaps. By increasing the magnetic field the minigap closes, until the characteristic is similar to that of a NIS junction at $\Phi = \Phi_0/2$. From these data we estimate the 15 nm-thick aluminum probe to be characterized by a superconducting gap $\Delta_{\text{pr}} \approx 235$ μeV and a tunnel resistance $R_T \approx 55$ k Ω . The curves are consistent with a maximum minigap amplitude $\varepsilon_g(\Phi = 0) \approx 145$ μeV , a value which corresponds approximately to 78% of Δ_r , the energy gap in the superconducting ring. The top right panel of fig. 5.3 shows the theoretical BCS-like profile [14] of the DOS in the probe junction where a Dynes parameter $\gamma/\Delta_{\text{pr}} = 10^{-3}$ accounts for energy smearing due to finite quasiparticle lifetime [25, 26]. The bottom right panels in fig. 5.3 show the theoretical DOS in the weak link $\bar{\rho}_{\text{WL}}(E)$, spatially averaged over the probe width. The latter DOS has been obtained by solving numer-

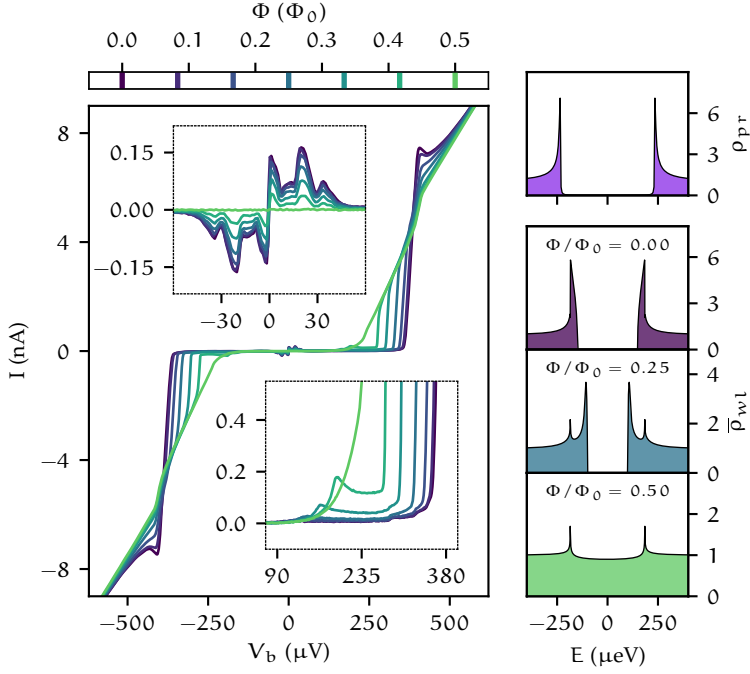


Figure 5.3: The left panel shows current vs voltage characteristics recorded at 240 mK for 7 equally-spaced magnetic flux values ranging from $\Phi = 0$ to $\Phi = \Phi_0/2$. The upper inset shows a magnification of the low-voltage bias range, where weak phase-dependent supercurrent features appear at fixed voltage values. The lower inset shows a magnification of the onset of quasiparticle conduction, where the voltage dependence of the current can be non-monotonic as a consequence of thermally-activated transport. This is particularly evident (at finite temperature) when the minigap starts to be suppressed by the magnetic flux. The top right panel shows the theoretical BCS density of states $\rho_{pr}(E)$ of the superconducting probe ($\Delta_{pr} = 235 \mu\text{eV}$). The bottom right panels show the theoretical local density of states $\bar{\rho}_{wl}(E)$ in the proximized weak-link averaged over the probe width for three different values of the applied magnetic flux. $\bar{\rho}_{wl}(E)$ was obtained by the numerical solution of the 1-D Usadel equations assuming $L = 1.1 \xi_0$, and full transparency at the interfaces.

ically the 1-D Usadel equations according to the methods presented in chapter 1 with parameters $L/\xi_0 = 1.1$, $\Delta_r = 185 \mu\text{eV}$ and assuming perfect interface transparency between the ring and the wire, for $\Phi = 0, 0.25, 0.5 \Phi_0$.

The upper inset in the left panel of fig. 5.3 shows a magnified view of the flux dependent features appearing at low bias. The latter can be attributed to a weak Josephson coupling between the proximized nanowire and the probe electrode, and their complete suppression at $\Phi = \Phi_0/2$ is a further indication of the full modulation of the minigap. A close inspection of the current-vs-voltage characteristics in fig. 5.3 indicates that the measured current modulation is able to reach peak-to-peak amplitudes as large as 4 nA. On the other hand, when biased at fixed current, the amplitude of the corresponding voltage modulation approaches ε_g/e .

The lower inset in the left panel of fig. 5.3 shows a magnified view of the characteristics at the onset of quasiparticle conduction. Here the current is non-monotonic as a consequence of the appreciable thermal population of the quasiparticle states in the proximized nanowire resulting in additional conduction when $V_b = [\Delta_{pr} - \varepsilon_g(\Phi)]/e$. This bias configuration shifts the chemical potentials of the tunnel junction electrodes so that the singularity in the DOS of the probe electrode is energetically aligned to the thermally excited quasiparticles in the copper nanowire. In the following, we adopt the term “singularity-matching peak” to refer to this particular transport feature, in analogy to S_1IS_2 systems [12]. The tunnel resistance value obtained in the fabrication process is compatible with the optimal input load impedance of both voltage and current preamplifiers. In the following we consider both voltage-biased and current-biased setups.

5.3 MAGNETOMETRIC PERFORMANCE

Current-vs-flux (*i.e.*, at fixed voltage bias) response figures have been obtained by numerical differentiation with respect to the magnetic flux of the $I(\Phi, V_b)$ characteristics (top left panel of fig. 5.4) at fixed V_b .

The bottom panel shows the absolute value of the base temperature flux-to-current transfer function $|\partial I(V_b, \Phi)/\partial \Phi|$ as a colormap. In this context the transfer function map indicates sharp response (due to the abrupt onset of quasiparticle conduction) reaching values as high as $108 \text{ nA}/\Phi_0$, over a wide range of the bias parameters in both flux: $\Phi \in [0.35 \div 0.45 \Phi_0]$, and voltage bias: $V_b \in [275 \div 310 \mu\text{V}]$. This high sensitivity (approximately four times higher than the best-performing devices so far [60]) originates from both a lower tunnel probe resistance and a full modulation of the minigap. In addition, the maximum flux-to-current responsivity level, is only moderately suppressed by increasing the temperature (top right panel in fig. 5.4).

Voltage-vs-flux characteristics, recorded at 240 mK for a few selected values of the current bias in the vicinity of the maximal response ($I_b = 435 \text{ pA}$, $\Phi \simeq 0.5 \Phi_0$) are shown in the left panel of fig. 5.5. The absolute value of the relative flux-to-voltage transfer function is plotted as a colormap in the left panel of fig. 5.6. At low current bias the non-monotonicity of the current vs voltage characteristics (see the bottom inset in fig. 5.3) results into bistable voltage configurations, giving rise to hysteretic behaviour and limiting the useful bias range for a SQUIPT used as a linear sensor. The non-monotonicity originating from the singularity-matching peak can, in principle, be limited by lowering the electron temperature beyond the base temperature of our cryostat. This can be achieved by using dilution refrigerators but also with the adoption of integrated on-chip electronic coolers [24, 62] relying on the same fabrication technique. On the other hand, the supercurrent peaks (see top inset in fig. 5.3) give rise to a similar electric bistability and are expected to increase in magnitude at lower temperatures (when not countered by lower transparency of the tunnel barrier) and will ultimately limit the current bias range available for linear response.

Notably, the electric bistability provided by the singularity-matching peak could instead be exploited for operating the SQUIPT as a threshold detector. In this configuration, the flux is applied in the close vicinity of a switching point (*e.g.*, $I_b = 335 \text{ pA}$ and $\Phi = 0.48 \Phi_0$ in the left panel of fig. 5.6), so that flux variations crossing the threshold given by the

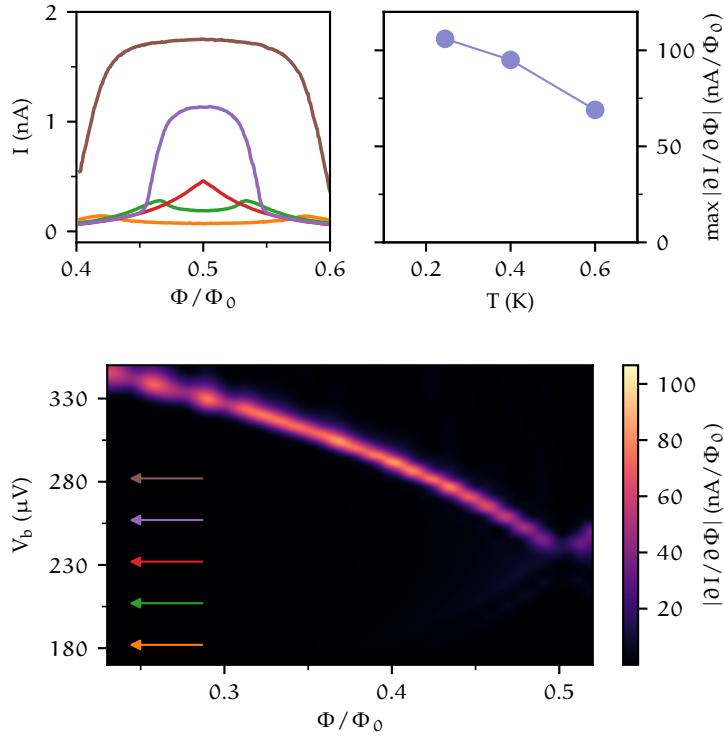


Figure 5.4: The top right panel shows current-vs-flux characteristics measured at 240 mK for fixed voltage bias (from bottom to top, $V_b = 182, 212, 232, 252$ and $282 \mu\text{V}$). The bottom panel shows a colormap of the absolute value of the flux-to-current transfer function ($|\partial I / \partial \Phi|$ vs V_b and Φ) obtained by numerical differentiation of the $I(\Phi)$ curves measured at 240 mK. Arrows indicate in corresponding colors the voltage bias values for the characteristics plotted in the top left panel. The top right panel shows the temperature dependence of the maximum absolute value of the flux-to-current transfer function.

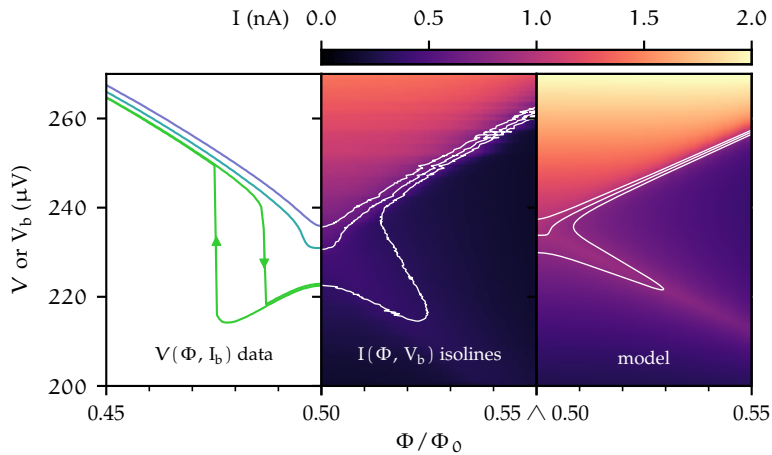


Figure 5.5: The left panel shows voltage-vs-flux characteristics measured at 240 mK for fixed current bias (from bottom to top, $I_b = 335, 435$ and 535 pA). The middle panel shows a colormap showing the measured $I(V_b, \Phi)$ dataset; the current isolines match the characteristics shown in the left panel. The reentrant shape of the lowest current isoline is at the origin of the hysteresis displayed in the corresponding $V(\Phi, I_b)$ characteristic (green trace in the left panel). The right panel shows a colormap of the theoretical current vs V_b and Φ calculated for a [SQUIPT](#) device based on a [SNS](#) weak link in the short regime.

switching point yield a voltage step response (whose amplitude may be $\approx 50 \mu\text{V}$) within a timescale corresponding to the relaxation time of the measurement setup. Such scheme can be useful for sampling the probability distribution function of a noisy magnetic flux source.

We now discuss the SQUIPT sensitivity when operated as a linear flux sensor. Inspection of the flux-to-voltage transfer function (shown as a colormap in fig. 5.6) reveals that the current-biased setup allows for a high responsivity ($\approx 1 \text{ mV}/\Phi_0$) over a rather broad flux and current bias range, with a peak value of $\approx 3 \text{ mV}/\Phi_0$, located at $\Phi = 0.495 \Phi_0$ and $I_b = 435 \text{ pA}$. This working point lies just outside of the hysteretic region, marked with magenta lines, and it is thus a suitable point for linear operation of the detector.

While compatible with earlier results [60], such a high voltage transfer function may seem surprising. Indeed, the detailed theoretical investigation of the SQUIPT performance in the short junction limit (where analytic calculations can be performed) carried in [58], predicted maximal transfer functions of about $3.1\Delta_r/e\Phi_0$ around $\Phi = 0.5 \Phi_0$, which can be traced back to the flux dependence of the minigap. Extrapolating this limit to our moderately-short SNS junction, *i.e.*, assuming the same scaling but replacing Δ_r with the measured minigap $\varepsilon_g = 145 \mu\text{eV}$, one would expect a response of about $450 \mu\text{V}/\Phi_0$, which is approximately 6 times smaller than the maximum value obtained in the experiment.

The reason for the observed higher response originates from the contribution of the singularity-matching peak, ignored in [58], which bends the non-hysteretic $V(\Phi, I_b)$ characteristics in the vicinity of $\Phi_0/2$ and $V = \Delta_{pr}/e$, resulting in a sharper voltage response. This feature can be easily reproduced by using a simplified model which holds in the short-junction limit as described in [58], with the replacement $\Delta_r \leftrightarrow \varepsilon_g$.

The right panel in fig. 5.5 presents a contour plot of the $I(\Phi, V_b)$ dataset obtained with the above theoretical model in the vicinity of $eV_b = \Delta_{pr} = 235 \mu\text{eV}$ and $\Phi/\Phi_0 = 0.5$ at $T = 240 \text{ mK}$. The white lines correspond to calculated current isolines, who strongly resemble those observed in the actual measured $I(\Phi, V_b)$ characteristics (see the

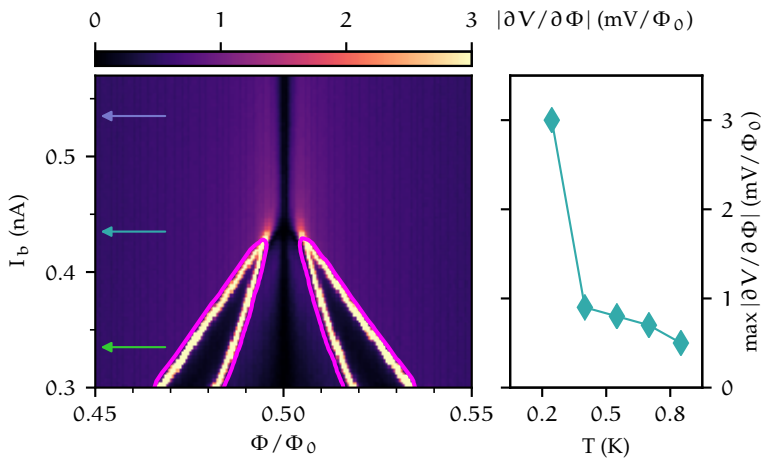


Figure 5.6: The left panel shows a colormap of the absolute flux-to-voltage transfer function ($|\partial V / \partial \Phi|$ vs I_b and Φ) obtained by numerical differentiation of $V(\Phi)$ curves measured at 240 mK. Hysteresis originating from the non-monotonicity of the current vs voltage characteristics (see lower inset of fig. 5.3) can be appreciated for $I_b < 435 \text{ pA}$. Magenta lines mark the hysteretic regions in the colormap. Arrows indicate in corresponding colors the current bias values for the characteristics plotted in the left panel of fig. 5.5. The right panel shows the temperature dependence of the maximum absolute value of the flux-to-voltage transfer function.

middle panel of fig. 5.5). Although rather idealized, the model provides a satisfactory reproduction of the physical mechanism underlying the observed high responsivity. Furthermore, a close match between the measured $V(\Phi, I_b)$ response curves and the current isolines can be appreciated in the juxtaposition of leftmost panels in fig. 5.5, therefore corroborating the identification of physical origin of the high flux-to-voltage responsivity we observe.

In particular, three regimes can be recognized, depending on the magnitude of the quasiparticle current. Low-current regime (corresponding to the green trace) is characterized by hysteresis originating from the singularity-matching peak bistability, which is evident in the reentrant shape of the low-current isolines in the rightmost panels of fig. 5.5. Conversely, in the high-current limit (exemplified by the blue trace) no hysteresis can be found, but the magnetic flux responsivity is only moderate. The optimal regime for sensitivity (represented by the cyan trace) emerges in the smooth transition between the two abovementioned limits. This latter regime features the highest value of the flux-to-voltage transfer function, but no hysteresis.

The temperature dependence of the maximum value of the transfer function is displayed in the right panel of fig. 5.6. The substantial enhancement observed at lower temperature is due to the abrupt character of the thermal suppression of the singularity-matching peak appearing in the current-vs-voltage characteristics, which allows to access the optimal current-bias range required for the sharpest voltage response.

Our device has been designed to show that high transfer function values can be obtained in SQUIPTs based on Al-Cu technology. The intermediate value of the impedance of the device ($R_T = 55 \text{ k}\Omega$), allows sensitive operation of the interferometer in both voltage-biased and current-biased setups. However, given the significant capacitive load present in the filtered lines of our refrigerator setup, the current-biased measurement scheme shows better performance thanks to the superior common-mode noise rejection properties of differential voltage preamplification.

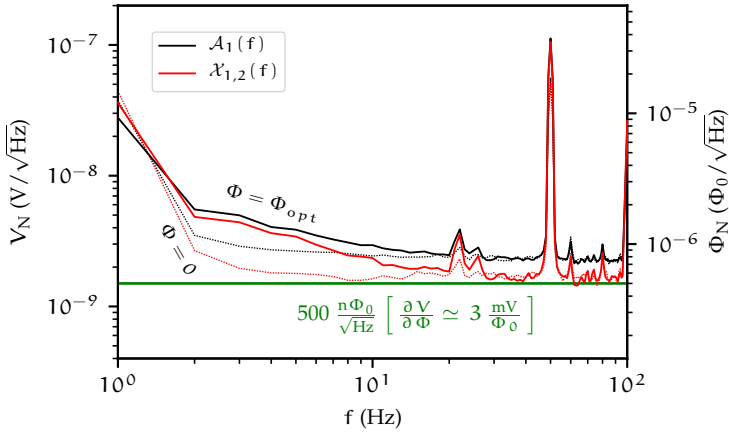


Figure 5.7: Noise level measurement in a current bias mode at 240 mK: power spectral density (\mathcal{A}_i , black traces) and cross spectral density ($\mathcal{X}_{1,2}$, red traces) of two preamplifier chains are expressed in voltage noise referred to the input of the preamplifiers (V_N , in $V/\sqrt{\text{Hz}}$ units). Continuous lines indicate traces recorded at optimal current and flux bias, where the transfer function is maximal ($3 \text{ mV}/\Phi_0$). The right vertical axis shows the values for the magnetic flux resolution (Φ_N) under these conditions. The $500 \text{ n}\Phi_0/\sqrt{\text{Hz}}$ white noise level is shown as a green horizontal line. Dotted lines indicate control traces recorded with optimal current bias at $\Phi = 0$ (zero transfer function and comparable differential resistance).

Figure 5.7 shows an assessment of the noise performance of the SQUIPT as a magnetic flux sensor obtained at 240 mK by measuring the power spectral density of voltage fluctuations recorded at the output of battery powered differential voltage preamplifiers (NF Corporation model LI-75A). Two identical preamplification units are connected to the two independent ADC channels of a spectrum analyzer (HP model 89410A), which computes the PSD of each channel as well as the CSD between the two. The latter quantifies the amount of noise which shows as correlated in the two ADC channels, and sets an upper limit to the estimate of the intrinsic noise figures for the measurement setup. The SQUIPT device is operated in the current-bias mode with $I_b = 435$ pA. The spectral densities (both PSD and CSD) are expressed in amplitude units (V_N , in $V/\sqrt{\text{Hz}}$); the expected bandwidth of the measurement setup ($\simeq 20$ Hz when tuned for high sensitivity) is here limited by the significant capacitance of the filtered measurement lines ($\simeq 90$ nF).

The continuous-line traces in fig. 5.7 were acquired with the device tuned for maximum sensitivity ($|\partial V/\partial \Phi|_{\text{max}} = 3$ mV/ Φ_0 and $\Phi_{\text{opt}} = 0.495 \Phi_0$). In these conditions, besides some spurious noise peaks, the input-referred white noise level for the preamplifiers (black trace) approaches the nominal limit for this model (2 nV/ $\sqrt{\text{Hz}}$), while the cross-correlated white noise level (red trace) reaches values as low as $1.5 \mu\Phi_0/\sqrt{\text{Hz}}$. Control traces, shown as dotted lines, were acquired with $I_b = 435$ pA but zero magnetic flux (and hence zero transfer function, yet similar differential resistance). They differ from the maximum-sensitivity traces for the absence in the 2 Hz to 20 Hz frequency range of a $1/f$ slope whose level (assuming a field-to-voltage coefficient $A_{\text{eff}}|\partial V/\partial \Phi|_{\text{max}} \simeq 4.8$ V/T) is consistent with the expected magnetic low-frequency noise found in unshielded rooms in urban environment (typically in the $0.1 - 1$ nT/ $\sqrt{\text{Hz}}$ range at 10 Hz [49]).

The white-noise floor displayed in the CSD traces is significantly lower than the corresponding levels from the single-channel PSD, meaning that the room-temperature preamplification stage is here limiting the noise performance of the measurement setup. The cross-correlated voltage

white-noise floor sets an upper limit to the magnetic flux resolution achievable by our measurement setup,

$$\Phi_N = \frac{V_N}{|\partial V/\partial \Phi|} \simeq 500 \text{ n}\Phi_0/\sqrt{\text{Hz}}. \quad (5.1)$$

In spite of the relatively simple measurement equipment used, this noise figure is already comparable with state-of-the-art [SNS SQUID](#) interferometers equipped with custom cryogenic preamplification readout systems [50, 51].

5.4 DISCUSSION

The key challenge in developing an effective [SQUIPT](#) magnetometer is establishing sizeable flux-to-voltage responsivity figures. This requires *both* a broad minigap in the proximized weak link and effective flux-to-phase bias conditions in the interferometer as a whole. Adopting wide-gap superconductors [63, 64] and designing the proximized weak link to be in the short limit are effective ways of satisfying the former requirement. However, the concomitant increase of the critical current directly hampers the phase-bias mechanism in the interferometer, in particular if the superconductor of choice is characterized by significant kinetic inductance.

In our design, the choice of aluminum grants ease of fabrication and low kinetic inductance. The short yet resistive copper weak link allows the complete phase bias of the minigap, yielding a flux-to-voltage modulation amplitude reasonably close to the ideal value of Δ_T/e . All in all, successful [SQUIPT](#) design is an exercise in nanofabrication. This is evident from our devices (see fig. 5.2), in particular with respect to the nanoscale geometry of the copper weak link and its contact with the readout tunnel electrode.

Compared with [SNS SQUID](#)s presented in the previous chapters, the readout is characterized by typical impedance values ($\approx 10 \text{ k}\Omega$) that are a better match to the differential input stage of [DC](#) voltage [LNAs](#). A figure of merit marking an important difference with respect to [SQUID](#)s

(of both SNS and SIS types) is the dissipated power. As a consequence of the minute current levels typically associated with subgap quasiparticle conductance, the power dissipated in the readout reaches here values as low as ≈ 100 fW. The supporting publication “Normal metal tunnel junction-based superconducting quantum interference proximity transistor” [5] demonstrates the feasibility of sub-femtowatt readout of a SQUIPT equipped with a normal-metal tunnel probe.

On the other hand the relatively high impedance of the tunnel barrier yields a proportionally low DC readout bandwidth, limiting the response time to the millisecond timescale; this value is not strictly an intrinsic limitation, but partly derives from the high shunt capacitance introduced by the signal filters adopted in the cryogenic setup. Nevertheless, schemes to couple RF readout to tunnel barriers in contact with proximized systems have been recently demonstrated [65, 66], a promising development to bring SQUIPT devices to fully outperform SQUIDs for ultrasensitive microscale magnetometry at sub-Kelvin temperatures.

ALUMINUM-BASED SQUIPTS

In the previous chapter it has been shown that a sensible design in both the superconducting ring and the normal-metal weak link is crucial to obtain full phase polarizability of the latter. For a sinusoidal CPR, this property is granted by an inductive screening parameter¹ $\beta_L < 1$. On the other hand, the amplitude of the voltage response in SQUIPT devices is proportional to the width of the energy gap in the LDOS sampled by the tunnel probe electrode. Therefore, in order to enhance the performance of SQUIPT magnetometers in terms of both operating temperature and voltage modulation it is helpful to maximize the energy gap in the proximized element. This goal can be achieved by ensuring that the latter is in the *short* regime (i. e., $E_{Th} \approx \Delta$), and by adopting a superconductor with sufficiently high critical temperature.

However, most high-gap elemental superconductors (such as vanadium, niobium, or lead) are also characterized by significant normal-state resistivity. As a consequence, a strong kinetic term is to be factored in the total ring inductance. This generally implies tighter requirements on the geometry of the interferometer in order to achieve full phase polarizability of the proximized weak link. In this chapter, instead, we explore the consequences of the unconventional idea of substituting the proximized normal-metal (copper) with an intrinsic superconductor (aluminum). The weak link in the resulting SQUIPT interferometers can be then considered as a geometrical constriction in a compositionally homogeneous ring. More precisely, the weak link consists in a SSS junction whose geometrical length is designed to be comparable with the coherence length of the constituent superconductor².

¹ See eq. (1.22) in section 1.4 for the definition of β_L .

² For aluminum films of 10 nm to 200 nm thickness, ξ is typically in the 50 nm to 150 nm range, depending on the electron elastic mean free path.

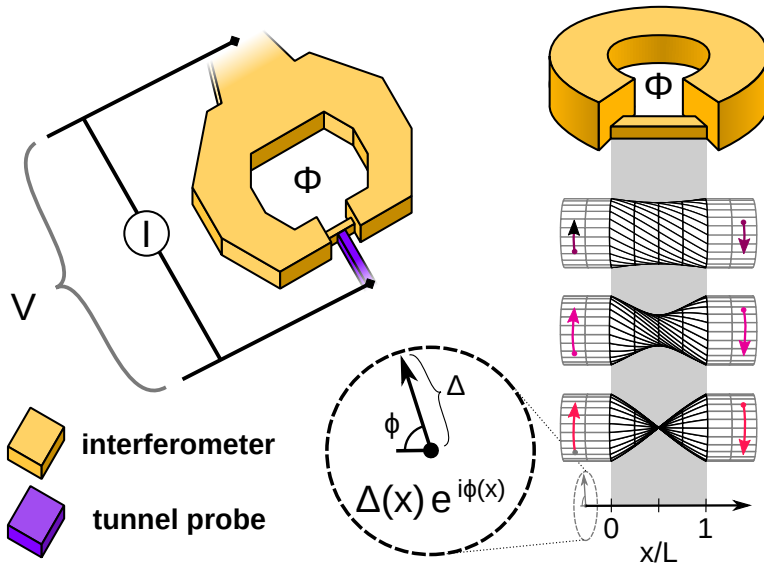


Figure 6.1: **SQUIPT** based on a **SSS** weak link. The tunnel probe readout scheme is shown in the top left part of the figure. The progressive collapse of the pairing potential amplitude in the middle of a short superconducting wire for increasing phase gradient is conceptually shown in the right part of the figure. The position-dependent value of the complex order parameter inside the wire is shown as a twisted-wireframe representation of a revolution surface. The phase bias enforced by the rigid electrodes (grey wireframe) acts as a “torque” on the self-consistent pairing potential in the wire (black wireframe). The singular cone-like shape with $\Delta(L/2) = 0$ is relative to the **SSS** weak link being biased at the π node of its **CPR**.

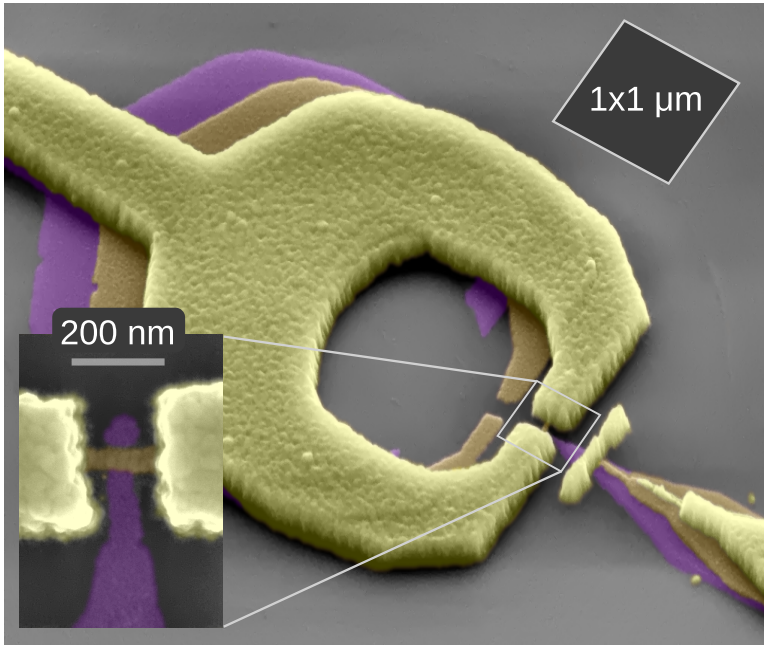


Figure 6.2: Tilted pseudo-colour scanning electron micrograph of a typical *SSS SQUIPT* device. The bottom left inset shows a zoomed-in perpendicular view of the weak link region. Physical size scales are indicated in both micrographs. Here, yellow indicates the 150 nm-thick “interferometer” and 25 nm-thick “nanowire” Al layers; the 15 nm-thick AlO_x tunnel probe electrode is shown in purple, realized by oxidizing respectively a Al/Al_{0.98}Mn_{0.02} metallic film to obtain a superconducting/normal-metal electrode.

By recording the magnetic flux response of the current-voltage characteristics as a function of temperature, we find evidence of the transition between a multi-valued and a single-valued CPR dependence for the superconducting weak link, in accordance with the theoretical expectations listed at the end of section 1.7 for diffusive SSS junctions. In the single-valued CPR regime a complete suppression of the gap in the quasiparticle excitation spectrum of the superconducting wire is observed. This phenomenon can be understood as the coherent³ collapse of the order parameter inside the superconducting wire, and is presented in the first section of this chapter.

Notably, the transition between multi and single-valued CPR regime entails a temperature-tunable singularity in the response to magnetic flux, originating from the resolution of hysteresis in the phase bias of the superconducting constriction. This is exploited in the second section of this chapter, where a review of magnetometric performance of SSS SQUIPTS is presented. These devices show significant improvements in terms of flux noise resolution, bandwidth and optimal operating temperature with respect to their SNS counterparts. The chapter is concluded by a review on the significance of the results.

6.1 COHERENT COLLAPSE OF THE ORDER PARAMETER

Superconducting depairing is defined as the suppression of the spatial density of Cooper pairs. It can be induced, beside temperature, by sources of time-reversal symmetry breaking. The latter includes kinetic effects, where a non-zero condensate *velocity* reduces the number of time-reversed electronic states that can be self-consistently paired up to form the condensate⁴.

Depairing affects the spectral properties of the superconducting condensate. This has been shown experimentally in [44] for a translationally invariant system constituted by a thin⁵ superconducting wire subjected

³ I. e., caused by the *phase bias* of the interferometer.

⁴ See e. g., [12], pag. 125.

⁵ Compared to the magnetic penetration depth.

to current bias and application of a magnetic field orthogonal to the wire axis. The DOS of quasiparticle excitations has been measured by tunnel-probe spectroscopy, revealing that both current bias and applied magnetic field induce an equivalent deformation in the excitation spectrum of the condensate via the manipulation of its momentum. In particular, the energy gap in the quasiparticle DOS is shown to be progressively suppressed by the increasing phase gradient of the order parameter⁶, although not completely.

On the other hand, a properly designed SQUIPT interferometer applies a superconducting phase difference directly on a diffusive weak link. When the latter is an intrinsic superconductor having a geometrical length comparable to its coherence length, significant phase gradient values can be expected as soon as the interferometer is flux-biased. As shown numerically in section 1.7, when diffusive SSS weak links are biased beyond the critical current up to the $\theta = \pi$ node of their CPR, the self-consistency requirement for the pairing potential forces the latter to suppress its amplitude in the middle of the superconducting wire. In this specific state no supercurrent flows in the Cooper condensate and, by virtue of time-reversal symmetry, its order parameter $\Delta \exp(i\phi)$ is a real-valued and sign-changing function of the spatial coordinate along the wire. Then, as a consequence of continuity, the pairing potential amplitude $\Delta(x)$ must equal zero in some position inside the wire (e.g., the centre in case of symmetric boundaries)⁷.

This concept is shown in fig. 6.1, where the spatial profile of the complex order parameter is represented for increasing depairing conditions. In particular, complete pairing potential suppression is expected when the diffusive SSS weak link is exactly biased at the $\theta = \pi$ node of its CPR. As thoroughly discussed in section 1.7, the possibility to achieve $\theta = \pi$ node bias depends on the normalized length of the supercon-

⁶ The phase gradient is proportional to the canonical momentum of the condensate. In the latter the kinetic and the magnetic-coupling terms can be manipulated independently.

⁷ Notably, while wide (compared to ξ) weak links can accommodate Abrikosov vortices, here we consider quasi-1D wires (thinner than ξ). They develop pinned 1D phase singularities without any screening supercurrents [15].

ducting wire. In fact, while short *SSS* weak links are characterized by a proper single-valued *CPR* functional form, in the long-wire limit even a $\theta = \pi$ phase difference can be matched by an approximately uniform phase gradient in the wire, corresponding to non-zero supercurrent values. The resulting anomalous multi-valued *CPRs* can be reverted to the single-valued regime under the influence of sufficiently high temperature⁸.

6.2 TRANSPORT SPECTROSCOPY

We first consider *SQUIPT* devices designed with the intent of studying the *LDOS* of the phase-biased *SSS* weak link. To this end, a normal-metal tunnel probe electrode would be the ideal tool, due to the direct proportionality between the observed differential conductance and the probed *DOS* in the low temperature limit, as shown in eqs. (1.36) and (1.37). To realize a normal-metal probe *SQUIPT*, 2% Mn-doped Al alloy has been adopted as a drop-in replacement for the pure Al deposition for the tunnel electrode fabrication in the protocol introduced in the previous chapter. At this doping level, any superconducting gap in the AlMn alloy is effectively suppressed [46]. At the same time, tunnel barriers can be grown by controlled oxidation with similar parameters and final quality as in the case of pure Al. Figure 6.2 show a scanning electron micrograph of a completed typical *SSS SQUIPT* interferometer. Here the tilted image allows to appreciate the strong geometrical contrast in the cross-section of the interferometer loop compared to the superconducting constriction represented by the *SSS* weak link. As thoroughly discussed in the previous chapter, this design is required to ensure complete phase polarizability of short diffusive weak links.

The electron transport properties of the device have been characterized in the *Triton* setup, a dilution refrigerator able to access the 0.02 K to 1.0 K range. The modulation of the current-vs-voltage $I(V_b)$ characteristics of a typical (wire length $L = 160$ nm) normal-metal tun-

⁸ Compare e. g., figs. 1.20 and 1.22.

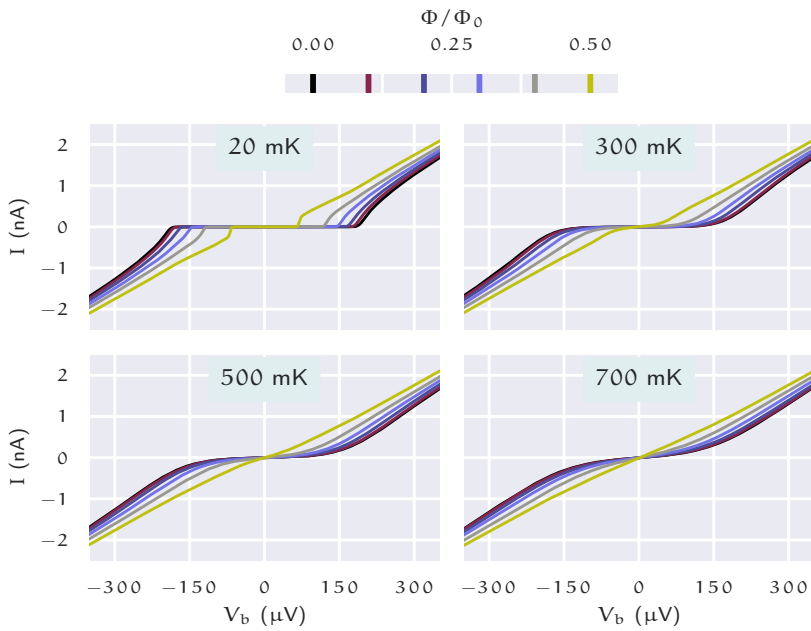


Figure 6.3: Magneto-electric response of a typical normal-metal tunnel probe device. Current-vs-voltage characteristic curves, recorded at lattice temperature $T = 20, 300, 500$ and 700 mK, respectively. The different traces in each panel are color-coded to six applied magnetic flux values equally spaced in the range $\Phi = 0 \rightarrow \Phi_0/2$.

nel probe device (tunnel resistance $R_T \approx 150 \text{ k}\Omega$) as a function of the magnetic flux Φ applied orthogonally to the interferometer by a superconducting coil is presented in figs. 6.3 and 6.4. At base temperature ($T = 20 \text{ mK}$) increasing the magnetic flux bias from $\Phi = 0$ to $\Phi = \Phi_0/2$ already results in a significant 65 % suppression of the energy gap in the quasiparticle DOS compared to its zero-field value. Notably, the low-temperature differential conductance characteristics (obtained under fixed voltage bias with a Lock-In Amplifier (LIA) and shown in the upper panel of fig. 6.4) recorded for $\Phi/\Phi_0 < 0.25$ are compatible with data reported for specimens in the current-biased (i. e., constant phase gradient) regime [44]. This is expected since in this flux range, the CPR is essentially linear, so that phase and current bias are interchangeable.

On the other hand, for $\Phi/\Phi_0 \approx 0.5$, a peculiar concentration of quasiparticle states at the edges of the residual energy gap can be inferred from the experimental data. The latter feature, absent in short phase-biased normal-metal wires [5], appears reproducibly between different samples, provided a sufficient phase difference is applied to the short superconducting wire. By inspecting characteristic curves recorded at increasing temperature ($T = 300, 500$ and 700 mK) evidence of the progressive suppression of the residual energy gap at $\Phi = \Phi_0/2$ can be gathered. The magnetic modulation of the differential conductance recorded at $T = 650 \text{ mK}$ (lower panel in fig. 6.4) shows the transition between a NIS-like response at zero field to an essentially⁹ ohmic (i. e., NIN-like) response at $\Phi = \Phi_0/2$.

These observations can be understood by considering the temperature response [15] of the CPR of a weak link based on a superconducting wire in contact with rigid superconducting electrodes. Figure 6.5 shows the comparison between observed differential conductance data and theoretical prediction stemming from the LDOS of a phase-biased SSS

⁹ The small residual conductance dip that can still be observed for $|V_b| < 200 \mu\text{V}$ is consistent with effects related to the interaction with the photonic environment, as allowed by the significant charging energy of the nanosized tunnel junction (with capacitance $\approx 100 \text{ aF}$). For further details, compare with the bottom right panel in fig. 1.13, and the corresponding derivation in chapter 1.

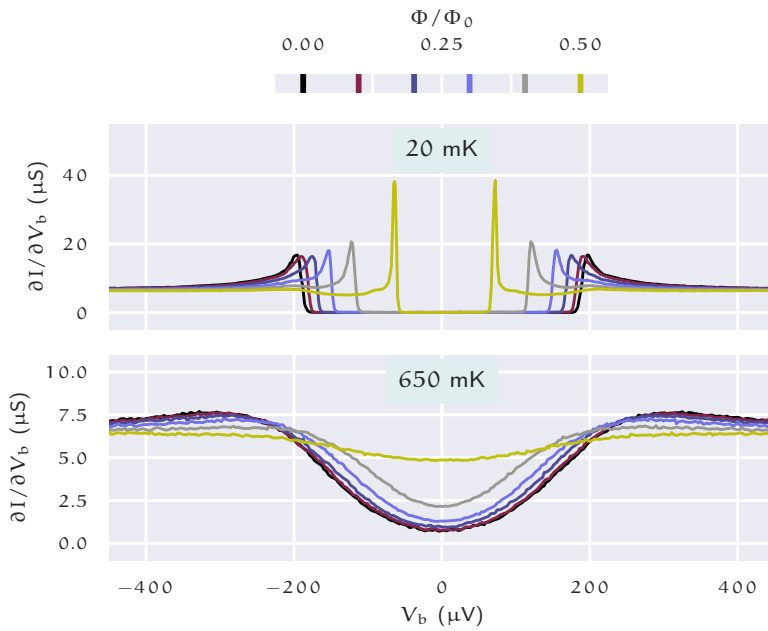


Figure 6.4: Magneto-electric response of a typical normal-metal tunnel probe device. Differential conductance as a function of voltage bias, recorded at lattice temperature $T = 20$ and 650 mK, respectively. The different traces in each panel are color-coded to six applied magnetic flux values equally spaced in the range $\Phi = 0 \rightarrow \Phi_0/2$.

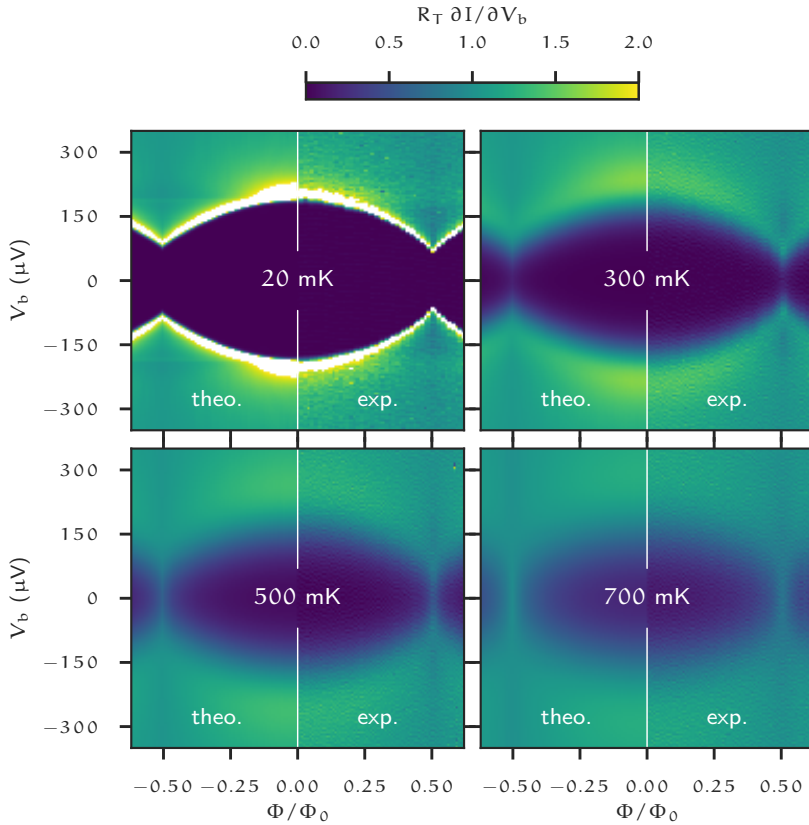


Figure 6.5: Normalized differential conductance of the normal-metal tunnel probe device as a function of the applied magnetic flux and voltage bias V_b at lattice temperature $T = 20, 300, 500$ and 700 mK, respectively. The halves of each colormap plot allow the comparison between theoretical predictions (left) and experimental data (right).

weak link computed in the quasiclassical framework by solving the Usadel equations self-consistently with the pairing amplitude profile, according to the methods reported in chapter 1. Figure 6.6 shows a synopsis of the “internal” SSS-related quantities correspondingly obtained in this modelization effort.

For reference, these numerical datasets have been generated assuming the critical temperature values $T_{c,w} = 1.4$ K for the thin wire and the bulk value $T_{c,r} = 1.25$ K for the thick ring. The modeled diffusive weak link has normalized length $L/\xi_0 = 1.7$, corresponding to $\xi_0 = \sqrt{\hbar D/\Delta_0} = 95$ nm for a physical length $L = 160$ nm. The interfaces of the wire are modeled with a non-ideality coefficient $r = 0.75$. The values of the set of mutually-independent parameters $T_{c,w}$, ξ_0 and r are chosen on the basis of optimal reproduction of the differential conductance characteristic curve recorded for null magnetic field at $T = 20$ mK. Optimal agreement with the observed flux modulation at all temperatures is obtained by letting $\beta_L = 0.03$, consistent with $I_c \approx 18$ μ A deduced from the former parameters if the total interferometer inductance is¹⁰ $\mathcal{L} = 3.5$ pH.

As the temperature increases, the CPR of the weak link progressively shifts from a multi-valued $I_s(\Phi)$ at low-temperature [characterized by metastable $\Phi = \Phi_0(n + 1/2)$ nodes] to a single-valued functional form reached at $T = 700$ mK. In the latter regime the amplitude of the pairing potential in the centre of the wire can be completely suppressed by applying a phase difference equal to π (lower panel of fig. 6.6). The striking correspondence observed between data recorded at different temperatures and the corresponding theoretical prediction in fig. 6.5 corroborates the physical interpretation of complete pair potential suppression in the superconducting wire for $\Phi/\Phi_0 = 0.5$.

¹⁰ This value of the inductance of the superconducting loop including both geometric and kinetic contributions, has been numerically estimated from the actual interferometer geometry with the software *FastHenry version 3.0wr* by S. R. Whiteley (available from <http://wrcad.com>). The calculated value corresponds to an effective magnetic penetration depth $\lambda_{\perp} \approx 60$ nm, which is compatible with a 150 nm-thick Al film.

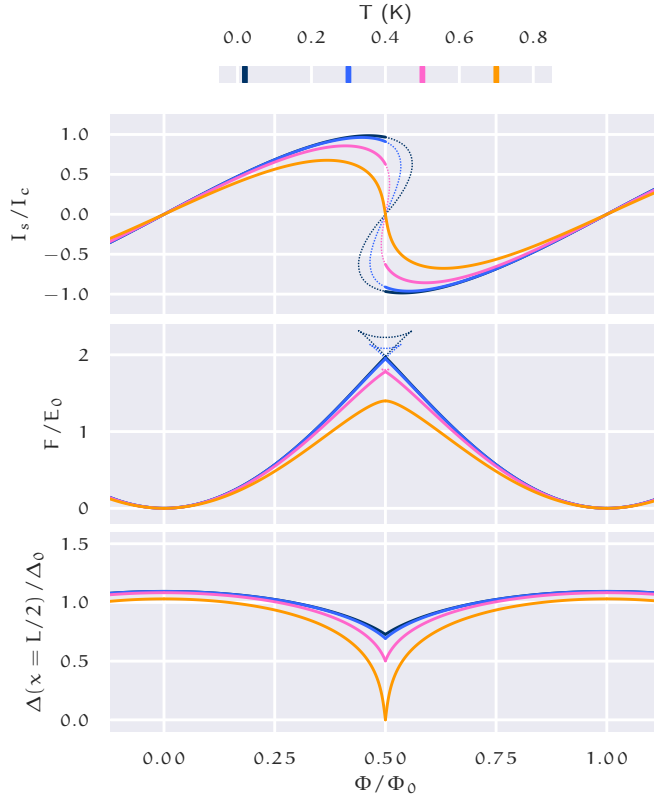


Figure 6.6: Results for the modelization of the superconducting nanowire according to parameters inferred from experimental data. The top panel shows the circulating supercurrent I_s normalized to the zero-temperature value of the critical current of the wire (I_c). The middle panel shows the free energy F normalized to $E_0 = I_c \Phi_0 / 2\pi$. The bottom panel shows the pairing potential amplitude $\Delta(x = L/2)$ in the center of the superconducting nanowire normalized to the zero-temperature value of the pairing potential amplitude in the interferometer loop (Δ_0). The different traces are color-coded to the temperature values $T = 20, 300, 500$ and 700 mK, and show the modulation of the respective quantity as a function of the magnetic flux Φ applied to the interferometer. Dotted branches in the first and second panels represent theoretical solutions corresponding to thermodynamically unstable interferometer states.

6.3 MAGNETOMETRIC PERFORMANCE

The phase-driven collapse of the pairing potential is further confirmed by observations focused on the transition from the unstable to stable π phase bias regime in devices equipped with a superconducting tunnel electrode. The latter, realized by a 15 nm-thick oxidized Al film, features a BCS-like DOS characterized by a sizeable superconducting gap $\Delta_{pr} \approx 250 \mu\text{eV}$, typical of thin Al films. As a consequence, the spectroscopic sampling of the DOS in the phase-biased wire does not suffer from the loss of energy resolution due to thermal broadening typical of normal-metal probes. In particular, this setup allows for a direct estimate of the energy gap $\varepsilon_g(\Phi)$ in a generically-gapped DOS. At finite temperature, the latter quantity can be derived [59] from the difference between voltage bias values relative to the direct and thermally-activated conductance peaks (found, respectively, at $eV_b = \Delta_{pr} \pm \varepsilon_g$, similarly to the well-known case of quasiparticles tunneling between different superconductors at nonzero temperature [12]).

The top panels of fig. 6.7 show normalized differential conductance maps recorded for a representative device characterized by a $L = 210 \text{ nm}$ superconducting wire in contact with a $R_T = 15 \text{ k}\Omega$ superconducting tunnel electrode. The mapping is focused on voltage bias values corresponding to the superconducting gap in the probe ($eV_b \approx \Delta_{pr}$) and with coupled magnetic flux applied in a minute range centered around $\Phi_0/2$. By inspecting the flux modulation of the direct ($eV_b > \Delta_{pr}$) and thermally-activated ($eV_b < \Delta_{pr}$) conductance peaks, an incomplete suppression of $2\varepsilon_g \simeq 40 \mu\text{eV}$ can be inferred from data recorded at $T = 0.9 \text{ K}$ (topmost panel). Within a 100 mK temperature increase, we observe the merging of the direct and thermally-activated peaks at $\Phi/\Phi_0 = 0.5$ and $eV_b = \Delta_{pr}$, the direct evidence of the full suppression of the energy gap in the probed quasiparticle DOS. Equivalently (lower panels), the latter is associated with a smooth monotonic $I(V_b)$ characteristic curve at $T = 1 \text{ K}$ for $\Phi/\Phi_0 = 0.5$, whereas the corresponding curve at $T = 0.9 \text{ K}$ displays a $\simeq 40 \mu\text{V}$ -wide plateau.

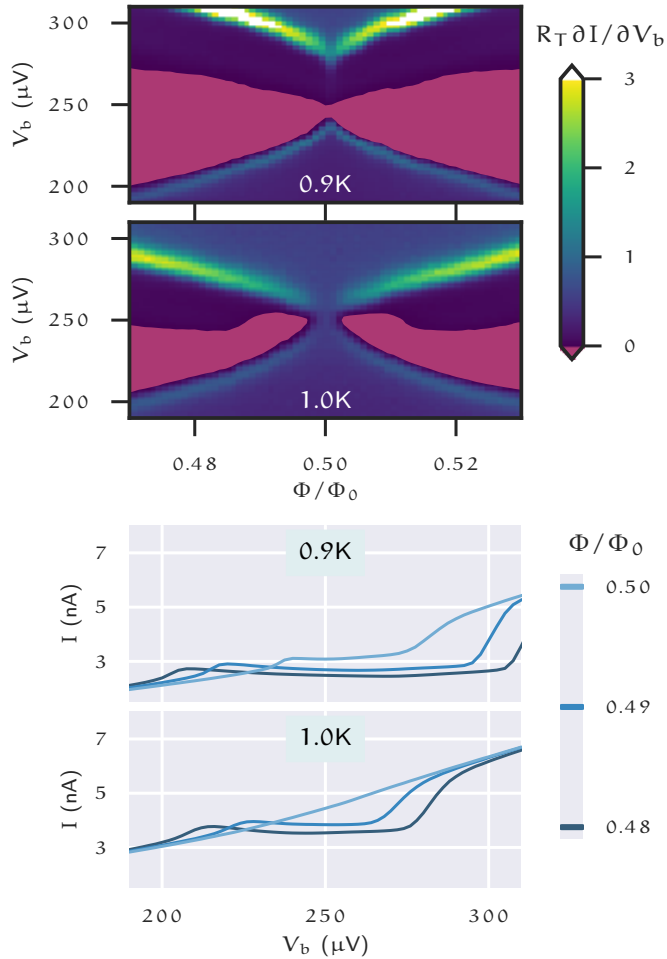


Figure 6.7: *Superconducting* tunnel probe spectroscopy of the phase-driven collapse of the superconducting gap in the Al nanowire. The two topmost panels show the normalized differential conductance as a function of the applied magnetic flux and voltage bias, recorded at lattice temperature $T = 0.9$ and 1.0 K, respectively. The region showing negative differential conductance is indicated in magenta. The two lowermost panels show the current-vs-voltage characteristic curves recorded for $\Phi/\Phi_0 = 0.48, 0.49, 0.5$ and for the same lattice temperature values.

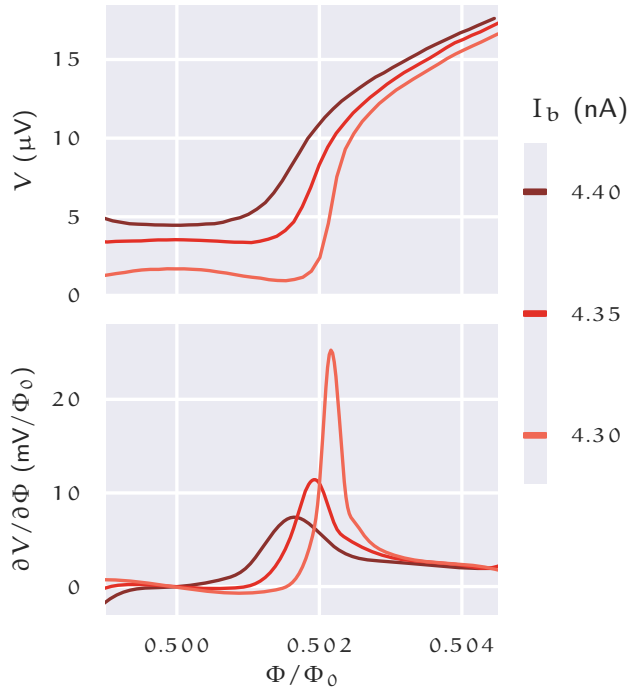


Figure 6.8: Magneto-electric response of a typical *superconducting* tunnel probe device. The top and bottom panel show, respectively, voltage response (arbitrary offset) and corresponding flux-to-voltage transfer function for $\Phi \approx \Phi_0/2$, recorded at temperature $T = 1.0\text{K}$. The device is here operated under fixed current bias values $I_b = 4.30, 4.35$ and 4.40nA .

We interpret these observations as the confirmation that the increase in temperature has driven the CPR of the weak link to the single-valued regime, leading to a complete collapse of the amplitude of the pairing potential in the center of the wire for $\Phi/\Phi_0 = 0.5$. In this case, the temperature value for this transition is higher than for the normal probe interferometer (figs. 6.5 and 6.6) as expected from the difference in the respective lengths of the wires, in agreement with the theory. Notably, while the value $T = 1$ K is arguably sizeable, it is also significantly smaller than the critical temperature $T_{c,w} = 1.4$ K of the 25 nm-thick Al film the wire consists of.

The steep character of the magnetic flux dependence of the pairing potential suppression suggests to exploit these devices for highly-sensitive magnetometry applications. Inspection of voltage traces recorded at $T = 1$ K under constant current bias I_b from the representative superconducting probe device (top panel in fig. 6.8) reveals abrupt but continuous voltage response in a minute magnetic flux range close to $\Phi/\Phi_0 = 0.5$. Here, the different traces indicate current bias values in the 4.3 nA to 4.4 nA range, matching the typical quasiparticle current measured in the voltage-biased setup with $V_b \approx \Delta_{pT}/e = 250$ μ V. The corresponding flux-to-voltage responsivity characteristics (*ibidem*, lower panel) obtain values as large as ~ 27 mV/ Φ_0 , which are unparalleled in this class of devices [3, 5].

The magnetic flux resolution of the SSS SQUIPT operated as a magnetometer has been estimated from the analysis of the cross-correlation between the output signals of two parallel amplification chains connected to the same device. As argued in section 2.3, this configuration allows to distinguish amplifier-limited magnetic flux resolution performance from noise sources intrinsic to the readout scheme.

Figure 6.9 shows a summary of the noise characterization of the representative superconducting probe device for $\Phi \approx \Phi_0/2$, measured at temperature $T = 1$ K under fixed current $I_b = 4.35$ nA. The noise characteristic of the readout/amplifier system can be assessed by tuning the applied magnetic flux to $\Phi = \Phi_0/2$, where the flux-to-voltage response is null to the first order in Φ . In this configuration (upper

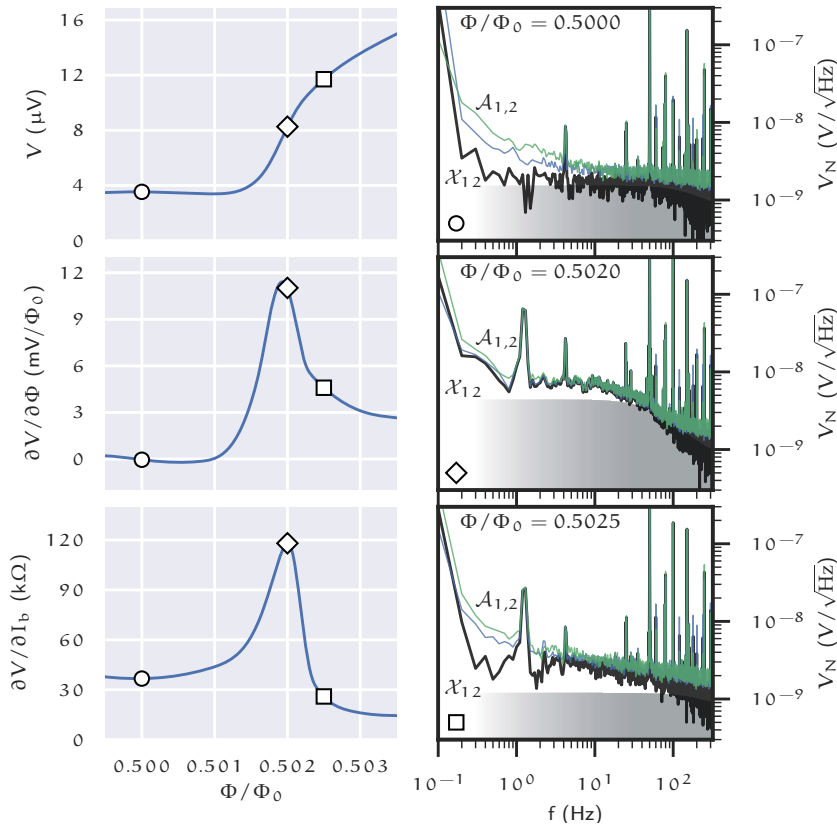


Figure 6.9: Summary of the magnetoelectric response figure of a typical superconducting probe device recorded at temperature $T = 1$ K and current bias $I_b = 4.35$ nA. The leftmost panels show as a function of the applied flux Φ , respectively, the DC voltage, the flux-to-voltage transfer function and the differential conductance. The spectral characteristics of the amplified signal (green/blue traces: individual-channel power spectral density $\mathcal{A}_{1,2}$, black trace: cross-spectral density \mathcal{X}_{12} , gray shading: readout noise floor estimate) are presented in the rightmost panels for three illustrative flux working points. The top panel corresponds to zero first-order response ($\Phi/\Phi_0 = 0.5$), while the middle and bottom panels are relative to the device being tuned for highest responsivity and best noise-equivalent flux resolution, respectively.

left panel) the PSD profiles of the individual preamplifiers (green/blue traces) are only barely higher than their nominal datasheet values, whereas the cross-spectral density (black trace) converges to a profile $\mathcal{X}_{12}(f)$ consistent with the following model (gray shade):

$$\mathcal{X}_{12}(f) = \sqrt{v_a^2 + R_d^2 \frac{2eI_b}{|1 + 2\pi i f R_d \mathcal{C}|^2}} \quad , \quad (6.1)$$

where $v_a = 0.7 \text{ nV}/\sqrt{\text{Hz}}$ is a white noise background, e is the elementary charge, $R_d = \partial V/\partial I_b$ is the differential resistance and $\mathcal{C} = 26 \text{ nF}$ is the effective shunt capacitance consistent with the noise roll-off observed for $f \approx 100 \text{ Hz}$. This simple model, based on the quadrature summation of RC-filtered tunnel shot noise with an amplifier-limited cross-correlated white noise background is sufficient to describe \mathcal{X}_{12} data recorded for $0.3 < f < 300 \text{ Hz}$.

In fig. 6.9, a comparison between the leftmost panels shows that the peak in the flux-to-voltage transfer function is correlated with a corresponding peak in the differential resistance of the device ($\Phi/\Phi_0 = 0.502$). On the other hand, the latter is suppressed with $\Phi/\Phi_0 > 0.5025$, while the flux-to-voltage transfer function maintains appreciable levels. The noise characterization presented in the rightmost panels shows indeed that at the working point associated with maximal responsivity the power spectral density of the individual amplifiers is basically indistinguishable from the cross-correlated spectrum, *i.e.*, the v_a term is negligible in Equation 6.1 compared to the shot noise term.

However, at this working point, the high value of R_d entails both a reduction in the available bandwidth and an increase of the shot-noise contribution to the observed voltage spectral density, lowering the effective Signal to Noise Ratio (SNR). By contrast, the bottom right panel, which corresponds to a working point ($\Phi/\Phi_0 = 0.5025$) associated with a significantly lower value of R_d , demonstrates a $\mathcal{X}_{12}(f)$ profile characterized not only by wider available RC bandwidth, but also slightly improved SNR (as suggested by the shape of the 1.3 Hz signal peak originating from mechanical vibrations induced by the pulse-tube cooler).

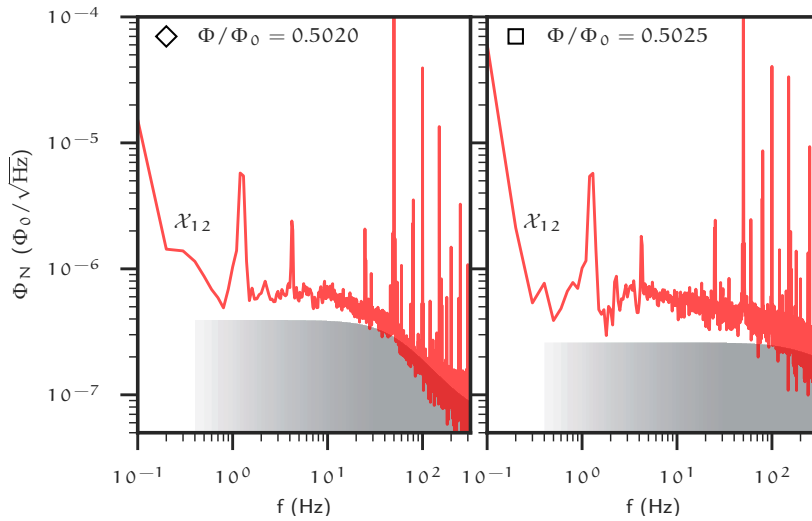


Figure 6.10: Cross-spectral density \mathcal{X}_{12} (red trace) and readout noise floor estimate (gray shading) in magnetic flux units. Left and right panels correspond, respectively, to the device tuned for highest responsivity ($\Phi/\Phi_0 = 0.502$) and for best noise-equivalent flux resolution ($\Phi/\Phi_0 = 0.5025$).

This difference in performance can be more quantitatively appreciated by renormalizing the spectral density profiles from voltage to magnetic flux units by means of the flux-to-voltage transfer function values. The results are shown in fig. 6.10. A summary of the performance figures for the different working points is reported in table 6.1.

Φ (Φ_0)	$\partial V/\partial\Phi$ (mV/ Φ_0)	R_d (k Ω)	noise floor		bandwidth (Hz)
			(nV/ $\sqrt{\text{Hz}}$)	(n Φ_0 / $\sqrt{\text{Hz}}$)	
0.5	0.0	36.7	1.5	—	167
0.502	11.3	117.	4.4	390	52
0.5025	4.6	26.2	1.2	260	234

Table 6.1: Summary of magnetometric figures for the representative superconducting probe [SSS SQUIPT](#), operated at the working points of [fig. 6.10](#).

6.4 DISCUSSION

In summary, we have presented a robust and reproducible means of suppressing the order parameter amplitude of the Cooper condensate inside a nanosized superconductor. Our observations are consistent with established theory. Reaching the complete flux modulation of the energy gap in the [DOS](#) inside the superconducting wire marks the transition between the *intrinsic*-like and *Josephson*-like regime of the [SSS](#) weak link. The corresponding temperature-dependent modulation of the [CPR](#) from a multi-valued locus to a proper single-valued form entails, at the cross-over, a strong dependence of the physical observables on the applied magnetic flux for $\Phi \approx \Phi_0/2$.

This property finds immediate application for the realization of ultra-sensitive micro-magnetometers. In this context, [SQUIPTs](#) based on [SSS](#) weak links demonstrate several points of improvement compared to the [SNS](#) counterparts presented in the previous chapter. At the optimal working point, the [SSS SQUIPT](#) operates with a magnetic flux resolution twice as good with one order of magnitude improvement in the available bandwidth. Additionally, the 1 K operating temperature makes this type of device compatible with continuous Joule-Thomson cooling systems. Finally, opposed to tarnishable Cu weak links, the self-passivation of Al structures makes this design intrinsically robust against aging and corrosion.

BIBLIOGRAPHY

- [10] R. P. Feynman. "There's plenty of room at the bottom: An invitation to enter a new field of physics." In: *Handbook of Nanoscience, Engineering, and Technology, Third Edition*. CRC Press, 2012, pp. 26–35.
- [11] F. Pobell. *Matter and methods at low temperatures*. Springer, 2007.
- [12] M. Tinkham. *Introduction to Superconductivity*. Courier Corporation, 1996.
- [13] P-G. De Gennes. *Superconductivity of metals and alloys*. Advanced Book Program, Perseus Books, 1999.
- [14] J. Bardeen, L. N. Cooper, and J. R. Schrieffer. "Theory of Superconductivity." In: *Physical Review* 108.5 (1957), pp. 1175–1204.
- [15] K. K. Likharev. "Superconducting weak links." In: *Reviews of Modern Physics* 51.1 (1979), pp. 101–159.
- [16] A. A. Golubov, M. Yu. Kupriyanov, and E. Il'ichev. "The current-phase relation in Josephson junctions." In: *Reviews of Modern Physics* 76.2 (2004), pp. 411–469.
- [17] B. D. Josephson. "Possible new effects in superconductive tunnelling." In: *Physics Letters* 1.7 (1962), pp. 251–253.
- [18] R. Doll and M. Näbauer. "Experimental proof of magnetic flux quantization in a superconducting ring." In: *Physical Review Letters* 7.2 (1961), pp. 51–52.
- [19] B. S. Deaver and W. M. Fairbank. "Experimental evidence for quantized flux in superconducting cylinders." In: *Physical Review Letters* 7.2 (1961), pp. 43–46.
- [20] A. F. Andreev. "Thermal conductivity of the intermediate state of superconductors." In: *Sov. Phys. JETP*. 19 (1964), p. 1228.

- [21] P-G. De Gennes and D. Saint-James. "Elementary excitations in the vicinity of a normal metal-superconducting metal contact." In: *Physics Letters* 4 (1963), pp. 151–152.
- [22] L. G. Aslamazov and A. I. Larkin. "Letter." In: *Sov. Phys. JETP* 9 (1969), p. 87.
- [23] V. Ambegaokar and A. Baratoff. "Tunneling between superconductors." In: *Physical Review Letters* 10 (1963), p. 486.
- [24] F. Giazotto, T. T. Heikkilä, A. Luukanen, A. M. Savin, and J. P. Pekola. "Opportunities for mesoscopies in thermometry and refrigeration: Physics and applications." In: *Review of Modern Physics* 78.1 (2006), pp. 217–274.
- [25] R. C. Dynes, V. Narayanamurti, and J. P. Garno. "Direct measurement of quasiparticle-lifetime broadening in a strong-coupled superconductor." In: *Physical Review Letters* 41.21 (1978), pp. 1509–1512.
- [26] J. P. Pekola, V. F. Maisi, S. Kafanov, N. Chekurov, A. Kempinen, Yu. A. Pashkin, O.-P. Saira, M. Möttönen, and J. S. Tsai. "Environment-assisted tunneling as an origin of the Dynes density of states." In: *Physical Review Letters* 105.2 (2010), p. 026803.
- [27] G.-L. Ingold and Y. V. Nazarov. "Single charge tunneling: Coulomb blockade phenomena in nanostructures." In: *Proceedings of the NATO Advanced Study Institute*. Les Houches, France: Plenum Press, 1991.
- [28] J. J. A. Baselmans, A. F. Morpurgo, B. J. van Wees, and T. M. Klapwijk. "Reversing the direction of the supercurrent in a controllable Josephson junction." In: *Nature* 397.6714 (1999), pp. 43–45.
- [29] I. O. Kulik and A. N. Omel'Yanchuk. "Contribution to the microscopic theory of the Josephson effect in superconducting bridges." In: *JETP Letters* 21 (1975), p. 96.
- [30] Y. Nambu. "Quasi-particles and gauge invariance in the theory of superconductivity." In: *Physical Review* 117.3 (1960), pp. 648–663.

- [31] L. P. Gor'kov. "On the energy spectrum of superconductors." In: *JETP* 7.3 (1958), p. 505.
- [32] L. P. Gor'kov. "Microscopic derivation of the Ginzburg-Landau equations in the theory of superconductivity." In: *JETP* 9.6 (1959), p. 1364.
- [33] L. P. Gor'kov. "The critical supercooling field in superconductivity theory." In: *JETP* 10.3 (1960), p. 593.
- [34] G. Eilenberger. "Transformation of Gorkov's equation for type II superconductors into transport-like equations." In: *Zeitschrift für Physik* 214.2 (1968), pp. 195–213.
- [35] K. D. Usadel. "Generalized Diffusion Equation for Superconducting Alloys." In: *Physical Review Letters* 25.8 (1970), pp. 507–509.
- [36] W. Belzig, F. K. Wilhelm, C. Bruder, G. Schön, and A. D. Zaikin. "Quasiclassical Green's function approach to mesoscopic superconductivity." In: *Superlattices and Microstructures* 25.5–6 (1999), pp. 1251–1288.
- [37] M. Yu. Kupriyanov and V. F. Lukichev. "Influence of boundary transparency on the critical current of dirty SS'S structures." In: *JETP* 67.6 (1988), p. 1163.
- [38] Y. V. Nazarov. "Novel circuit theory of Andreev reflection." In: *Superlattices and Microstructures* 25.5–6 (1999), pp. 1221–1231.
- [39] C. J. Lambert, R. Raimondi, V. Sweeney, and A. F. Volkov. "Boundary conditions for quasiclassical equations in the theory of superconductivity." In: *Physical Review B* 55.9 (1997), pp. 6015–6021.
- [40] T. T. Heikkilä, J. Särkkä, and F. K. Wilhelm. "Supercurrent-carrying density of states in diffusive mesoscopic Josephson weak links." In: *Physical Review B* 66.18 (2002), p. 184513.
- [41] J. C. Hammer, J. C. Cuevas, F. S. Bergeret, and W. Belzig. "Density of states and supercurrent in diffusive SNS junctions: Roles of nonideal interfaces and spin-flip scattering." In: *Physical Review B* 76.6 (2007), p. 064514.

- [42] P. Virtanen and T. T. Heikkilä. "Thermoelectric effects in superconducting proximity structures." In: *Appl. Phys. A* 89 (2007), p. 625.
- [43] P. Dubos, H. Courtois, B. Pannetier, F. K. Wilhelm, A. D. Zaikin, and G. Schön. "Josephson critical current in a long mesoscopic SNS junction." In: *Physical Review B* 63.6 (2001), p. 064502.
- [44] A. Anthore, H. Pothier, and D. Esteve. "Density of states in a superconductor carrying a supercurrent." In: *Physical Review Letters* 90.12 (2003), p. 127001.
- [45] G. J. Dolan. "Offset masks for lift-off photoprocessing." In: *Applied Physics Letters* 31.5 (1977), pp. 337–339.
- [46] F. W. Smith. "Effect of manganese on the superconductivity of aluminum." In: *Journal of Low Temperature Physics* 6.5-6 (1972), pp. 435–443.
- [47] O. V. Lounasmaa. *Experimental principles and methods below 1K*. Academic Press, 1974.
- [48] R. C. Jaklevic, J. Lambe, A. H. Silver, and J. E. Mercereau. "Quantum interference effects in Josephson tunneling." In: *Physical Review Letters* 12.7 (1964), pp. 159–160.
- [49] J. Clarke and A. I. Braginski, eds. *The SQUID Handbook: Fundamentals and Technology of SQUIDS and SQUID Systems*. Vol. 1. Wiley-VCH, 2004.
- [50] R. Wölbing, J. Nagel, T. Schwarz, O. Kieler, T. Weimann, J. Kohlmann, A. B. Zorin, M. Kemmler, R. Kleiner, and D. Koelle. "Nb nano SQUIDS with high spin sensitivity for operation in magnetic fields up to 0.5T." In: *Applied Physics Letters* 102.19 (2013), p. 192601.
- [51] J. Nagel, O. F. Kieler, T. Weimann, R. Wölbing, J. Kohlmann, A. B. Zorin, R. Kleiner, D. Koelle, and M. Kemmler. "SQUIDS with sub-micron Nb/HfTi/Nb junctions for investigation of small magnetic particles." In: *Applied Physics Letters* 99.3 (2011), p. 032506.

- [52] C. P. García and F. Giazotto. "Josephson current in nanofabricated V/Cu/V mesoscopic junctions." In: *Applied Physics Letters* 94.13 (2009), p. 132508.
- [53] H. Courtois, M. Meschke, J. T. Peltonen, and J. P. Pekola. "Origin of hysteresis in a proximity Josephson junction." In: *Physical Review Letters* 101.6 (2008), p. 067002.
- [54] L. Angers, F. Chiodi, G. Montambaux, M. Ferrier, S. Guéron, H. Bouchiat, and J. C. Cuevas. "Proximity DC SQUIDS in the long-junction limit." In: *Physical Review B* 77.16 (2008), p. 165408.
- [55] D. Hazra, L. M. A. Pascal, H. Courtois, and A. K. Gupta. "Hysteresis in superconducting short weak links and micro-SQUIDS." In: *Physical Review B* 82.18 (2010), p. 184530.
- [56] A. Kemppinen, A. J. Manninen, M. Möttönen, J. J. Vartiainen, J. T. Peltonen, and J. P. Pekola. "Suppression of the critical current of a balanced superconducting quantum interference device." In: *Applied Physics Letters* 92.5 (2008), p. 052110.
- [57] F. Giazotto, J. T. Peltonen, M. Meschke, and J. P. Pekola. "Superconducting Quantum Interference Proximity Transistor." In: *Nature Physics* 6.4 (2010), pp. 254–259.
- [58] F. Giazotto and F. Taddei. "Hybrid superconducting quantum magnetometer." In: *Physical Review B* 84.21 (2011), p. 214502.
- [59] M. Meschke, J. T. Peltonen, J. P. Pekola, and F. Giazotto. "Tunnel spectroscopy of a proximity Josephson junction." In: *Physical Review B* 84.21 (2011), p. 214514.
- [60] R. N. Jabdaraghi, M. Meschke, and J. P. Pekola. "Non-hysteretic superconducting quantum interference proximity transistor with enhanced responsivity." In: *Applied Physics Letters* 104.8 (2014), p. 082601.
- [61] H. Le Sueur, P. Joyez, H. Pothier, C. Urbina, and D. Esteve. "Phase controlled superconducting proximity effect probed by tunneling spectroscopy." In: *Physical Review Letters* 100.19 (2008), p. 197002.

- [62] H. Q. Nguyen, T. Aref, V. J. Kauppila, M. Meschke, C. B. Winkelmann, H. Courtois, and J. P. Pekola. "Trapping hot quasi-particles in a high-power superconducting electronic cooler." In: *New Journal of Physics* 15.8 (2013), p. 085013.
- [63] R. N. Jabdaraghi, J. T. Peltonen, O-P. Saira, and J. P. Pekola. "Low-temperature characterization of Nb-Cu-Nb weak links with Ar ion-cleaned interfaces." In: *Applied Physics Letters* 108.4 (2016), p. 042604.
- [64] R. N. Jabdaraghi, J. T. Peltonen, D. S. Golubev, and J. P. Pekola. "Magnetometry with Low-Resistance Proximity Josephson Junction." In: *Journal of Low Temperature Physics* 191.5-6 (2018), pp. 344-353.
- [65] O.-P. Saira, M. Zgirski, K. L. Viisanen, D. S. Golubev, and J. P. Pekola. "Dispersive Thermometry with a Josephson Junction Coupled to a Resonator." In: *Physical Review Applied* 6 (2 2016), p. 024005.
- [66] R. N. Jabdaraghi, D. S. Golubev, J. P. Pekola, and J. T. Peltonen. "Noise of a superconducting magnetic flux sensor based on a proximity Josephson junction." In: *Scientific Reports* 7.1 (2017), p. 8011.